UNIVERSITA' DEGLI STUDI DI TRIESTE

XXV CICLO DEL DOTTORATO DI RICERCA IN NANOTECNOLOGIE

DESIGN, FABRICATION AND CHARACTERIZATION OF METAMATERIAL INSPIRED STRUCTURES FOR SENSING APPLICATIONS

Settore scientifico-disciplinare FIS/03

DOTTORANDA
VALENTINA GIORGIS

COORDINATORE
PROF. MAURIZIO FERMEGLIA

SUPERVISORE DI TESI
PROF. FILIPPO ROMANATO

ANNO ACCADEMICO 2011 / 2012

Abstract

In the last few years the interest in nanostructures for sensing application has grown increasingly [1], [2], [3], [4] leading to the development of new designs based on the surface plasmon resonance of metallic structures.

By carefully tuning the geometry of the nanostructures, it is possible to adjust the resonance frequencies, resulting in amplification and confinement of the electromagnetic field around specific areas of the structure. The oscillating plasmonic field obtained may be exploited for bio-chemical detection.

In this work we present the design, the fabrication and the characterization of gold nano split ring resonators on transparent substrate, combining finite element simulation, lithographic techniques and transmittance ellipsometry. Bearing in mind the importance of the control of the geometric parameters, we approach the structure fabrication using top-down lithographic techniques. We explore and develop, in particular, an X-ray Lithography based process for producing high volumes of tall, nanometric split ring resonators. The choice of X-ray Lithography as the main technique is justified by the possibility to obtain higher aspect ratio and to achieve large areas array of split ring resonators in a single, fast exposure, compared to other techniques, such as nanoimprinting or Electron Beam Lithography[5].

The structure we focused our research on is the split ring resonator, one of the most popular and studied geometries for metamaterials. As metamaterial building block, the split ring resonator exhibits characteristic plasmonic resonances and a tunable frequency magnetic resonance [6]. Besides, the split ring resonator shows a strong polarization dependance and a strong mechanical stability.

In this thesis we will analyze the optical properties of the split ring nanostructure when illuminated in normal incidence. The analysis of the response in transmission at two polarization is presented. The preliminary detection test performed using a monolayer of dodecanthiol evidence the detection potential of this geometry.

Sommario

L'utilizzo di nanostrutture nell'ambito della sensoristica ha conosciuto, negli ultimi anni, una crescente espansione [1], [2], [3], [4], che ha portato allo sviluppo di nuove geometrie, progettate in modo da sfruttare le risonanze plasmoniche delle strutture metalliche.

La geometria delle strutture in questione può essere attentamente calibrata in modo da ottenere, in specifiche aree della struttura stessa, amplificazione e confinamento del campo elettromagnetico. Questa caratteristica può quindi essere utilizzata per il rilevamento di sostanze bio-chimiche.

Nel corso di questa tesi verranno presentate la progettazione, la fabbricazione e la caratterizzazione di *split ring resonator* in oro su substrato trasparente. A questo scopo abbiamo utilizzato una combinazione di svariate tecniche: la simulazione a elementi finiti, tecniche litografiche *top-down* e misure ellissometriche. La scelta di tecniche litografiche *top-down* è dovuta all'importanza fondamentale rivestita dal controllo sui parametri geometrici delle strutture da realizzare. In particolare abbiamo basato l'impianto fabbricativo sulla tecnica della litografia a raggi X, allo scopo di ottenere *split ring resonator* alti su vaste aree. Infatti, i vantaggi della litografia a raggi X, rispetto ad altre tecniche quali il *nanoimprinting* o la litografia elettronica[5], sono la possibilità di ottenere strutture con alto *aspect ratio* su grandi aree per mezzo di una singola, rapida esposizione.

La nostra ricerca si è concentrata su una struttura, lo *split ring resonator*, che è stata una delle prime geometrie ad essere sviluppata e analizzata nell'ambito dei metamateriali. La particolarità dello *split ring resonator* sta nelle caratteristiche risonanze plasmoniche e una risonanza magnetica [6] che può essere regolata con la calibrazione della geometria della struttura. Lo *split ring resonator*, inoltre, presenta una grande stabilità strutturale e la sua risposta ottica dipende fortemente dalla polarizzazione dell'onda con cui lo si illumina.

In questo lavoro analizzeremo le proprietà ottiche della struttura *split ring resonator* in illuminazione normale e la risposta in trasmissione in rapporto alla polarizzazione della radiazione incidente. Un esperimento preliminare

sulla capacità della struttura di rivelare uno monostrato di tioli autoassemblati ha messo in luce le sue potenzialità di sensore.

Contents

List of Figures

Preface

Motivations

The development of novel, fast and efficient sensors has become increasingly important in a great number of science and technology fields, due to their countless applications in everyday life.

In this thesis we focus our attention of optical sensing and, in particular, surface plasmon resonance sensors. The main advantage of optical sensing is the possibility to accurately recognize substances by label-free and non-invasive detection methods, by converting the quantity to be measured (measurand) to another quantity encoded in one of the characteristic of the light wave. Surface plasmon resonance sensors rely on the collective electron oscillation at metal-dielectric interface, generated by the coupling of the incident electromagnetic field to the oscillations of the metal electron plasma. When a change occurs in the refractive index of the dielectric, it results in a change in the propagation constant of the surface plasmon [17].

When we consider metal nanostructures, the surface plasmon phenomenon affects the interaction of the structure with light [18]. The resulting resonant oscillations leads to amplification and confinement of the local electromagnetic field around particular areas of the geometry. New fabrication capabilities, development in nanoengineering methods, improvements in the computational power of electromagnetic simulation are driving to new designs of the nanostructures, offering the possibility to go beyond the standard sensing geometries, such as grating and shallow metal nanoparticles.

The control on the geometric parameters of the nanostructure allows to localize the plasmonic modes and to tune the resonance frequencies: only a top-down lithographic fabrication process offers possibility to obtain well ordered and regular complex nanostructure geometries.

We focus our research on the split ring resonator geometry, usually employed as metamaterial's building block [19] [20] [21]. This structure was originally designed in order to obtain a negative effective magnetic permeability above a certain value of frequency of the incident light. Moreover, due to

its morphology, the split ring resonator is able, even below this frequency, to confine and enhance the electromagnetic field into the gap area, when the electric field of the incident radiation is polarized along the gap itself. Even if the metamaterial behavior is not exploited in our research, since we limit our analysis in a range of wavelength comparable to the structure's period (the visible - near-infrared range), the split ring resonator geometry proves promising detection properties [22] [23] [2] [24].

In the last years a few groups [3] [25] [26] has analyzed the split ring resonator geometry for sensing application. Our innovative approach is the development of a X-ray Lithography based process [27], in order to obtain large arrays of tall split ring resonators on a transparent substrate, and to organize the arrays in a multiple chip sample to perform, eventually, microfluidic analysis [28]. This choice allows us to produce tall nano split ring resonator on a larger area compared to other fabrication techniques, such as Electron Beam Lithography [3]. Moreover, the development of the fabrication process permits to produce structures below the micrometric range [29] [30] [26], which consequently allows the analysis in the visible and near-infrared region. The transparent substrate consents transmission analysis in normal incidence.

The development of the X-Ray Lithography based process is the core of this thesis work.

Outline of the thesis

We are now giving a brief overview of the thesis chapters:

Capitolo 1- Introduction and theory: in this chapter we introduce the theory of the interaction of light with metal, presenting the electromagnetic theory of surface plasmon resonances. The sensitivity of the surface plasmon polaritons to the variation of the refractive index at the surface of the metal film supporting those electromagnetic surface waves may be exploited for bio-chemical sensing. By patterning the metal film in nanostructures, the plasmonic modes and the resonance frequencies may be localized and tuned. The split ring resonator, one of the first geometry proposed for metamaterials, is proposed as plasmonic nanostructure due to the strong polarization dependance and high mechanical stability.

Capitolo 2 - Structure simulation: the simulated optical response of the SRR to visible and near-infrared light illumination is presented in this

chapter. The structure has been modelled by the finite element analysis software COMSOL Multiphysics. We analyzed the case of normally impinging plane wave with electric field polarized parallel and perpendicular to the gap, focusing our attention on the peak in transmittance, in the $400 - 1100nm$ range of wavelength. Near field analysis of the distribution of the electric and magnetic field enhancement corresponding to transmittance peak has been used in order to understand the origin of the resonances.

Capitolo 3 - Methods: in this chapter we are presenting the fabrication and characterization techniques exploited in the SRR samples production. The main fabrication technique we used is X-Ray lithography. X-Ray lithography itself and sample fabrication request the use of many other techniques: UV Lithography, wet and dry etching, Electron Beam Lithography and electrochemical growth among the others. Scanning Electron Microscopy and Ellipsometry have been employed in this thesis for the samples characterization.

Capitolo 4 - Nanofabrication: this is the central chapter of the thesis, where the fabrication process development is described. The principal exploited technique is X-ray lithography, performed LILIT beamline at Elettra Synchrotron in Trieste. Membrane design, mask fabrication, X-ray lithography, sample preparation and metal deposition are some of the steps composing the fabrication process we have optimized.

Capitolo 5 - Characterization: the results of the characterization of the fabricated SRR samples and a preliminary test of the detection of a functionalization thiol monolayer are shown. Transmission spectra of the fabricated samples have been acquired by ellipsometry in the range $400 - 1100nm$, at normal incidence. The measurement have been performed for two polarization: electric field parallel and electric field perpendicular to the gap of the split ring resonator.

Capitolo 6 - Future work and conclusions: in this chapter we summarize the result obtained in the thesis work, from the design and simulation of the structure, to the fabrication and the optimization of the process, to the characterization of the fabricated samples by ellipsometric measurement.

Chapter 1

Introduction and theory

In this chapter we introduce the theory of the interaction of light with metal, presenting the electromagnetic theory of surface plasmon resonances [8] [31] [32]. The sensitivity of the surface plasmon polaritons to the variation of the refractive index at the surface of the metal film supporting those electromagnetic surface waves may be exploited for bio-chemical sensing.
Plasmonic bio-chemical sensors belong to the field of optical sensing, which is particularly advantageous due to the label-free and non-invasive detection methods suitable for accurate substance recognition [33] [17] [34]. By careful patterning the metal film in nanostructures, it is possible to localize the plasmonic modes and tune the resonance frequency.
The split ring resonator, one of the first geometry proposed for metamaterials, is introduced. The strong polarization dependance and high mechanical stability makes this nanostructure a promising candidate for plasmonic sensing applications [25] [35] [36].

1.1   SPPs basis: Maxwell equation

Surface Plasmon Polaritons (SPPs) are electromagnetic excitations propagating at the interface between a dielectric and a conductor. They are generated by the coupling of the incident electromagnetic fields to the oscillations of the conductor's electron plasma, which produces electromagnetic surface waves evanescently confined in the perpendicular direction.
A change in the refractive index of the dielectric produces a change in the propagation of the SPPs. In nanostructures, the SPPs generated by the interaction of the structures itself with light may lead to amplification and

confinement of the local electromagnetic field around particular facets of
the structure geometry. The confinement and the sensitivity of the SPP to
changes of the refractive index of the dielectric medium may be exploited to
create sensing devices.
Surface Plasmon Polaritons physical properties can be investigated consid-
ering the wavelike solution of Maxwell's equations at the interface between
two semi-infinite media.
We take as a starting point Maxwell's equations, in the absence of free charges
and currents:

$$\nabla \cdot \mathbf{D} \;=\; 0 \tag{1.1}$$

$$\nabla \times \mathbf{E} \;=\; -\frac{\partial \mathbf{B}}{\partial t} \tag{1.2}$$

$$\nabla \cdot \mathbf{B} \;=\; 0 \tag{1.3}$$

$$\nabla \times \mathbf{H} \;=\; \frac{\partial \mathbf{D}}{\partial t} \tag{1.4}$$

We can define the constitutive relations, limiting ourselves to linear, isotropic
and nonmagnetic media:

$$\mathbf{D} \;=\; \epsilon_0 \epsilon_r \mathbf{E} = \epsilon \mathbf{E} \tag{1.5}$$

$$\mathbf{B} \;=\; \mu_0 \mu_r \mathbf{H} = \mu \mathbf{H} \tag{1.6}$$

where ϵ_r and μ_r are respectively the relative dielectric permittivity and the
relative dielectric permeability of the medium, ϵ_0 and μ_0, are their values in
vacuum. Considering a set of time-varying harmonic plane waves as solution
of Maxwell's equations in the high frequency regime, we can write the fields
in the following form:

$$\mathbf{E}(x,y,z,t) \;=\; \mathbf{E}(x,y,z,t)e^{i\omega t}$$
$$\mathbf{H}(x,y,z,t) \;=\; \mathbf{H}(x,y,z,t)e^{i\omega t} \tag{1.7}$$

Substituting (1.7) in (1.2) and (1.4), and using the constitutive relations, we
can derive a unique formulation for the magnetic field:

$$\nabla \times (\epsilon_r^{-1} \nabla \times \mathbf{H}) - k_0^2 \mathbf{H} = 0 \tag{1.8}$$

where $k_0 = \omega/c$ is the wave vector of the propagating wave in vacuum. As
we considered only non magnetic materials, $\mu_r = 1$.
Typically equation (1.8) is solved separately in regions of constant ϵ_r and
the obtained solutions have to be matched using the appropriate boundary
conditions. Using vector identities[1] and (1.4), this equation simplifies in

$$\nabla^2 \mathbf{H} + k_0^2 \epsilon_r \mathbf{H} = 0 \tag{1.9}$$

---

[1]$\nabla \times \nabla \times \mathbf{H} \equiv \nabla(\nabla \cdot \mathbf{H}) - \nabla^2 \mathbf{H}$
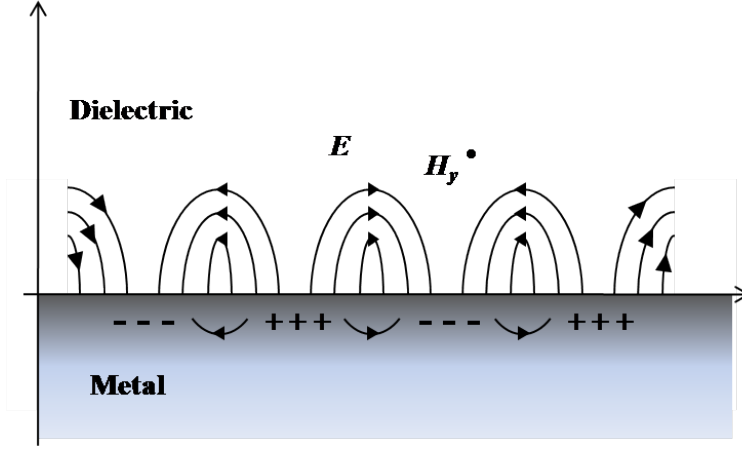
Figure 1.1: This figure shows the coupling between the electromagnetic wave and the surface charges, resulting in excited SPPs at the interface between metal and dielectric. [7]

known as *Helmholtz equation*. It is possible to obtain the wave equation for **H** necessary for the general analysis of guided electromagnetic modes considering the geometry showed in Figure 1.1, where the interface sustaining the propagating wave coincides with $z = 0$, and the particular case the wave propagates alog x-direction. Due to the continuous translational symmetry along the y-direction, the field of the propagating wave is invariant along this direction and it is possible to write it as

$$\mathbf{H}(x, y, z) = \mathbf{H}(z)e^{ik_x x} \tag{1.10}$$

where k_x, called *propagation constant*, is the component of the wave vector along the direction of propagation. Inserting (1.10) in Helmholtz equation (1.9), we obtain

$$\frac{\partial^2 \mathbf{H}(z)}{\partial z^2} + (k_0^2 \epsilon_r - k_x^2)\mathbf{H}(z) = 0 \tag{1.11}$$

This equation, and the analogous one for the electric field **E**, is the starting point to study of guided electromagnetic modes in waveguides and to analyze the SPP dispersion relation.

1.2 SPPs at a single interface - dispersion relation

It is possible to examine the properties of SPPs by analyzing their dispersion relation, which can be derived studying the most simple geometry
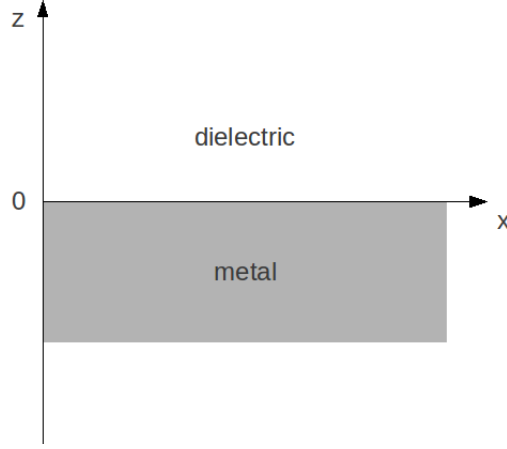
Figure 1.2: Geometry for SPP propagation at a single interface between a metal and a dielectric.

sustaining SPPs: the single, flat interface between a dielectric space and a conductive one. Let us consider the ideal system shown in Figure 1.2: it consists of a dielectric material, in the half space $z > 0$, characterized by an isotropic complex relative dielectric constant $\epsilon_2 = \epsilon_2' + \epsilon_2''$, and a metal, in $z < 0$, described by an isotropic, frequency-dependent, complex dielectric function $\epsilon_1(\omega) = \epsilon_1' + i\epsilon_1''$. Since medium 1 is a metal, it is required that $Re[\epsilon_1] < 0$, i.e. $\epsilon_1' < 0$. For metals, this condition is fulfilled at frequencies below the bulk plasmon frequency ω_p [2].

As a consequence of Maxwell's equations, fields have to obey to the following boundary conditions at the interface:

$$
\begin{aligned}
\mathbf{n} \cdot (\mathbf{D}_1 - \mathbf{D}_2) &= 0 \\
\mathbf{n} \times (\mathbf{E}_1 - \mathbf{E}_2) &= 0 \\
\mathbf{n} \cdot (\mathbf{B}_1 - \mathbf{B}_2) &= 0 \\
\mathbf{n} \times (\mathbf{H}_1 - \mathbf{H}_2) &= 0
\end{aligned}
\tag{1.12}
$$

where $\mathbf{n}$ is the versor normal to the surface. Since the normal displacement vector component $\mathbf{D}_\perp$ must be continuous, the electric field tangential component $\mathbf{E}_\parallel$ is continuous, while the normal one is not.

---

[2] $\omega_p^2 = \frac{ne^2}{\epsilon_0 m}$

Thus we have:

$$
\begin{aligned}
\mathbf{E}_{1,\parallel} &= \mathbf{E}_{2,\parallel} \\
\epsilon_1 \mathbf{E}_{1,\perp} &= \epsilon_2 \mathbf{E}_{2,\perp} \\
\mathbf{H}_{1,\parallel} &= \mathbf{H}_{2,\parallel} \\
\mu_1 \mathbf{H}_{1,\perp} &= \mu_2 \mathbf{H}_{2,\perp}
\end{aligned}
\tag{1.13}
$$

Our aim is to look for propagating wave solutions confined to the interface, i.e. with evanescent decay in the perpendicular direction, z.
We first look at TM solutions: the guess magnetic field is in the form

$$
\mathbf{H}_2 = (0, H_{2,y}, 0)e^{i(k_{2,x}x - \omega t) - k_{2,z}z}
\tag{1.14}
$$

for $z > 0$ (medium 2: dielectric), and

$$
\mathbf{H}_1 = (0, H_{1,y}, 0)e^{i(k_{1,x}x - \omega t) + k_{1,z}z}
\tag{1.15}
$$

for $z < 0$ (medium 1: metal).
$k_{1,z}$ and $k_{2,z}$ must be positive in order to describe an electromagnetic wave localized at the dielectric-metal interface at $z = 0$. If we apply the boundary conditions (1.13), then

$$
k_{1,x} = k_{2,x} \equiv k_x
\tag{1.16}
$$

Using (1.4) we find the following expression for the x and z components of the electric field:

$$
E_{2,x} = i\frac{k_{2,z}}{\omega\epsilon_2}H_{2,y}e^{i(k_x x - \omega t) - k_{2,z}z}
\tag{1.17}
$$

$$
E_{2,z} = -\frac{k_x}{\omega\epsilon_2}H_{2,y}e^{i(k_x x - \omega t) - k_{2,z}z}
\tag{1.18}
$$

for $z > 0$, and

$$
E_{1,x} = -i\frac{k_{1,z}}{\omega\epsilon_1}H_{1,y}e^{i(k_x x - \omega t) - k_{1,z}z}
\tag{1.19}
$$

$$
E_{1,z} = -\frac{k_x}{\omega\epsilon_1}H_{1,y}e^{i(k_x x - \omega t) - k_{1,z}z}
\tag{1.20}
$$

for $z < 0$. Applying the boundary conditions (1.13), we now obtain:

$$
\begin{cases}
\frac{k_{1,z}}{\epsilon_1}H_{1,y} + \frac{k_{2,z}}{\epsilon_2}H_{2,y} = 0 \\
H_{1,y} = H_{2,y}
\end{cases}
\tag{1.21}
$$

which admits solution only if the determinant vanishes:

$$
\frac{k_{1,z}}{\epsilon_1} + \frac{k_{2,z}}{\epsilon_2} = 0
\tag{1.22}
$$
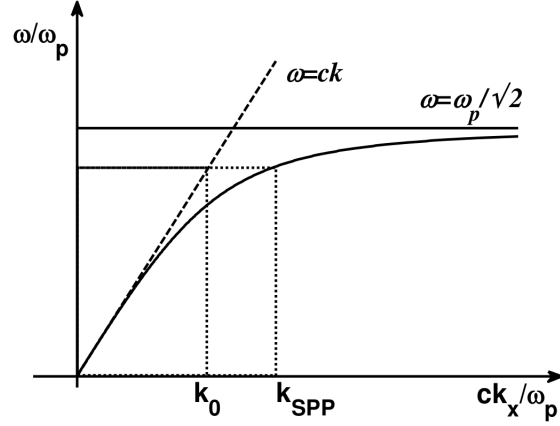
Figure 1.3: SPP dispersion curve. This figure shows the momentum mismatch that must be overcome in order to couple light and excite SPP modes. [7]

When we apply Helmholtz equation to (1.14) and (1.15) we have:

$$k_{j,z}^2 + k_x^2 = \epsilon_j \left(\frac{\omega}{c} \right)^2 \tag{1.23}$$

Combining (1.22) and (1.23) we obtain the central result of this section, the dispersion relation of SPPs propagating at the interface between the two half spaces:

$$k_x = \frac{\omega}{c} \sqrt{\frac{\epsilon_1 \epsilon_2}{\epsilon_1 + \epsilon_2}} \tag{1.24}$$

The dielectric function of an undamped free electron plasma for $\omega < \omega_p$ is:

$$\epsilon(\omega) = 1 - \frac{\omega_p^2}{\omega^2} \tag{1.25}$$

Substituting (1.25) in (1.24), and considering vacuum as dielectric interface (i.e. $\epsilon_2 = 1$) with a Drude metal, we obtain the curve plotted in Figure 1.24.

The dispersion curve of a SPP, due to its bound nature, lies on the right side of the dispersion relation of light in vacuum. This implies SPPs are non radiative waves that can not be excited directly by incident light, but an additional momentum must be provided. Considering small wave vectors, corresponding to low (below mid-infrared) frequencies, we can see the SSP propagation constant is close to k_0 at the light line. In this regime the waves extend over many wavelengths into dielectric space, therefore the SSPs acquire the nature of grazing-incidence light field and are also known as *Sommerfeld-Zenneck waves*.

In the opposite regime of large k_x, the group velocity goes to zero since the

derivative of the dispersion relation tends to zero. Phase velocity goes to zero as well. In this limit the SPP resembles a localized fluctuation of the electron plasma. The frequency of the SPPs approaches the characteristic *surface plasmon frequency*

$$\omega_{sp} = \frac{\omega_p}{\sqrt{1 + \epsilon_2}} \tag{1.26}$$

Let us briefly analyze the possibility of TE surface modes. We will see there are no modes supported at the metal-dielectric interface. We are considering a TE mode as guess solution for the electric field:

$$\mathbf{E}_2 = (0, E_{2,y}, 0)e^{i(k_{2,x}x - \omega t) - k_{2,z}z} \tag{1.27}$$

for $z > 0$, dielectric, and

$$\mathbf{E}_1 = (0, E_{1,y}, 0)e^{i(k_{1,x}x - \omega t) + k_{1,z}z} \tag{1.28}$$

for $z < 0$, metal. Using (1.2) it is possible to calculate the x and z components of the magnetic field:

$$H_{2,x} = -i\frac{k_{2,z}}{\omega}E_{2,y}e^{i(k_x x - \omega t) - k_{2,z}z} \tag{1.29}$$

$$E_{2,z} = \frac{k_x}{\omega}E_{2,y}e^{i(k_x x - \omega t) - k_{2,z}z} \tag{1.30}$$

for $z > 0$, and

$$H_{1,x} = i\frac{k_{1,z}}{\omega}E_{1,y}e^{i(k_x x - \omega t) - k_{1,z}z} \tag{1.31}$$

$$H_{1,z} = \frac{k_x}{\omega}E_{1,y}e^{i(k_x x - \omega t) - k_{1,z}z} \tag{1.32}$$

for $z < 0$. Continuity of E_y and H_x at the interface leads to the condition

$$(k_{1,z} + k_{2,z})E_{1,y} = 0 \tag{1.33}$$

However, since the real parts of $k_{1,z}$ and $k_{2,z}$ must be positive in order to have a localized wave, this condition is fulfilled only if $E_{1,y} = 0$. Since $E_{1,y} = E_{2,y}$, no surface mode exist.

An *s*-polarized surface plasmon polariton can not propagate along the planar dielectric-metal interface and no surface modes exist for TE polarization: surface plasmon polaritons only exist for TM polarization.

1.3 Spatial extention and propagation length of SPPs

As previously said, surface plasmon polaritons are surface waves localized at the interface between dielectric and metal. The field amplitude decreases exponentially in both media along the z-direction, normally to the surface as $\exp(-|k_{j,z}z|)$, since $k_{j,z}$ is purely imaginary.
The values of skin depths at which the fiel falls to $1/e$ are:

$$d_{j,z} = \frac{1}{|k_{j,z}|} \tag{1.34}$$

We can calculate them combining (1.23) and (1.24), assuming $\epsilon'' = 0$

$$d_{1,z} = \frac{\lambda}{2\pi}\sqrt{-\frac{\epsilon'_1 + \epsilon_2}{\epsilon'^2_1}}$$

$$d_{2,z} = \frac{\lambda}{2\pi}\sqrt{-\frac{\epsilon'_1 + \epsilon_2}{\epsilon'^2_2}} \tag{1.35}$$

We report in the following table the field penetration depths for SPP excited at different metal/dielectric interfaces: noble metals, such as gold and silver, and air and water as dielectris.

Metal/Dielectric field depths (nm) @ $\lambda = 633$nm	air $\epsilon_{air} = 1$	water $\epsilon_{water} = 1.78$
$\epsilon_{Au} = -12.1 + 1.3i$	$d_{Au,z} = 28$	$d_{Au,z} = 27$
	$d_{air,z} = 336$	$d_{water,z} = 181$
$\epsilon_{Ag} = -17 + 0.7i$	$d_{Ag,z} = 24$	$d_{Ag,z} = 23$
	$d_{air,z} = 403$	$d_{water,z} = 221$

In the dielectric medium above the metal the decay length of the field is of the order of half the wavelength of the light involved, whereas the decay length into the metal is one order smaller.
From dispersion relation (1.24) we notice that the wave vector k_x on the surface wave is complex when the dielectric function of the metal is complex. In the approximation $|Re[\epsilon_{dielectric}]| \gg Im[\epsilon_{dielectric}]$ the x-component of the plasmonic wave vector is a complex number:

$$k_x = \frac{\omega}{c}\sqrt{\frac{\epsilon'_1\epsilon_2}{\epsilon'_1 + \epsilon_2}} + i\frac{\omega}{c}\left(\frac{\epsilon'_1\epsilon_2}{\epsilon'_1 + \epsilon_2}\right)^{\frac{3}{2}}\frac{\epsilon''_1}{2\epsilon'^2_1} \tag{1.36}$$

Figure 1.4: SPP field components decreasing exponentially. This evanescent field is related to the non-radiative nature of SPPs: power can not propagates away from the surface. [7]

The intensity of a SPP along the direction of propagation decreases as $exp(-2xIm[k_x])$ and the *propagation length* of the SPPs can be defined as:

$$L = \frac{1}{2k_x''} \tag{1.37}$$

In the following table propagation lengths for various interfaces are shown.

Metal/Dielectric propagation length (μm) @ $\lambda = 633$nm	air $\epsilon_{air} = 1$	water $\epsilon_{water} = 1.78$
$\epsilon_{Au} = -12.1 + 1.3i$	10	4
$\epsilon_{Ag} = -17 + 0.7i$	38	15

Again, we are considering the SPP propagating at the interface between air or water and silver or gold, for TM wave at $\lambda = 633nm$.
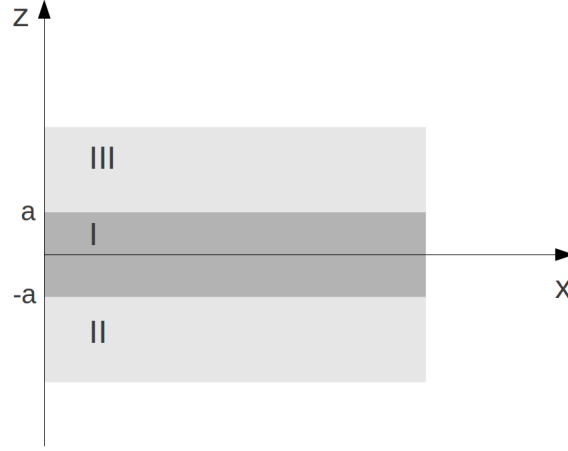
Figure 1.5: Geometry of a three-layer system, consisting of a thin layer I sandwiched between two infinite half spaces II and III

1.4   Multilayer Systems

Let us consider a system consisting of an alternating conducting and dielectric thin films. In a multilayer system, each single interface can sustain bound SPPs. When the separation between adjacent interfaces is comparable to or smaller than the decay length d of the interface mode, interactions between SPPs give rise to coupled modes.

We will focus on two specific three-layer systems (Figure 1.5) in order to elucidate the general properties of coupled SPPs: an insulator/metal/insulator (IMI) heterostructure, a thin metallic layer (I) sandwiched between two infinitely thick dielectric claddings (II, III), and a metal/insulator/metal (MIM) heterostructure, a thin dielectric core layer (I) sandwiched between two metallic claddings (II, III).

Let us consider non-oscillatory in the z-direction TM modes. For $z > a$ the field components are:

$$H_{III,y} = H_{III}e^{i(k_x x - \omega t) - k_3 z} \tag{1.38}$$

$$E_{III,x} = i\frac{k_3}{\omega\epsilon_3}H_{III}e^{i(k_x x - \omega t) - k_3 z} \tag{1.39}$$

$$E_{III,z} = -\frac{k_x}{\omega\epsilon_3}H_{III}e^{i(k_x x - \omega t) - k_3 z} \tag{1.40}$$

while for $z < -a$ we have:

$$H_{II,y} = H_{II}e^{i(k_x x - \omega t) + k_2 z} \tag{1.41}$$

$$E_{II,x} = -i\frac{k_2}{\omega\epsilon_2}H_{II}e^{i(k_x x - \omega t) + k_2 z} \tag{1.42}$$

$$E_{II,z} = -\frac{k_x}{\omega\epsilon_2}H_{II}e^{i(k_x x - \omega t) + k_2 z} \tag{1.43}$$

In the core region $-a < z < a$, the modes localized at the bottom and top interface couple:

$$H_{I,y} = H_{I,1}e^{i(k_x x - \omega t) + k_1 z} + H_{I,2}e^{i(k_x x - \omega t) - k_1 z} \tag{1.44}$$

$$E_{I,x} = -i\frac{k_1}{\omega\epsilon_1}H_{I,1}e^{i(k_x x - \omega t) + k_1 z} + i\frac{k_1}{\omega\epsilon_1}H_{I,2}e^{i(k_x x - \omega t) - k_1 z} \tag{1.45}$$

$$E_{I,z} = \frac{k_x}{\omega\epsilon_1}H_{I,1}e^{i(k_x x - \omega t) + k_1 z} + \frac{k_x}{\omega\epsilon_1}H_{I,2}e^{i(k_x x - \omega t) - k_1 z} \tag{1.46}$$

Note that we denote the component of the wave vector normal to the surface as $k_i \equiv k_{i,z}$. Moreover, we denote $k_{1,x} = k_{2,x} = k_{3,x} \equiv k_x$, as implied by the boundary conditions (1.13).
The requirement of continuity of H_y and E_x leads to:

$$H_{III}e^{-k_3 a} = H_{I,1}e^{k_1 a} + H_{I,2}e^{-k_1 a} \tag{1.47}$$

$$\frac{H_{III}}{\epsilon_3}e^{-k_3 a} = -\frac{H_{I,1}}{\epsilon_1}k_1 e^{k_1 a} + \frac{H_{I,2}}{\epsilon_1}k_1 e^{-k_1 a} \tag{1.48}$$

at $z = a$ and

$$H_{II}e^{-k_2 a} = H_{I,1}e^{-k_1 a} + H_{I,2}e^{k_1 a} \tag{1.49}$$

$$\frac{H_{II}}{\epsilon_2}e^{-k_2 a} = -\frac{H_{I,1}}{\epsilon_1}k_1 e^{-k_1 a} + \frac{H_{I,2}}{\epsilon_1}k_1 e^{k_1 a} \tag{1.50}$$

at $z = -a$. Solving this system of linear equation we find an implicit expression for the dispersion relation:

$$e^{-4k_1 a} = \frac{k_1/\epsilon_1 + k_2/\epsilon_2}{k_1/\epsilon_1 - k_2/\epsilon_2}\frac{k_1/\epsilon_1 + k_3/\epsilon_3}{k_1/\epsilon_1 - k_3/\epsilon_3} \tag{1.51}$$

When we consider the particular case where the sub- and the superstrates II and III are equal in terms of their dielectric response, i.e. $\epsilon_2 = \epsilon_3$ and $k_2 = k_3$, the dispersion relation (1.51) can be split in:

$$\tanh k_1 a = -\frac{k_2\epsilon_1}{k_1\epsilon_2} \tag{1.52}$$

$$\tanh k_1 a = -\frac{k_1\epsilon_2}{k_2\epsilon_1} \tag{1.53}$$

It can be shown that the first equation describes modes of odd vector parity, while the second describes the mode of even vector parities. If we apply the dispersion relations (1.52) and (1.53) to IMI and MIM structures it is possible to investigate the properties of the coupled SPP modes.
Let us start with IMI geometry: a $2a$ thickness metal layer sandwiched between two insulating layers. The dielectric function of the metal is $\epsilon_1 = \epsilon_1(\omega)$, and ϵ_2 is the positive and real dielectric constant of the insulating strates. The odd modes have frequencies ω_+ higher than the respective frequencies for a single interface SPP, and the even modes lower frequencies ω_-.

$$\omega_+ = \frac{\omega_p}{\sqrt{1 + \epsilon_2}}\sqrt{1 + \frac{2\epsilon_2 e^{-2k_x a}}{1 + \epsilon_2}} \qquad (1.54)$$

$$\omega_- = \frac{\omega_p}{\sqrt{1 + \epsilon_2}}\sqrt{1 - \frac{2\epsilon_2 e^{-2k_x a}}{1 + \epsilon_2}} \qquad (1.55)$$

Both modes have interesting, though opposite, behavior. Odd modes evolve into a plane wave supported by the homogeneous dielectric environment when the metal film thickness decreases and the confinement of the coupled SPP to the metal film decreases as well, producing, in real metals described by complex $\epsilon(\omega)$, an increase of the propagation length, resulting in *long-ranging* SPP. On the other hand, the confinement of the even modes increases with decreasing metal film thickness, resulting in a reduction in propagation length. Moving on to MIM geometries, $\epsilon_2 = \epsilon_2(\omega)$ is the dielectric function of the metal and ϵ_1 is the dielectric constant of the insulating core. Considering the fundamental odd mode of the system we note that it does not exhibit a cutoff for vanishing core layer thickness. In Figure 1.6 the dispersion relation curve of the odd mode for a silver/air/silver multilayer is shown. The propagation constant k_x does not go to infinity as the surface plasmon frequency is approached, but folds back and eventually crosses the light line. In the case the width of the dielectric core is suffcently small, a large propagation constant can be achieved even for excitation below ω_{sp}.

1.5   Excitation of SPP

In a former paragraph, we point out that SPP dispersion curve (see Figure 1.3) lies to the right of the light line of the dielectric and excitations by three-dimensional light beam is not possible: at a given frequency, the wave vector has to be increased by a Δk_x value in order to couple with surface polaritons. In order to promote this coupling, special techniques for phase-matching are
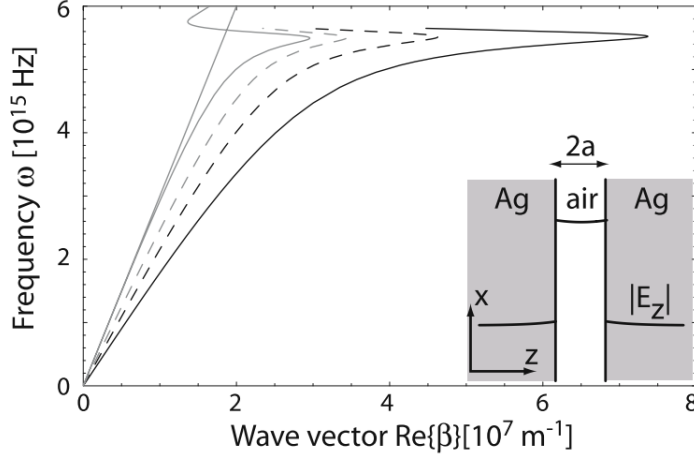
Figure 1.6: Dispersion relation of the fundamental coupled SPP modes of a silver-air-silver heterostructure. Air core size: 100nm (broken gray curve), 50nm (broken black curve), 25nm (continuous black curve). Dispersion of a SPP at single interface (gray curve) and air light line (gray line) are shown. [8]

required. Two of the most common phase matching techniques are prism coupling and grating coupling.

1.5.1 Prism coupling

The prism coupling technique, also known as Attenuated Total Refraction (ATR) method, consists in giving rise to surface polaritons at the metal-dielectric surface thanks to the passage of the exciting wave through a medium with a refractive index greater than the dielectric one. Let us consider a three-layer system consisting of a thin metal layer sandwiched between two insulators of different dielectric constant. When the light propagating in the higher dielectric constant insulator hit on the metal, part of the light is reflected back and part progresses in the metal as an inhomogeneous electromagnetic wave, which decays exponentially in the direction perpedicular to the interface between the first insulator and the metal. If the metal film is thin enough (less than $100nm$ for light in visible and infrared spectrum), the evanescent wave penetrates through the metal film and couples with a surface plasmon at the boundary between the metal and the lower dielectric constant insulator. SPP with propagating constant k between the light lines of air and the higher index dielectric can be excited (Figure 1.7).
The higher index dielectric is usually in form of a prism. Note that there is no phase matching at prism-metal interface.
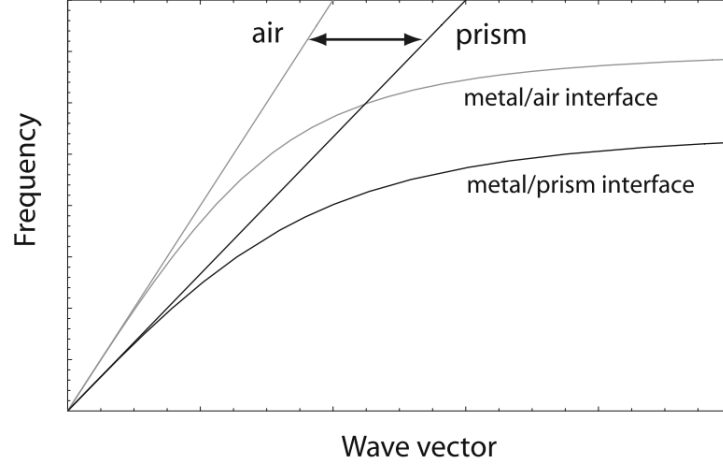
Figure 1.7: Prism coupling and SPP dispersion. Only propagating constants between light lines of air and prism are accessible. [8]

Two different geometries for prism coupling are possible: Kretschmann geometry and Otto geometry. In the Kretschmann method a thin film of metal is deposited on the top of a glass prism, while in the Otto configuration the prism is separated from the metal film by a thin air gap (see Figure 1.8). The prism coupling technique is also suitable for exciting coupled SPP modes in MIM and IMI three-layer systems.

1.5.2   Grating coupling

Another way to overcome the mismatch in wave vector is patterning the metal surface with a shallow grating of grooves or holes with lattice constant a. Diffracted light can couple to SPP if the momentum of diffracted light parallel to the surface is equal to the propagation constant of the plasmon:

$$k_{SPP} = \frac{2\pi}{\lambda} n_d \sin \theta_i + m \frac{2\pi}{a} \qquad (1.56)$$

where n_d is the refractive index of the dielectric medium in contact with the metal, λ is the incident wavelength and θ_i is the incident angle.
It is possible to analyze the effect of diffraction grating on the incident wave and plasmon polaritons coupling using Fraunhofer approximation. Let us consider one dimensional gratings (Figure 1.9). For an incident plane wave diffracted field distribution is proportional to the Fourier transform of the grating transmission function $\tau(x)$, which is the convolution of the grating
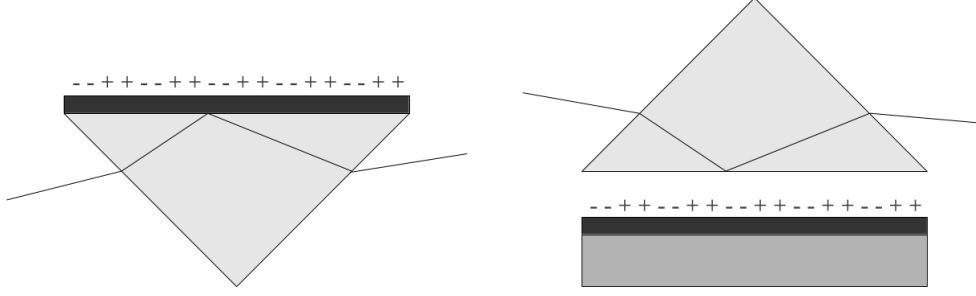
Figure 1.8: Prism coupling: Kretschmann (on the left) and Otto configuration (on the right)

structure function $s(x)$ and of the profile function $f(x)$ of the single element of the grating:

$$\tau(x) = s(x) * f(x) = \sum_{i=0}^{N} \delta(x - ia) * f(x) \qquad (1.57)$$

the sum over Dirac delta function describes the N-grating structure. The field distribution is given by

$$F(k_x) = \mathcal{F}[s * f](k_x - k_{0x}) = \mathcal{F}[s](k_x - k_{0x}) \cdot \mathcal{F}[f](k_x - k_{0x}) \qquad (1.58)$$

and diffracted intensity is proportional to che squared module of F:

$$I(k_x) \propto |\mathcal{F}[f](k_x - k_{0x})|^2 \cdot \left| \frac{\sin \frac{(k_x - k_{0x})aN}{2}}{\sin \frac{(k_x - k_{0x})a}{2}} \right|^2 \qquad (1.59)$$

The zeroes in the denominator of the structure factor give the intensity maxima

$$\frac{(k_x - k_{0x})a}{2} = n\pi \qquad (1.60)$$

from which it is possible to obtain the grating equation:

$$k_x = k_{0x} + n\frac{2\pi}{a} \qquad (1.61)$$

Maxima intensity is modulated by the form factor given by Fourier transform of the transmission function of the single element of the grating. Let us
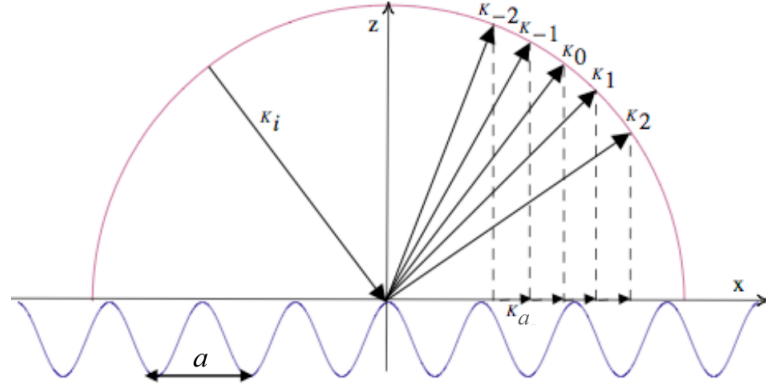
Figure 1.9: Grating coupling

assume that these waves carry away the whole incident energy: the diffracted field can be described as the superimposition of plane waves:

$$E(x, z) = \sum_{n=-\infty}^{+\infty} E_n e^{i(k_{nx}x + k_{nz}z)} \tag{1.62}$$

where $k_{nx} = k_{0x} + nk_a$, $k_{nz} = \sqrt{k_i^2 - k_{nx}^2}$ and k_i is the wave vector of the incident radiation, E_n gives the weight of the nth diffracted order. If n is large enough, k_{nz} becomes purely imaginary and the corresponding component represents an evanescent wave propagating along the x-axis and damped along the z-axis: the light couples with the grating. If the x-component wave vector of an intensity maximum matches the SPP wave vector of that frequency, plasmons are excited along the metal-dielectric surface.

The reverse process can also take place: surface plasmon polaritons propagating along a grating modulated surface can couple to light and radiate. Propagating direction of SPPs can be influenced and SPPs focusing can be attained by properly designing grating structure.

1.6   Localized surface plasmon

Localized surface plasmons are *non-propagating* excitations of the conduction electrons of metallic nanostructures coupled to the electromagnetic field. Those plasmonic excitations, occurring in isolated nanoparticles, are simpler to induce compared to the bulk metal case.

The penetration depth of an electromagnetic field on a metal is of orders of tens of nanometers: this means only the electrons of the metal within this region can interact with the impinging electromagnetic wave. Let us consider
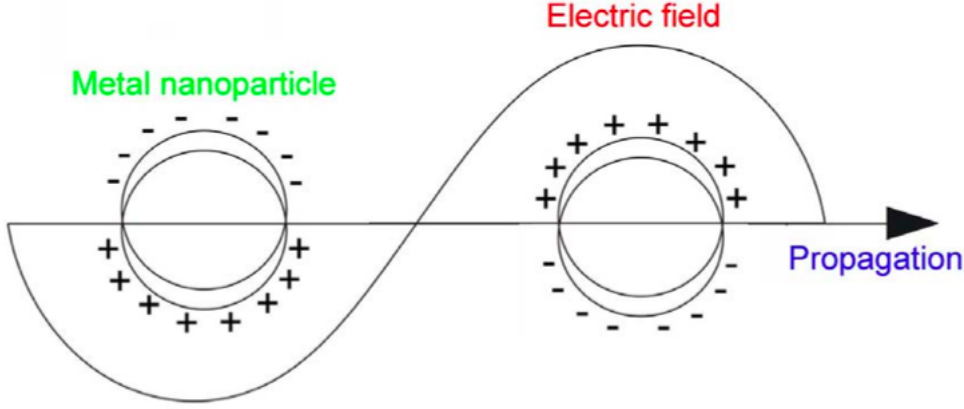
Figure 1.10: Electric dipole created in a nanosphere by the incident electromagnetic field. [9]

a metallic spheric nanoparticle whose size is smaller than the penetration depth. The particle is characterized by a natural oscillatory frequency given by the plasma frequency of the bulk metal and the shape of the particle itself.

An incident electromagnetic field, due to the size of the nanoparticle, interacts with all the nanoparticle's free electron, creating an electric dipole (Figure 1.10). The nanoparticle can be thus considered an electromagnetically driven oscillator. If the impinging electromagnetic wave matches the particle natural oscillatory frequency, a resonant enhancement of the surface plasmon takes place. The enhancement is confined to the nanoparticle, unable to travel like plasmons in bulk metal: this resonance is considered a localized surface plasmon resonance (LSP).

The localized surface plasmon resonance of a nanoparticle causes both scattering and absorption of the exciting electromagnetic field to take place. Scattering is a consequence of the particle's fluctuating charge distribution re-radiating the exciting wave, while absorption can be attributed to energy losses from within the LSP.

The frequency of LSP resonance is given by the extinction cross-section of the particle, σ_{ext}, a combination of absorption and scattering cross-section: $\sigma_{ext} = \sigma_{sca} + \sigma_{abs}$. For particles whose diameter is smaller than $30nm$ it is possible to describe extinction and scattering using Mie theory [37] [38], a solution of Maxwell's equations describing electromagnetic interaction with spherical particles:

$$\sigma_{ext} = 9\frac{\omega}{c}\epsilon_2^{3/2}V\frac{\epsilon_1''}{(\epsilon_1' + 2\epsilon_2)^2 + \epsilon_1''^2} \tag{1.63}$$

$$\sigma_{sca} = \frac{3}{2\pi} \left(\frac{\omega}{c} \right)^4 \epsilon_2^2 V^2 \frac{(\epsilon_1' - \epsilon_2)^2 + \epsilon_1''^2}{(\epsilon_1' + 2\epsilon_2)^2 + \epsilon_1''^2} \tag{1.64}$$

where ω is incident wave frequency, ϵ_2 the dielectric function of the surrounding medium, V is the nanoparticle volume, ϵ_1' the real part of dielectric metal function and ϵ_1'' the imaginary part. It is possible to determine the absorption cross-section by subtracting scattering cross-section from extinction one.

In the case the particles size is larger than $30nm$ it may support multiple resonances and require calculation via numerical simulation.

The plasmonic resonance of a single or an array of nanoparticles is highly dependent on the particle's size, geometry, local dielectric environment, metallic composition and interparticle spacing. By controlling these factors it is possible to tune the LSP resonance over a range of wavelengths.

1.7 Split Ring Resonators

Split Ring Resonators (SRR) are one of the first and most studied geometries for metamaterials [39] [40].

To start to understand what a "metamaterial" is, it is interesting to look at the term etymology: the word "metamaterial" is composed by the greek suffix "*meta*", which means "beyond" and the word "material". It describes a class of materials which displays non-natural properties. Nowadays metamaterials are engineered materials, structured in specific manners that, when illuminated by an electromagnetic radiation, can exhibit resonances unique to the structure at certain frequencies. The structure composing a metamaterial, also known as *meta*-atoms, are engineered such that at these frequencies, the wavelength of the electromagnetic radiation is much larger than the structural unit sizes, and thus can excite these resonances while still failing to resolve the details of the structure. By properly driving the resonances, one can cause the electric permittivity ϵ and the magnetic permeability μ to become negative in a frequency band slightly above the resonance frequency.

Metamaterials with negative permittivity and permeability are known as *negative refractive index medium* or *left-handed medium*. Viktor G. Veselago introduced the term *left-handed medium* in his work published in 1968 [41]. He was the first suggesting that in a medium for which ϵ and μ are simultaneously negative, the phase of the electromagnetic waves would propagate in a direction opposite to that of the electromagnetic energy flow. In this case, the vectors $\mathbf{k}$, $\mathbf{E}$ and $\mathbf{H}$ form a left-hand set.

Pendry [42] [43] showed, first theoretically in 1996 then experimentally in 1998, that composite medium of periodically placed thin metallic wires exhibits a negative effective permittivity, ϵ_{eff} below a particular frequency. In 1999 he showed [44] that microstructures built from nonmagnetic materials, such as cylinders, split ring resonators and spirals, exhibit an effective magnetic permeability, μ_{eff}. Smith [45] experimentally demonstrate, in 2000, a composite medium that exhibits a frequency region in the microwave regime with simultaneously negative values of effective permeability $\mu_{eff}(\omega)$ and effective permittivity $\epsilon_{eff}(\omega)$.

The medium fabricated by Smith and his collaborators was based on a periodic array of interspaced conducting nonmagnetic split ring resonators and continuous wires.

A SRR is, basically, a metallic cylinder with a gap (Figure 1.11), which can produce an effective magnetic permeability. Within selected frequency range, this effective permeability may be negative.

The metamaterial behavior of the SRR can be described in a simplified way considering an equivalent LC circuit [46]. When the magnetic field of the
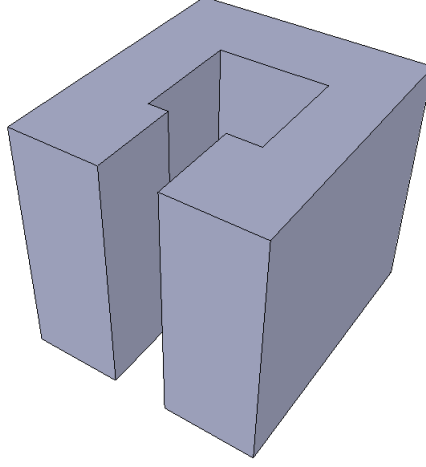
Figure 1.11: A single Split Ring Resonator

electromagnetic radiation is parallel to the cylinder vertical axis, it induces a circular current on the ring (inductive element). If the electric field is, at the same time, parallel to the ring gap, it produce a charge storing (capacitative element). A resonant LC circuit results.

Analyzing the SRR as a circuit, is possible to calculate the effective magnetic permeability:

$$\mu_{eff}(\omega) = 1 + \frac{f\omega^2}{\omega_0^2 - \omega^2 - i\Gamma\omega} \tag{1.65}$$

We have a resonant form of permeability with a resonant frequency of

$$\omega_0 = \frac{1}{\sqrt{LC}} = c\sqrt{\frac{d}{\epsilon_{gap}wl^2}} \tag{1.66}$$

where c is the speed of light in vacuum, l is the lateral dimension of the SRR (see Figure 1.12), d is the SRR gap size, w is the SRR width, a is the SRR array period, ϵ_{gap} is the electric permittivity of the dielectric in the gap, $f = l^2/a^2$ is the filling fraction of the material and Γ [3] is the dissipation parameter.

For frequencies larger than ω_0, the response is out of phase with the driving magnetic field and the μ_{eff} is negative up to the magnetic plasma frequency:

$$\omega_m = c\sqrt{\frac{d}{(1-f)\epsilon_{gap}l^2w}} \tag{1.67}$$

---

[3]$\Gamma = 2\rho/\mu_0 l\sqrt{2}$, where ρ is the resistivity of the SRR composing material and μ_0 is its permittivity
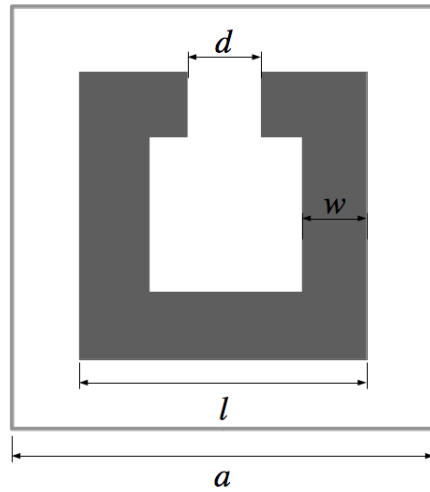
Figure 1.12: Scheme of a square SRR: l is lateral dimension, a is the period, w is the lateal width, d is gap size

Hence modifying SRR geometric parameter and the dielectric material into the gap, it is possible to tune the working frequency and, consequently, the effective permeability.

It has been demonstrated [47] that SRR has also a strong electric response in addition to the magnetic response, identical to that of cut wires. This electric cut-wire resonance has been described due to the oscillation of linear currents along the sides of the SRR which are parallel to the external electric field.

There are two methods for exciting a magnetic resonance: one is the magnetic coupling of the magnetic field perpendicular to the SRR vertical axes, perpendicular to the SRR plane, the other is the electric coupling of the electric field parallel to the SRR gap, as shown by Katsarakis et al. in 2004 [48]. The magnetic coupling requirement regarding the magnetic field oscillation implies the light to propagate parallel to the plane of the SRR (grazing illumination): such a configuration has not been accomplished in the optical domain, being challenging for nano-fabrication technology. Normal incidence illumination, however, probe the spectral position of the so called LC resonance via electric field coupling. A strong resonance at higher frequency is usually encountered, described at first as the plasmon excitation of the piece of wire opposed to the gap.

The other SRR response, the electric resonance, is excited coupling the electric field perpendicular to the SRR gap.

In 2006 Rockstuhl and Lederer [49] numerically studied the spectral response
of SRR, concluding that, at normal incidence, all resonances can be under-
stood as plasmonic resonance of increasing order of the entire structure. The
LC resonance can be treated as the fundamental mode of the SRR [50] and
the electric resonance the second mode. For the polarization of the electric
field parallel to the gap, the modes have an odd symmetry. For the polar-
ization of the electric field perpendicular to the gap, the modes have an even
symmetry. The analysis of the optical near field shows that the far field
spectral resonances corresponds to near field field enhancement [51].

The large electric field enhancement, the dependance of the resonance po-
sition to the dielectric properties of the material in the gap, the multiple
plasmon response suggests the application of SRR geometry in the plasmonic
sensor field, due to the possible multi-functional detection.

In the last few years many different studies has been done in order to exploit
this geometry for sensing purposes [4] [1] [3].

In this work we are proposing large array of SRR fabricated using X-Ray
Lithography in order to obtain large areas, tall structures in a fast litho-
graphic process. The fabrication on transparent substrate allows transmis-
sion analysis in normal incidence. The sensing potential of this structure will
be tested.

1.8 Surface Plasmon Resonance (SPR) Sensors

The idea behind the optical sensing is to convert the measurand, or the quantity being measured, to an output, tipically encoded into one of the characteristics of a light wave.

In a SPR sensor the measurand is the change of the refractive index of a dielectric medium. The propagation constant of the surface plasmon, excited at the interface between a metal film and a dielectric medium, is modified by the changes of the refractive index of the dielectric (superstrates). The changes alter the coupling condition between a light wave and the surface plasmon, which can be observed as a change in one of the characteristics of the optical wave interacting with the surface plasmon.

SPR sensors may be direct or indirect: in the former case, the measurand modulates the characteristics of the light directly, while in the latter, the measurand modulates an intermediate quantity which then modulates the light characteristics. On the basis of which characteristic of the light wave modulated by a surface plasmon is measured, SPR sensorsare classified as sensors with *angular*, *wavelength*, *intensity* or *phase modulation*.

SPR affinity biosensors are sensing devices incorporating biorecognition elements, which recognise and are able to interact with a selected analyte. The biorecognition elements are immobilized on the surface of a metal film supporting a surface plasmon. When a solution containing analyte molecules is brought in contact with the SPR sensor, analyte molecules bind to the molecular recognition elements. This binding produces an increase in the refractive index at the sensor surface. With the refractive index change the propagation constant changes, and this is determined by measuring a change in one of the characteristics of the light wave interaction with the surface plasmon.

SPR affinity biosensors belongs, then, to the indirect SPR sensors group.

Sensitivity, linearity, resolution, accuracy, reproducibility, dynamic range, limit of detection and limit of quantification are the main characteristics describing the performance of SPR sensors.

1.8.1   Sensitivity

Sensor *sensitivity* is the ratio of the change in a sensor output to the change in a measurand (slope of the calibration curve):

$$S = \frac{\partial Y}{\partial X} \tag{1.68}$$

Refractometric sensitivity describes the sensitivity of the SPR sensor to refractive index n and can be written as:

$$S_{RI} = \frac{\partial Y}{\partial n} \tag{1.69}$$

The sensitivity of an SPR biosensor to a concentration of analyte c can be written as:

$$S_c = \frac{\partial Y}{\partial c} \tag{1.70}$$

Sensitivity can be decomposed into two contributions:

$$S_c = \frac{\partial Y}{\partial c} = \frac{\partial Y}{\partial n_b} \frac{\mathrm{d}n_b(c)}{\mathrm{d}c} = S_{RI} S_{nc} \tag{1.71}$$

where S_{RI} and S_{nc} are, respectively, the sensitivity of the output to a refractive index profile change and the sensitivity derived from the refractive index change (n_b) caused by the binding of analyte (concentration c) to biorecognition elements.
The sensitivity S_{RI} is given by two contribution:

$$S_{RI} = \frac{\delta Y}{\delta n_{ef}} \frac{\delta n_{ef})}{\delta n_b} = S_{RI1} S_{RI2} \tag{1.72}$$

The first term depends on the method of excitation of surface plasmons and the modulation approach and it is referred as to an instrumental contribution. The second term describes the sensitivity of the effective index of a surface plasmon to refractive index and is independent of the modulation method and the method of excitation of SPP: it mainly depends on the profile of the refractive index.

1.8.2   Linearity

Sensor *linearity* defines the extent to which the relationship between the measurand and the sensor output is linear over the working range. It may concern either the measurand or refractive index. In general, linearity is specified in terms of maximum deviation from a linear transfer function over the

specific dynamic range. Sensors with linear transfer function are desirable as they require fewer calibration points to produce an accurate sensor calibration. However, response of SPR biosensors is usually a non-linear function of the analyte concentration and therefore calibration needs to be carefully considered.

1.8.3 Resolution

The *resolution* of a sensor is the smallest change in measurand which produces a detactable change in the sensor output. It is strictly related to the level of uncertainty of the sensor output, the *sensor noise*. The resolution σ_{RI} is typically expressed in terms of the standard deviation of noise of the sensor output, σ_{SO}, translated to the refractive index of bulk medium, $\sigma_{RI} = \sigma_{SO}/S_{RI}$.

Dominant sources of noise are the fluctuations in the light intensity emitted by the light source, shot noise associated with photon statistics, noise in conversion of the light intensity into electric signal by the detector. Noise in the intensity of light emitted by the light source is proportional to the intensity and its standard deviation σ can be given as $\sigma_L = \sigma_L^r I$, where σ_L^r is relative standard deviation and I is the measured light intensity. Shot noise is associated with random arrival of photons on a detector and corresponding random production of photoelectrons. Photon flux usually obeys Poisson statistics and produces a shot noise σ_S directly proportional to the square root of the detected light intensity: $\sigma_S = \sigma_S^r \sqrt{I}$, where σ_S^r is relative standard deviation. Detector noise consists of several contributions that originate mostly in temperature noise and its standard deviation σ_D is independent on the light intensity. The resulting noise of a measured light intensity σ_I is a statistical superposition of all the noise components and it is expressed as:

$$\sigma_I(I) = \sqrt{I^2(\sigma_L^r)^2 + I(\sigma_S^r)^2 + \sigma_D^2} \qquad (1.73)$$

In order to reduce the noise, light intensities are averaged: time averaging involves the average of time series of intensity from the same detector, spatial averaging the average of the output of multiple detectors. As in the time domain all the noise contributions behave independently, the time averaging of N spectra reduces the total noise as follows:

$$\sigma_I^{tN} = \frac{\sigma_I}{\sqrt{N}} \qquad (1.74)$$

The noise in the light intensity is translated to sensor output noise by the data processing algorithm that is used to generate the sensor output. Centroid

method uses a simple algorithm which finds the geometric center of the SPR dip under a certain threshold. The centroid is calculated as follows:

$$Y_C = \frac{\Sigma_i Y_i (I_{th} - I_i)}{\Sigma_i (I_{th} - I_i)} \tag{1.75}$$

where Y_i is the spectral position of the contributing intensity I_i, and I_{th} denotes the threshold value. In the case the noise of intensities detected by individual detectors can be treated as independent, the the resulting standard deviation of calculated dip position σ_{SO} can be derived as:

$$\sigma_{SO}^2 = \Sigma_i \left(\frac{\partial Y_c}{\partial I_i}\right) \sigma^2(I_i) \tag{1.76}$$

In the assumption that the portion of the SPR dip used by the centroid algorithm follows a lorentzian profile, we find the following esteeme for SPR resolution:

$$\sigma_{RI} = K \frac{1}{\sqrt{N}} \frac{\sigma_{th}}{d} \frac{w}{S_{RI}} \tag{1.77}$$

where N is the number of intensities used for the calculation of the centroid, σ_{th} is the total intensity noise at threshold, d is the difference of intensities at the SPR dip minimum and at the threshold, w is the width of the dip, S_{RI} is the bulk refractive index sensitivity of the sensor and K is a factor depending on the relative contributions of the sources of noise. The width of the SPR dip is directly correlated with its sensitivity and it can be shown that the ratio w/S_{RI} depends only weakly on the choice of coupler and modulation. The result shows that the sensor resolution is linearly dependent on the noise of measured signal and on the dip width, and inversely dependent on the depth of the the SPR dip. From these results the importance of optimizing resonance conditions looking for deep and narrow intensity dips. Best sensitivity values reach $1 \cdot 10^{-6}$ RIU (RIU=Refractive Index Unit) for grating coupler and $0.5 \cdot 10^{-6}$ RIU for prism coupler for angular modulation and orders of 10^{-5} and 10^{-6} RIU respectively for wavelength modulation.

1.8.4   Accuracy

Accuracy describes the closeness of agreement between a measured value of the measurand; it is usually expressed in absolute terms or as a percentage of error/output ratio.

1.8.5   Reproducibility

Sensor *reproducibility* is the ability of the sensor to provide the same output when measuring the same value of the measurand under the same

operating conditions over a period of time. Reproducibility is typically expressed as a percentage of full range.

1.8.6   Dinamic range

The *dynamic range* describes the span of the values of the measurand that can be measured by the sensor. In SPR biosensors it defines the range of concentration of an analyte which can be measured with specified accuracy and extends from the lowest concentration at which a quantitative measurement can be done.

1.8.7   Limit of detection

The *limit of detection* (LOD) of a biosensor describes the concentration of analyte, c_L, derived from the smallest measure, Y_L, that can be detected with reasonable certainty. It is given by:

$$Y_{LOD} = T_{blanck} + m\sigma_{blank} \tag{1.78}$$

where Y_{blank} is the mean of the blank (sample with no analyte) measures, σ_{blank} is the standard deviation of the blank measures, m is a numerical factor chosen according to the confidence level desired. As $c_{blank} = 0$, the LOD concentration c_{LOD} can be expressed as:

$$c_{LOD} = m\frac{\sigma_{blank}}{S_C} \tag{1.79}$$

To quantify the analyte concentration sometimes the *limit of quantification* (LOQ) is used. Analyte quantification is generally accepted to begin at a concentration equal to 10 standard deviations of the blank.

Chapter 2

Structure simulation

Simulation software offers a fundamental contribution to the pattern design.
In this chapter we present the simulated optical response of the SRR to visible-near infrared light illumination. The structure has been modelled by the software COMSOL Multiphysics.
COMSOL Multiphysics is a finite element analysis, solver and Simulation software / FEA Software package for various physics and engineering applications, especially coupled phenomena, or multiphysics.
We studied the optical response of the SRR array structure. The designed unit cell consists of a gold SRR upon a layer of Indium Tin Oxide (ITO) and a substrate of glass. Solving the full three dimensional electromagnetic problem, we obtained the transmittance of the structure.
We analyzed the case of normally impinging plane wave with electric field polarized parallel and perpendicular to the gap, focusing our attention on the peaks in transmittance spectra. Near field analysis of the distribution of the electric and magnetic field enhancement corresponding to transmittance peak has been used in order to understand the origin of the resonances.
The analysis of the simulated spectra has been performed in the Matlab environment.

2.1 The Finite Element Method (FEM)

The Finite Elements Method (FEM) is a numerical technique for finding approximate solutions of partial differential equations (PDEs), as well as of integral equations. The solution approach is based either on eliminating the differential equation completely (steady state problems), or rendering the PDE into an approximating system of ordinary differential equations, which

are then numerically integrated.

The commercial software COMSOL Multiphysics version 4.2, which we had at our disposal for the calculations, fully implements the FEM.

This kind of numerical analysis aims to provide a realistic simulation of every quantity of interest in our model (essentially magnetic and electric fields) as a function of space and time. In other terms, it is supposed to show us what happens in our system, as long as the phenomena involved can be described in the theoretical frame we consider, classical electromagnetism.

However, the simulation not always allows us to fully understand reality. In fact, the higher is the accuracy required to the simulation the more are the degrees of freedom which need to be taken into account. Even providing the required calculation power, the final result is such a wide ensemble of calculated variables that its complexity resembles that of the reality itself. On the other hand, a reliable simulation of reality not only allows quick and easy tests of physically meaningful models but can also suggest more targeted and significant experiments, having previously performed geometry optimizations. Further, any deviations between experimental data and simulated ones will indicate the presence of new physics not taken into account. One of the main advantages of the FEM, in comparison to the more common methods, like finite differences method, as an example, lies in the flexibility concerning the geometry of the domain where the PDE is to be solved. Moreover the FEM is perfectly suitable as adaptive method, because it makes local refinements of the solution easily possible. The method does not operate on the PDE itself: the PDE is transformed to a equivalent variational or weak form.

The idea of the FEM is to discretize the domain into finite elements and define function on each the element, which vanishes elsewhere.

The exact field is approximated by a superimposition of functions of a particular basis. The basis functions are usually not defined directly: a function type, the so called *ansatz* function (e.g. linear or quadratic polynomial), is selected instead. The finite element method is defined by the choice of the basis.

2.2   Split Ring Resonators

The design on the SRR was based on the capability of the fabrication techniques, mainly X-Ray Lithography (XRL), plasma etching and electro-chemical growth.

The aim of the simulation step is the design of the SRR and the study of the plasmonic resonances in the wavelength range of interest. We focused on the

following SRR geometry:

l (nm)	w (nm)	d (nm)	a (nm)
390	120	60	460

where l is the lateral side of the SRR, w is the width, d is the gap size and a is the SRR array period (see Figure 1.12).The other geometrical parameter of the structure, the height of the SRR h, has not being reported here because the study of the dependance of the resonances to this parameter has been analyzed in the following sections, in the range $h = 200 - 400nm$.
We simulated the response of the geometry in the visible-near infrared (VIS-NIR) range of wavelength, $400 - 1100nm$.
The structures behavior has been analyzed in normal light incidence (incident angle of illumination 0°) and electric field polarized perpendicular and parallel to the gap (respectively defined as y- and x-axis), in order to explore the resonances of the structure and their origins.
The fabrication step of this thesis aims to the production of gold SRR array on transparent substrate (ITO on glass) to perform analysis in transmission. In order to adhere to this goal, the materials composing the unit cell in the simulation are the same of the fabricated sample: gold for the SRR and ITO and glass for the substrate.

2.2.1   Electric field polarized perpendicular to the gap

In this section we analyze the simulated transmittance spectra in the range of wavelength is $400 - 1100nm$, when the electric field is polarized perpendicular to the gap (Figure 2.1).
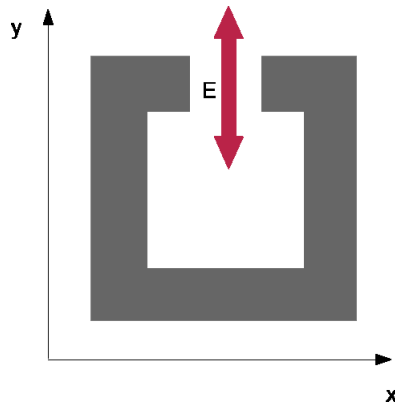
Figure 2.1: Electric field polarized perpendicular to the gap along the y-axis

The unit cell replies the final structure for the fabricated sample: the SRR is

in gold, over a substrate in ITO ($100nm$) and glass. The surrounding media is air.

We report the spectra for $h = 200nm$ (Figure 2.2), $h = 300nm$ (Figure 2.3) and $h = 400nm$ (Figure 2.4).   In order to understand the origin of the
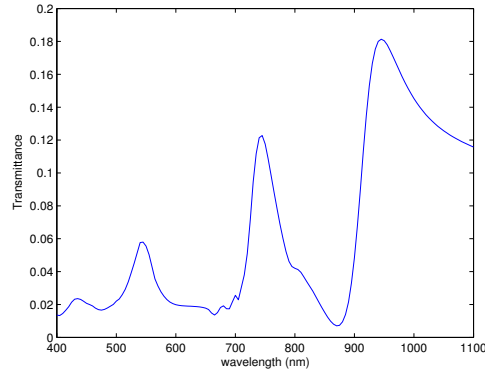
Figure 2.2: Transmittance over $\lambda = 400 - 1100nm$, for $h = 200nm$, electric field polarized perpendicular to the gap.
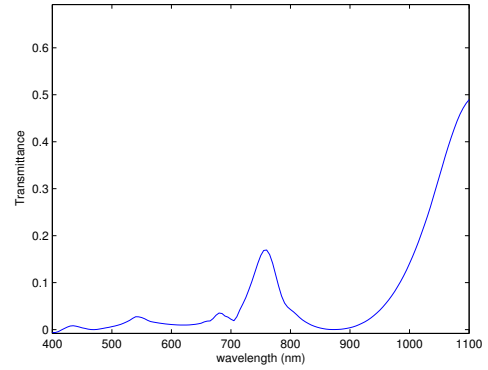
Figure 2.3: Transmittance over $\lambda = 400 - 1100nm$, for $h = 300nm$, electric field polarized perpendicular to the gap.
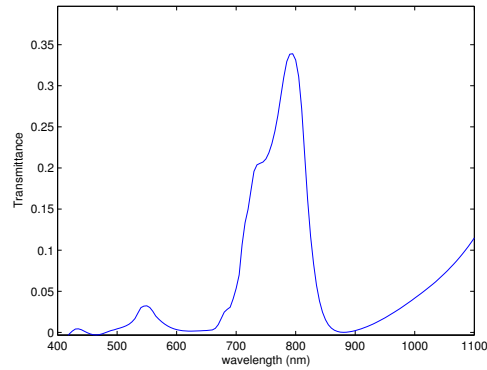
Figure 2.4:   Transmittance of $390nm$ side SRR, $h = 400nm$, electric field polarized perpendicular to the gap.

resonances, we are reporting the near field images for the electric and mag-

netic field norm in Figures 2.5, 2.6, 2.7, 2.8, for $h = 400nm$[1] at $\lambda = 790nm$, wavelength corresponding to the peak in Figure 2.4.
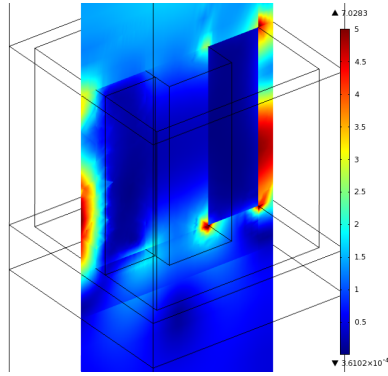
Figure 2.5: Near field image of $|\mathbf{E}|$ in yz cross section at $\lambda = 790nm$. Electric field of the impinging light polarized perpendicular to the gap.
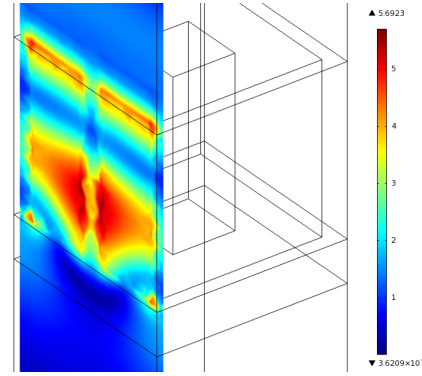
Figure 2.6: Near field image of $|\mathbf{E}|$ in xz cross section at $\lambda = 790nm$. Electric field of the impinging light polarized perpendicular to the gap.
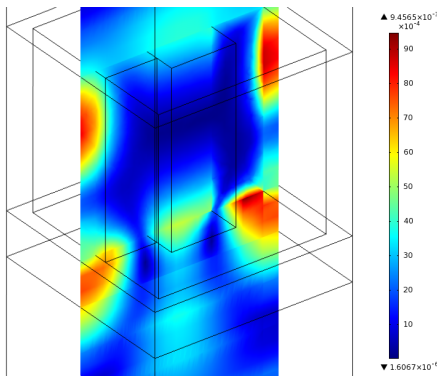
Figure 2.7: Near field image of $|\mathbf{H}|$ in yz cross section at $\lambda = 790nm$. Electric field of the impinging light polarized perpendicular to the gap.
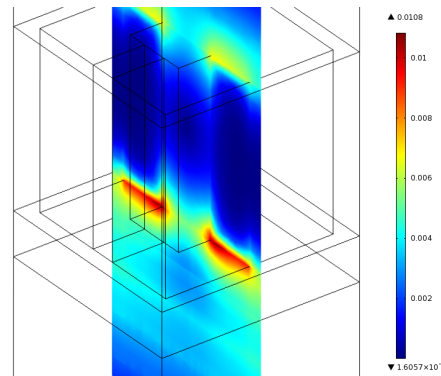
Figure 2.8: Near field image of $|\mathbf{H}|$ in xz cross section at $\lambda = 790nm$. Electric field of the impinging light polarized perpendicular to the gap.

As evidenced in Figures 2.5, 2.6 and 2.7, the enhancement of the electromagnetic field does not occur in the gap area, but between two contiguous SRR in the yz plane. In particular, Figure 2.6 shows the electric field enhancement

---

[1]The choice to analyze the case $h = 400nm$ is only due to the clarity of the near field images in this configuration.

in the area between the gap of a SRR and the bottom of the next SRR.
Our hypothesis is that the peak in the transmittance and the correspondent
enhancement in the near field are due to Fabry-Pérot resonances between
two contiguous SRR [52].
An analogous enhancement of the field is expected for the other polarization
in the xz plane at the same wavelength, as a proof of our hypothesis.

2.2.2   Electric field polarized parallel to the gap

In this section we analyze the simulated transmittance spectra in the
range of wavelength $400 - 1100nm$, when the electric field is polarized par-
allel to the gap (Figure 2.9). We are expecting an electric field enhancement
in the gap region.
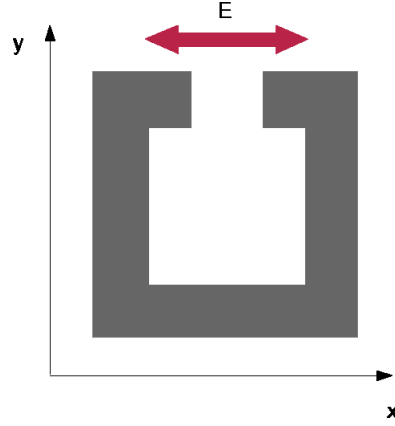
Figure 2.9: Electric field polarized parallel to the gap along the x-axis

Also in this case, the unit cell replies the final structure for the fabricated
sample: the SRR is in gold, over a substrate in ITO ($100nm$) and glass. The
surrounding media is air.
We report the spectra for $h = 200nm$ (Figure 2.10), $h = 300nm$ (Figure 2.11)
and $h = 400nm$ (Figure 2.12). On the same graph we report the simulated
spectra for the opposite polarization of the impinging electric field in order
to compare the position of the peaks.
A first set of peaks in the range $700 - 900nm$ is present for each spectrum,
around the same wavelengths corresponding to the resonances excited by the
perpendicular polarization.
To analyze the Fabry-Pérot hypotesis on the origin of the resonances in the
perpendicular polarization, we consider the same case as the previous Sec-
tion, the peaks around $800nm$ in the spectrum of the simulated SRR having
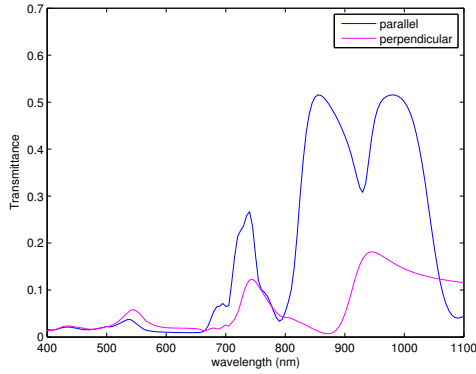
Figure 2.10: Polarization comparison for $h = 200$. In blue: transmittance over $\lambda = 400 - 1100nm$, electric field polarized parallel to the gap. In red: electric field polarized perpendicular to the gap.
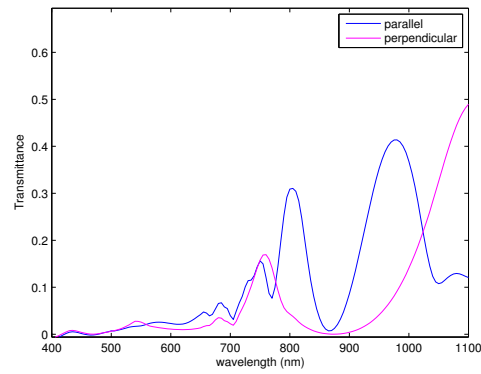
Figure 2.11: Polarization comparison for $h = 300$. In blue: transmittance over $\lambda = 400 - 1100nm$, electric field polarized parallel to the gap. In red: electric field polarized perpendicular to the gap.
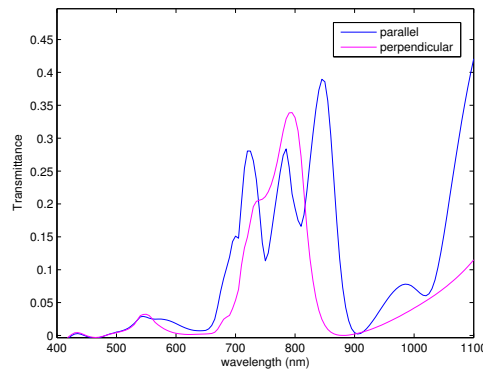
Figure 2.12: Polarization comparison for $h = 400$. In blue: transmittance over $\lambda = 400 - 1100nm$, electric field polarized parallel to the gap. In red: electric field polarized perpendicular to the gap.

$h = 400nm$. From Figure 2.12 it is possible to notice the central transmittance peak of the parallel polarization spectra falls around $\lambda = 790nm$, position of one of the trasmittance peaks for the perpendicular polarization.

When we analyze the near field image of the norm of the electric and the magnetic field in the parallel polarization for $h = 400$ at $\lambda = 790nm$, we can observe a strong, expected enhancement of the electric (Figure 2.13) and magnetic (Figure 2.15) fields in the gap, but also a resonant response between the lateral walls of two adjacent SRR (Figures 2.14, 2.16).
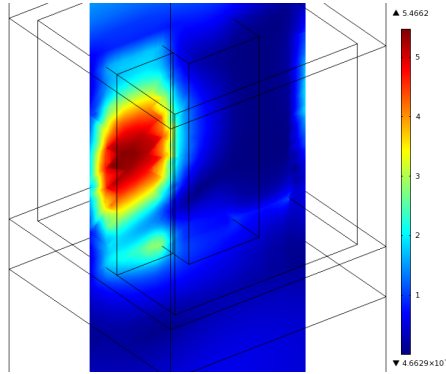
Figure 2.13:   Near field image of $|\mathbf{E}|$ in yz cross section at $\lambda = 790nm$, $h = 400nm$. Electric field of the impinging light polarized parallel to the gap.
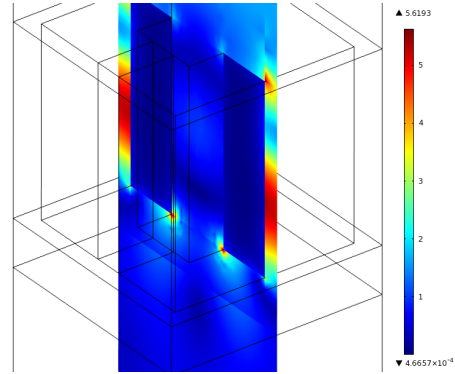
Figure 2.14:   Near field image of the norm of $|\mathbf{E}|$ in xz cross section at $\lambda = 790nm$, $h = 400nm$. Electric field of the impinging light polarized parallel to the gap.
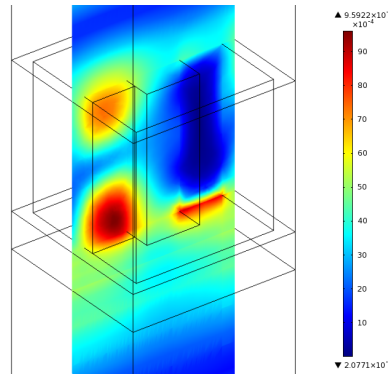
Figure 2.15:   Near field image of $|\mathbf{H}|$ in yz cross section at $\lambda = 790nm$, $h = 400nm$. Electric field of the impinging light polarized parallel to the gap.
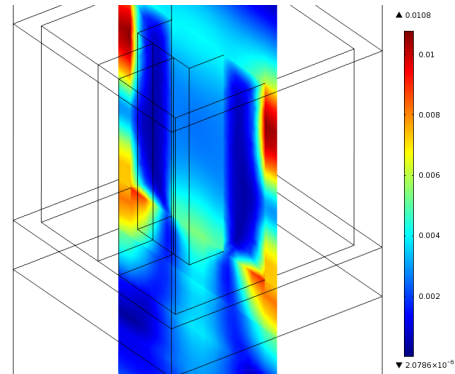
Figure 2.16:   Near field image of $|\mathbf{H}|$ in xz cross section at $\lambda = 790nm$, $h = 400nm$. Electric field of the impinging light polarized parallel to the gap.

A qualitative comparison between the enhancement of the magnetic field

in the yz plane for the perpendicular polarization (Figure 2.7) and the enhancement of the magnetic field in the xz plane for the parallel polarization (Figure 2.16), both at $\lambda = 790nm$, seems to confirm our hypothesis on the Fabry-Pérot origin of this resonance. This remark lead us to conclude the resonances, in the parallel polarization case, corresponding to the transmittance peaks and located at the same wavelength of the perpendicular polarization case, are a combination of the plasmonic resonances occurring in the gap area and the Fabry-Pérot resonances between the SRRs.

The simulations evidence how the height influences structure and shape of the peaks, in particular the first set of peaks every present simulated spectrum shows in the $700 - 900nn$ range: as the height increases, the centre of the set is red shifted ($720nm$ for $h = 200$, $780nm$ for $h = 300$ and $800nm$ for $h = 400$), the number of peaks increases and the width of the set enlarges. This effect can be due to the higher order plasmonic modes a taller gap may permit [53] [50] (Figure 2.17) and to the presence of resonances due to field enhancement between the SRRs.
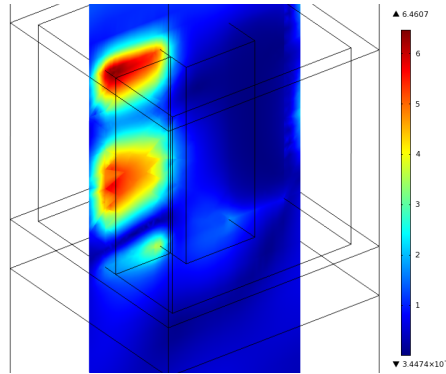
Figure 2.17: Near field image of $|\mathbf{E}|$ in yz cross section at $\lambda = 730nm$, $h = 400nm$, evidencing the higher order plasmonic modes. Electric field of the impinging light polarized parallel to the gap.

Let us consider, now, the other peaks in the transmittance spectra. In order to study the origin of the resonance evidenced by those peaks, we consider the spectrum for $h = 200nm$, since it present two peaks which do not correspond to resonances for the other polarization.

The electric field enhancement in the gap area for $h = 200nm$, corresponding to excited plasmonic modes, for $\lambda = 855nm$ and $\lambda = 980nm$, respectively in Figure 2.18 and Figure 2.19. In the first case the presence of two spot in the gap area indicates a probable superimposition of the resonance at $\lambda = 855nm$ (upper spot) and the resonance at $\lambda = 980nm$ (lower spot).

The near field images of the norm of the magnetic field in the xz plane
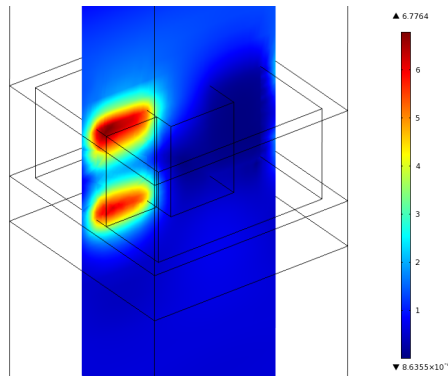
Figure 2.18: Enhancement of the electric field at $\lambda = 855nm$ in the gap area for $h = 200nm$ (yz cross section). Electric field polarized parallel to the gap.
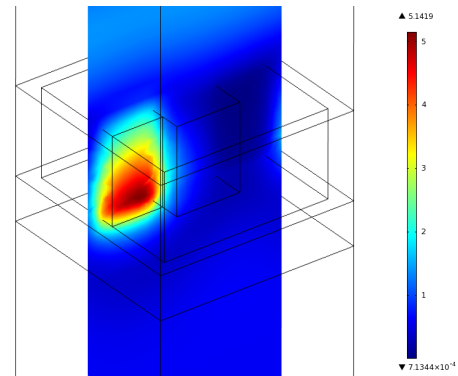
Figure 2.19: Enhancement of the electric field at $\lambda = 980nm$ in the gap area for $h = 200nm$ (yz cross section). Electric field polarized parallel to the gap.
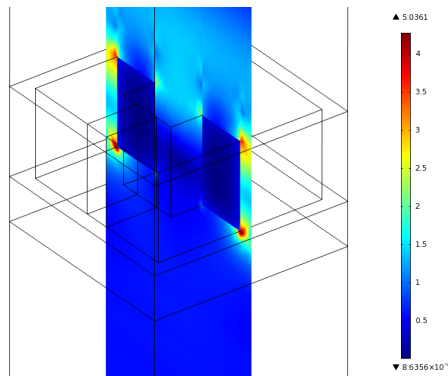
Figure 2.20: Enhancement of the electric field at $\lambda = 855nm$ in the gap area for $h = 200nm$ (xz cross section). Electric field polarized parallel to the gap.
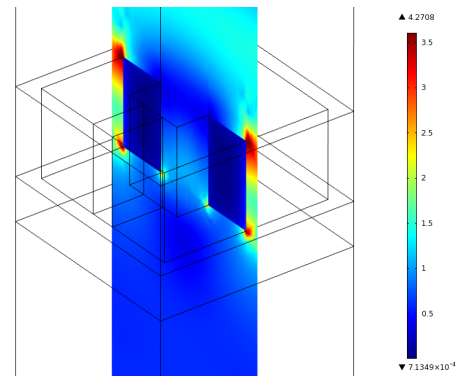
Figure 2.21: Enhancement of the electric field at $\lambda = 980nm$ in the gap area for $h = 200nm$ (xz cross section). Electric field polarized parallel to the gap.

(Figures 2.23 and 2.23) show a different field distribution compared to the Fabry-Pérot resonace evidenced previously (Figures 2.7 and 2.16). We may conclude the origin of the resonances is due to the electromagnetic enhancement occurring in the gap and a minor contribution due to the enhancement between the SRRs (Figures 2.20 and 2.21).

The peaks in the transmittance for $h = 300nm$ and $h = 400nm$ correspond
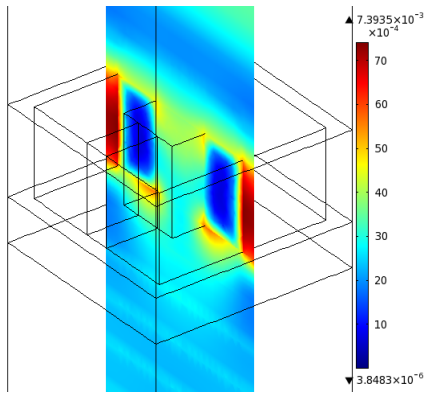
Figure 2.22: Enhancement of the magnetic field at $\lambda = 855nm$ for $h = 200nm$ (xz cross section). Electric field polarized parallel to the gap.
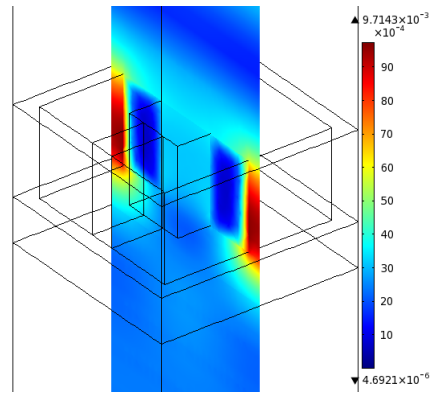
Figure 2.23: Enhancement of the magnetic field at $\lambda = 980nm$ for $h = 200nm$ (xz cross section). Electric field polarized parallel to the gap.

to analogous near field electromagnetic field enhancements.

2.3   Sensitivity test

A fast, preliminary and qualitative analysis of the sensitivity of the SRR to the changes in the refractive index of the environment, and consequently in the gap area, can be done simply by changing the bulk refractive index of the material surrounding the SRR.

We analyze the simulated transmittance spectra in the range of wavelength is $500 - 1100 nm$, reduced compared to the previous result since the response in the $400 - 500 nm$ range is poor. The unit cell consists of a SRR in gold over a substrate in ITO ($100 nm$) and glass. We limit the analysis to a single height ($h = 300 nm$). The simulation has been obtained for four different refractive index for the media surrounding the SRR: $n_{sup} = 1$, $n_{sup} = 1.05$, $n_{sup} = 1.1$ and $n_{sup} = 1.2$. We limited our analysis to the polarization of the electric field parallel to the gap of the SRR, in order to exploit the electric field enhancement in the gap area.

The model differs from the former ones in the gold refractive index: the literature value implemented in the previous section have been substituted by the value collected by ellipsometry on a fabricated gold sample. The main difference of the obtained spectra compared to the previous ones is the broadening of the first set of peaks. The new spectra is red shifted.

The geometric parameter of the model SRR are, then:

l (nm)	w (nm)	d (nm)	h (nm)	a (nm)
390	120	60	300	460

The comparison between the transmittance spectra for the four refractive index is shown in Figure 2.24. The increasing in the refractive index of the media surrounding the SRR causes a red shift of the transmittance peaks. The first peak ($\lambda = 780 nm$ at $n = 1$) is shifted by a smaller quantity compared to the second ($\lambda = 850 nm$ at $n = 1$) or the third peak($\lambda = 1030 nm$ at $n = 1$).

The performed simulation it is not sufficient *per se* to calculate the expected sensitivity of the structure. Nevertheless, the accurate simulation of the response of the 3D structure to the deposition of a thin layer of material would require a very high computation power. Further simulation have already been scheduled.

The qualitative analysis performed here encourages, however, the test of the structure for sensing purposes.
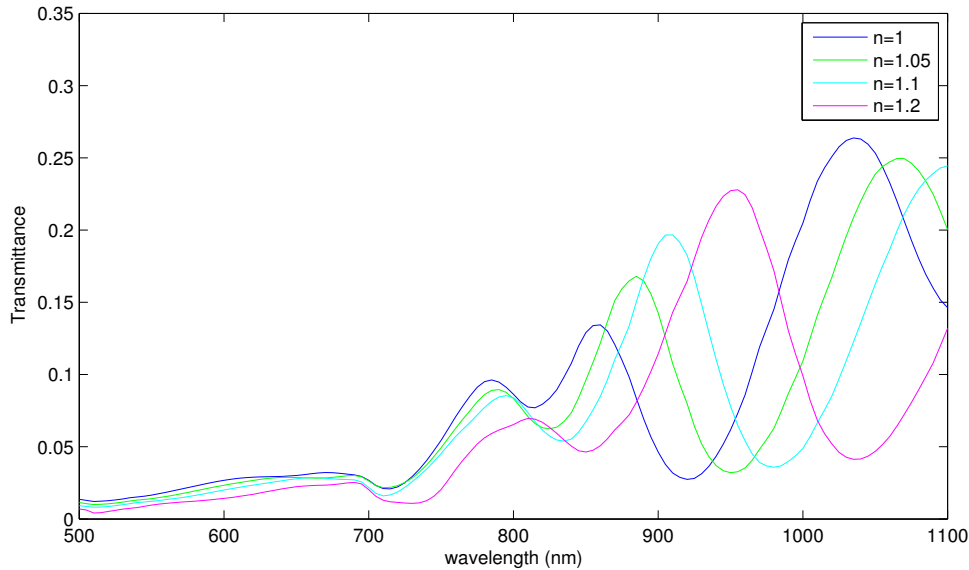
Figure 2.24: Transmittance spectra simulated for different refractive index of the media surrounding the SRR. Blue line: $n_{sup} = 1$. Green line: $n_{sup} = 1.05$. Cyan line: $n_{sup} = 1.1$. Red line: $n_{sup} = 1.2$. A red shift is present.

2.4 Conclusion

In this part of the project we designed the structure and analyzed the response of a geometry for the SRR, using the finite element analysis software COMSOL.

The model reproduces the fabricated sample: a gold SRR on a thin layer of ITO on glass.

The response of the structure has been simulated in transmittance with normal impinging light, covering the visible-infra red wavelength range ($400 - 1100nm$). Two polarization of the electric field to the gap of the SRR have been analyzed.

The analysis of the near field corresponding to the peaks in the transmittance spectra evidenced the origin of the resonances as plasmonic modes in the gap of the structure and Fabry-Pérot modes between the SRRs. In particular, the analysis of the near field images of the simulation in which the electric field is perpendicular to the gap, evidences a resonance between the SRRs found at the same wavelength in the other polarization simulation results, making the first set of peak in transmittance as the superimposition of plasmonic resonances in the gap and Fabry-Pérot resonances. The electric

field polarized parallel to the gap, on the other hand, causes a strong field enhancement and confinement in the SRR gap region.

The behavior of the resonances has been studied while changing the SRR geometric parameters and the refractive index of the surrounding media.

The changes in the height strongly influences the shape and the position of the peaks in transmittance.

The qualitative test performed on the structure response to refractive index changes evidenced red shift of the transmittance spectra as the refractive index increases.

The enhancement of the electromagnetic field in the gap region may be exploited, in principle, for sensing purposes.

Chapter 3

Methods

The fabrication of the plasmonic devices described in the previous chapters requires the use of different techniques, from the preparation of the sample, to the lithography, to the finalization and characterization.

In this chapter we are presenting the fabrication and characterization techniques exploited in the SRR samples production. The main fabrication technique we used is X-Ray lithography (XRL), a parallel transfer technique using X-rays flux to transfer a pattern from a mask to the sample. XRL itself and sample fabrication request the use of many other techniques: UV Lithography (UVL), wet and dry etching, Electron Beam Lithography (EBL) and electrochemical growth among the others.

Once produced, the samples are characterized. Scanning Electron Microscopy (SEM) and Ellipsometry have been employed in this thesis for the samples characterization.
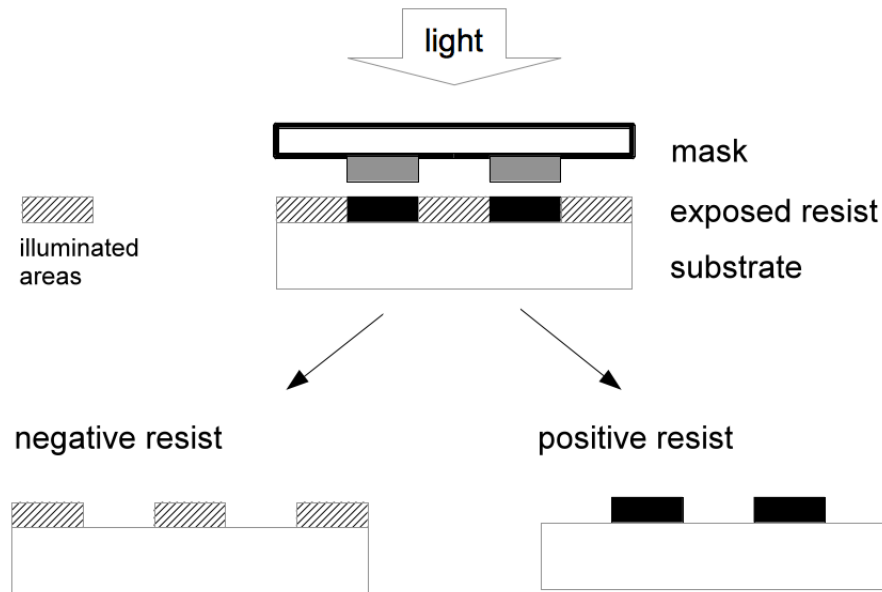
Figure 3.1: Negative and positive resist behavior to exposure. Positive exposed resist is removed during development, negative exposed resist remains.

3.1   Fabrication techniques

3.1.1   Resist

A photoresist is a solution composed mainly by a polymer, a sensitizer and a casting solvent. The polymer changes structure when exposed to radiation, the sensitizer controls the photochemical reactions, the solvent allows the deposition of the resist on the substrate (see 3.1.2) and the formation of thin layers on the surface to be covered.

The tone of the photoresist describes its behavior to exposure. When the photoresist is of the *positive* type, the photochemical reaction during exposure weakens the polymer causing scission of the main and side polymer chains, resulting in a higher solubility of the exposed resist. The development rate of the exposed resist is, then, faster than the development rate of the unexposed resist. When the photoresist is of the type called *negative*, the exposure causes the strengthening of the polymer by random cross-linkage of main or pendant side chains, becoming less soluble.

Figure 3.1 shows exposure effects on both positive and negative resist.

3.1.2 Spin coating

One of the techniques used to cover a surface with a thin, homogeneous layer of photoresist is the spin coating. The photoresist is dispensed from a viscous solution onto the sample, which is then spun at high speed. The spinner vacuum chuck holds the sample in place.

The speed at which the sample is spun varies from 500 to 8000 revolutions per minute (rpm) and depends on the viscosity of the resist and the required film thickness. At these speeds, centrifugal forces causes the solution to flow to the edges, where it builds up until the surface tension is exceeded. The rotation at high speed causes the resist to deposit homogeneously. The resist thickness is a function of spin speed, solution concentration and molecular weight and can be valued using the empiric expression [54]:

$$T = \frac{K C^{\beta} \eta^{\gamma}}{\omega^{\alpha}} \qquad (3.1)$$

where K is a calibration constant, C the polymer concentration in $g/100ml$ solution, η the intrinsic viscosity, ω the speed (rpm) and α, β, γ parameters to be determined. The quality of resist coating determines the density of defects transferred to the final structure.

After spin coating the resist still contains up to 15% solvent and may contain stresses: the resist covered sample is then soft baked (this operation is also known as *pre exposure bake*), to promote residual solvent evaporation, surface adhesion and to reduce the stresses. Temperature and time of the soft bake are specific to every resist. The negative resist often requires a post exposure bake after exposure to enhance cross-linkage.

3.1.3 X-Ray Lithography

X-Ray lithography (XRL) belongs to the class of parallel lithographic techniques (UV, nanoimprinting, casting...) [11]. This means that the pattern can not be originated, but just replicated. All constituent points of the pattern are addressed at the same time, and the process is typically fast. However, the pattern has to be first encoded into an object, the mask, and then transferred entirely in a single parallel step (Figure 3.2).

X-ray masks consist of absorbing patterns supported by a transparent mask-carrier, which has a weak absorption of X-rays in the range of photon energies required for exposures. In XRL exposure the X-rays illuminate the back of the mask, which is in contact to the resist covered sample. As a first step, the beam impinges on the mask, then the ray flux continues its path through it: the photon either passes through the transparent areas of the mask (usually
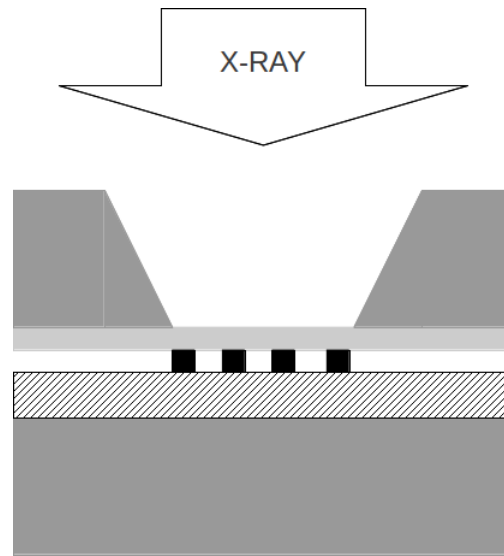
Figure 3.2: This figure shows the X-Ray lithographic process, as the illumination of the mask-sample complex

silicon nitride membrane) or is absorbed by the absorber areas (gold pattern). The exiting image of flux from the bottom of the mask is absorbed by the photoresist, creating photoelectrons. A latent image, corresponding to the geometric mask absorber pattern, is instantly formed in the photoresist layer, due to the photoelectron-induced changes to its molecular weights and refractive index.

There may be different X-Ray sources [10]:

- **electron impact sources:** x-rays are produced by the impact of electrons on a solid target, both by stripping of the target inner nucleous electrons and continuous *Bremsstrahlung*;

- **plasma sources:** plasma of multimillion-degree temperatures can emit intense x-ray pulses: a focused laser beam impinges upon and vaporize a thin iron alloy film taget, coupling its energy into a spatial metal vapor, creating dense million degree microplasma temperatures; about 10% of the laser pulse energy is converted to a soft x-ray energy spectrum;

- **synchrotron radiation sources:** when a charge moves at relativistic speeds following a curved trajectory, a radiation emission occurs, limiting charge energy. This effect, undesired in the case of elementary particles experiments, can be exploited for XRL application, using this emitted radiation as a x-ray source. Synchrotrons are the brightest X-ray sources for lithography.
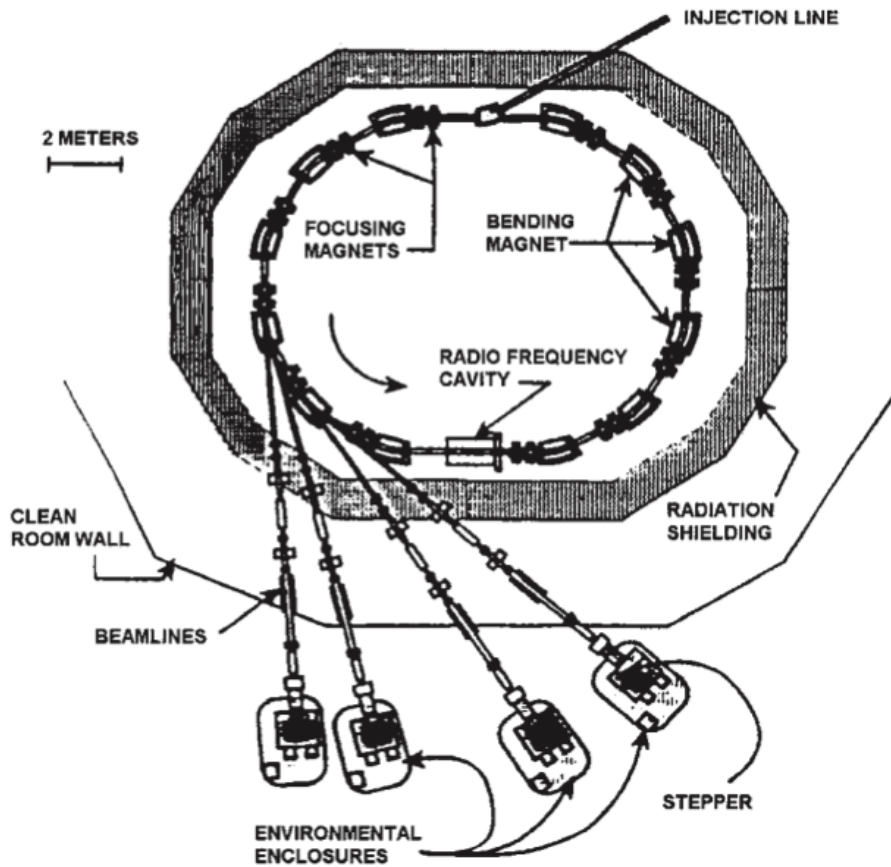
Figure 3.3: Scheme of electron storage ring [10]

In this work we took advantage of the beamline of LILIT (Laboratory for Interdisciplinary LIThography) on Elettra synchrotron (Trieste) (see Appendix A for more information): we will, therefore, limit ourselves below to the discussion of this source.

Synchrotron radiation and irradiation system

Synchrotrons are accelerators capable of producing stable beam of particles of very high energy (Figure 3.3). Synchrotron basic function is to capture and store electrons which are generated by an injector system. Those electrons are kept in stable orbits that close upon themselves and are defined by the action of several magnets, used to define the orbit (bending magnet) and to focus (focusing magnet) the electrons. Electrons energy in the ring is

given by [55] [56]:

$$E \approx 0.3 \frac{GeV}{Tm} B \cdot r \tag{3.2}$$

It is well known that when a charged particle is subjected to a radial acceleration it emits electromagnetic radiation tangentially to the circular electron path (*Bremsstrahlung*). The energy lost in the emission process is restored in a radio frequency (RF) cavity, which accelerates the electrons back to the storage ring energy.

For XRL application the X-ray emission is highly desired. The most simple device that generates photons by bending the electron beam is represented by bending magnets, that produce a single deflection of the beam, whereas other devices, such as undulators and wigglers, produce multiple deflections. The spectrum of the radiation emitted at a bending magnet depends on the electron energy and on the intensity of the magnetic field (or equivalently on the radius of curvature of the electron trajectory), and can be parameterized by the critical energy:

$$E_c = \hbar \omega_c = \frac{3e\hbar B}{2m} \gamma^2 \tag{3.3}$$

where $\gamma = E_e/(mc^2)$ is the energy of the accelerated electrons in the storage ring, normalized to their rest energy. It is possible to obtain the photon flux at a given energy considering the critical energy and the total intensity, which depends linearly on the current circulating in the ring, by superimposing the curves representing photon flux. All curves representing the photon flux from a bending magnet, indeed, can be superimposed on each other if plotted versus the photon energy normalized to the critical energy E_c, and after normalization to their total intensity. The lower end of the spectrum is in the IR wavelength regime. The flux raises smoothly as a function of photon energy until the critical energy E_c, and then drops rapidly (Figure 3.4). The critical wavelength corresponding to the critical energy is given by:

$$\lambda_c(nm) = \frac{1.864}{E_e^2(GeV)B(T)} \tag{3.4}$$

Elettra Syncrotron operates at two regimes: electron energy of 2.0 GeV and magnetic field of 1.2 T for bending magnets, or 2.4 GeV and 1.45 T. Therefore, the critical wavelength in these two operational regimes are 0.39 nm and 0.22 nm, corresponding to a critical energy of 3.2 keV and 5.6 keV, respectively.

The radiation from a bending magnet is emitted mostly within a narrow cone of angular aperture γ^{-1} (in radiant), whose axis is directed along the instantaneous direction of the electron trajectory. Since in the presence of a
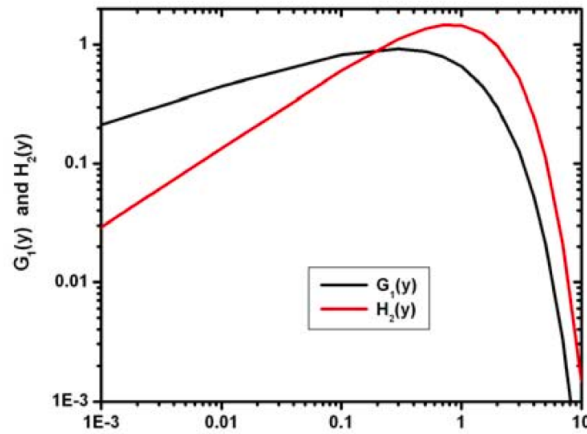
Figure 3.4: The function $H_2(y)$ representing on-axis photon flux from bending magnet and $G_1(y)$ representing the vertically integrated photon flux, as a function of the photon energy normalized to the critical photon energy [11]

magnetic field the trajectory is circular, the emission cone sweeps a "wide" angle, corresponding to the deflection that the electron beam has undergone in the horizontal plane due to the action of the bending magnet.

The emitted radiation has to be delivered from the source to the experimental room in order to be used for XRL, propagating inside a ultrahigh vacuum beamline.

A series of elements, inside the ultrahigh vacuum beamline, are interposed between the X-ray source and the mask/sample assembly for filtering the spectrum and shaping the beam, typically:

- filters

- mirrors

- slits or windows

- a stepper or a scanner

The length of a typical beamline is in the range of tens of meters, which allows to consider as a first approximation planar the electromagnetic waves when they reach the mask/sample assembly.

Along the beamline the radiation interacts with a series of different optical elements: to select the wavelength spectral window and adjust the beam shape and position, the beam can be let to pass through a series of foils of different material and to impinge on one or more mirrors. The wide energy range the

bending magnet can cover may be too broad to provide controlled conditions for lithography. Whereas the hard X-ray region, with photon energy higher than 5 keV and up to 10 keV, can be very useful for exposing sensitive materials thicker than hundreds of microns, only in the spectral range between 1 and 2 keV the highest lithographic resolution can be achieved by the so called "soft X-ray lithography" (High Resolution XRL).

Usually the first element the beam impinges on is a mirror or a couple of mirrors, acting as a low energy pass filters, redirecting and reshaping the beam and filtering out the high energy part of the spectrum. X-rays mirrors exploit the phenomenon of total external reflection. In the X-rays the refractive index is lower than 1, determining that the total reflection takes place passing from a lower density to a higher density material.

The spectral distribution which is employed in the exposure is controlled by a combination of mirrors and absorbers, acting as a band pass energy filter. A beryllium window is generally present for isolating the part of the beamline under high vacuum conditions (10^{-9} $mbar$ or better) and a part of beamline fluxed with Helium at a pressure of 1 atm and open to the external atmosphere. The role of the Helium in the terminal, open part of the beamline, is to displace from the trajectory of the X-ray beam the atmospheric gases (oxygen, nitrogen and water vapor),and to keep under the same He atmosphere also the mask/sample assembly. Helium also stops or slows down high energy photoelectrons generated by the interaction of photons with the mask that otherwise would cause unwanted exposure of the resist.

Finally, the beam is delimited in the horizontal plane by the slits along the beamline. This results in a horizontal "stripe" of radiation that, in the experimental room, is typically of 10-50 mm in the horizontal direction and of the order of the millimeter in the vertical one.

To expose larger area the assembly of mask and sample held together are scanned vertically, using a scanner. This operation is also fundamental to perform a spectral and intensity average of the photon beam.

X-Ray mask

As previously told, XRL is a parallel technique, able to reproduce a pattern, not to originate it. The role of masks, then, is that of selecting where the impinging radiation would be let to reach the resist and where not. The x-ray mask production is one of the crucial aspects of x-ray lithography. The mask must resist many exposure, without distortion, be robust and relatively easy to handle. To achieve good contrast it should be composed by a transparent support and a highly absorbing pattern [13].

A mask typically consist of a patterned absorber layer (usually a heavy
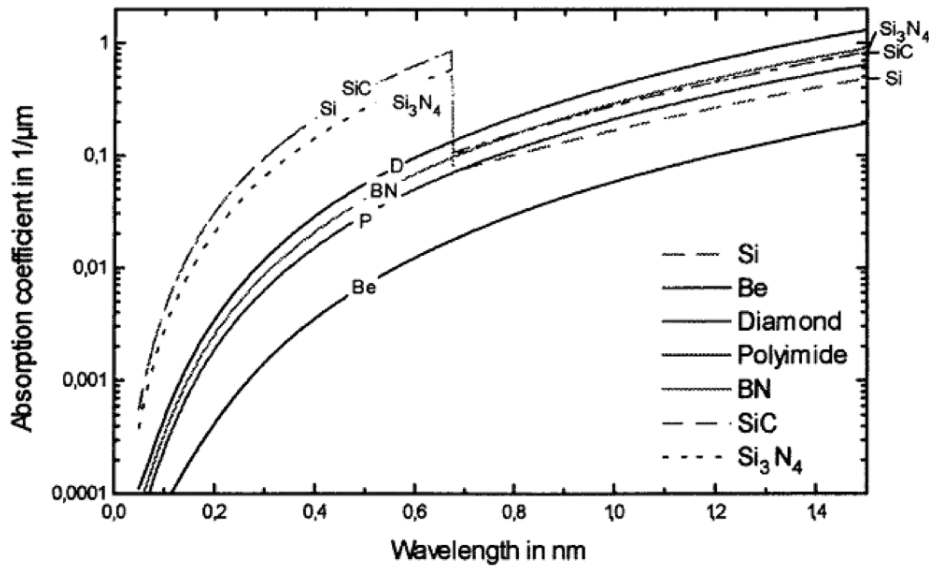
Figure 3.5: Absorption coefficient of selected material suitable as XRL mask substrate, as a function of wavelength [12]

metal) and a plate or a membrane supporting it, made of low-atomic number, weakly absorbing materials. For hard XRL the choice for pattern support are beryllium, carbon (amorphous or glassy graphite), polyimide, with thickness ranging from about 50 to 1000 μm, while thin membranes (0.5 to 4 μm) of silicon nitride, silicon carbide, diamond (Diamond Like Carbon (DLC)) are used with softer radiation (Figure 3.5). The requirement about the pattern support is to remain as much undistorted as possible against the effect of stress introduced by the absorber layer: the absorber layer has usually an inner residual stress that, once patterned, induces a non-uniform strain in the membrane, resulting in a distortion of the pattern itself. Moreover, the membrane has to be highly stable against the distortions caused by heating during irradiation.

Due to safety and cost reasons, the most common choice for the support is silicon nitride (Si_3N_4).

The absorber material must have a high atomic number and density, in order to obtain a contrasted shadow pattern interposing the absorber along the trajectory of the X-ray beam. The choice of the material to be used as mask absorber is mainly dictated by the type of technological processes that is selected for their deposition on the substrate and for the patterning. One possibility is the "additive" process, consisting of adding the material to the substrate after defining the pattern, which serves as a template for
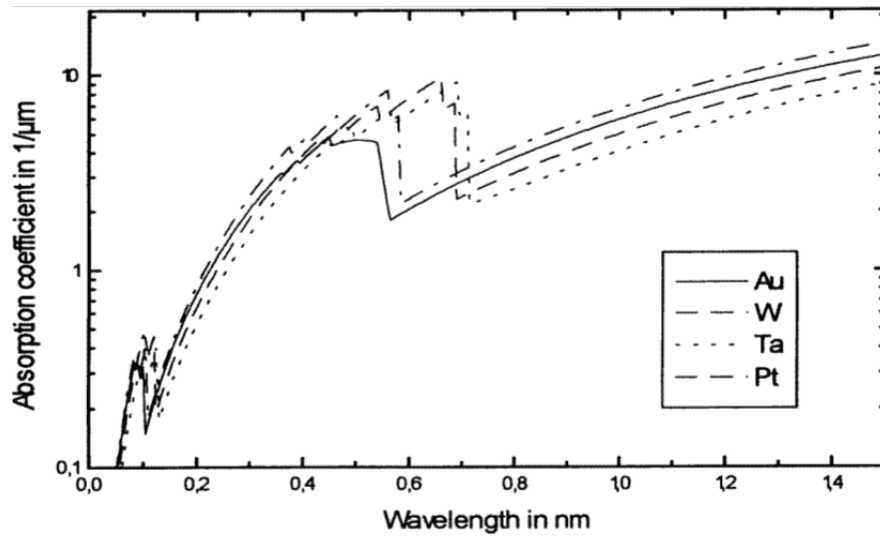
Figure 3.6: Absorption coefficient of selected material suitable as XRL mask absorber, as a function of wavelength [12]

the electrolytic growth of the absorber. The other strategy is based on a "subtractive" process by plasma assisted etching. In this case, the absorber structures, are obtained by subtracting material from a film. This is obtained after pattering a resist film on top of the absorber, that protects selectively areas that are required to be saved from the action of the plasma etching process (3.1.6). Gold is the most convenient material for the "additive" strategy. Absorption coefficient of suitable material as XRL absorber is shown in Figure 3.6. In the case of High Resolution XRL (HR XRL), then, the mask is made by a metallic base plated silicon nitride membrane supporting an absorbing pattern in gold, usually created by Electron Beam Lithography (EBL) on resist covered membranes, followed by electrochemical growth.

Silicon nitride membrane fabrication

Fabrication of silicon nitride membrane is a subtractive process (Figure 3.7) through which a silicon nitride double covered silicon wafer is etched until a single silicon nitride membrane is formed.
Silicon nitride film is deposited on both side polished silicon wafer using plasma-enhanced chemical vapor deposition (PECVD). Various silicon nitride film thickness are available commercially. In the case the membrane is intended to support metallic grown structure, a metal base plating is required; usually it is evaporated on one side of the wafer before the membrane production. The metalized side will become the membrane.
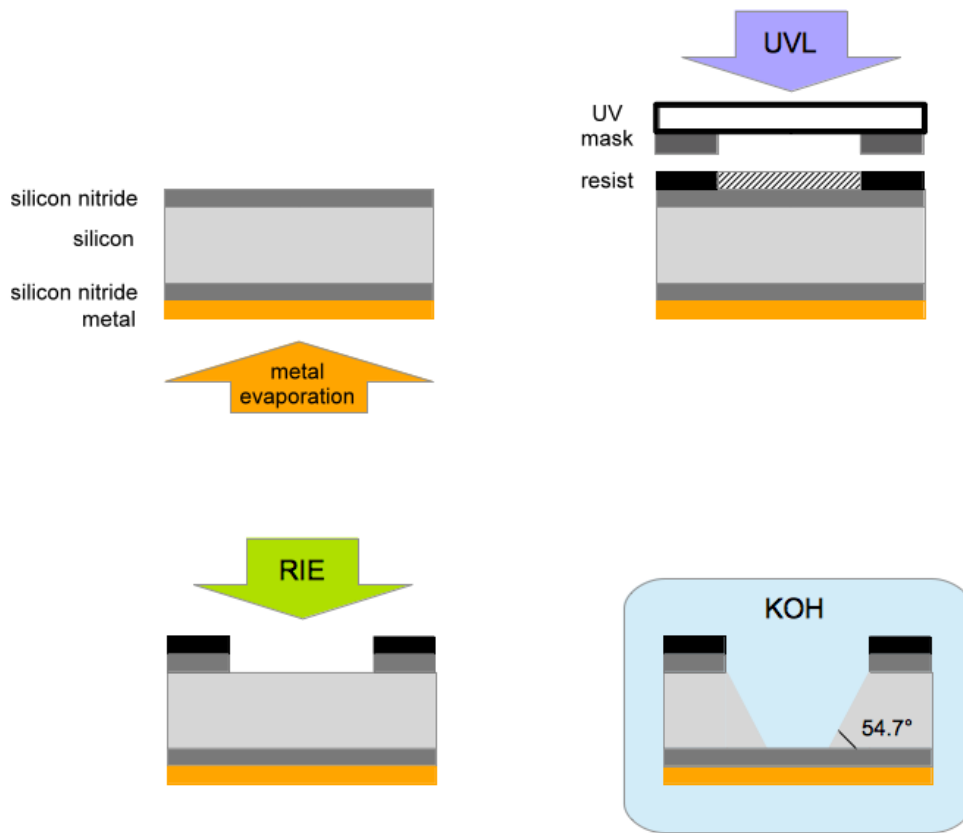
Figure 3.7: Membrane fabrication process

Membrane structure is transferred by UV lithography (see 3.1.5) on the clean side of the wafer, using the resist as a mask for removing selectively the silicon nitride film by reactive ion etching. In this way, a silicon nitride mask is created for the subsequent step of the fabrication process, the silicon wet etching in potassium hydroxide (KOH) solution. KOH attacks silicon preferentially in the <100> plane, producing an anisotropic V-shaped etch, whose sidewalls form a 54.7° angle with the surface. This feature has to be considered during the design of the UV lithography mask in order to obtain the desired membrane size.
It is also possible to produce the membrane after mask pattern fabrication.

3.1.4 Electron Beam Lithography

In electron beam lithography (EBL) high-energy electrons are focused into a narrow beam and used to expose electron-sensitive resist. The lithographed pattern is designed using a computer software, usually a CAD, and stored in

a digital format. The high resolution, the main advantage of this technique, is due partially to the short electron wavelength. Not limited by diffraction, the nanometer regime is achievable. Another advantage of the technique is the the flexibility, due to the easily modified pattern source.

Once produced, the temporary image layer created in the electron beam resist is used as a template or a mask respectively for the metal deposition of the final structure or the permanent transfer of the pattern image to the substrate.

Applications for the EBL are the fabrication of mask, used for parallel lithographic techniques, and the direct writing. The throughput limitations are the low exposure speed, the need to work in vacuum conditions and the cost of the system. Limitation in resolution may arise as the low effective mass electrons are easily deflected from their intended position on the substrate surface by scattering from collisions with the resist and substrate materials and by charge built up on the substrate surface. Those effects expose the resist over a greater area than the beam spot size. Electrons partially exposing the resist far from their impact point cause line width variations in dense structures, due to proximity effects. It is possible to correct this effect using proximity correction algorithms, which however slow the lithographic process.

In Figure 3.8 we report the basic EBL system scheme. It consists of an electron source providing the electron beam and associated components to control beam size, shape, and current. A stage holds the substrate to be exposed and maintains it in a plane orthogonal to the incident beam axis. Stage position is measured with high resolution and accuracy. The movement of the beam is controlled by a deflection system, composed by electromagnetic lenses, analogous to the SEM ones (see Section 3.2.1). A detection system permits the location of features (reference marks, used to calibrate the beam and to align the patten) on the stage or substrate by detecting electrons emitted when the beam is scanned across the reference mark. A vacuum system provides the necessary vacuum level at different points in the system and provides for substrate exchange at atmospheric pressure. A system control computer integrates all of these functions, establishing beam parameters, executing calibrations and alignments, sequencing stage movement, controlling pattern data flow to the deflection system, and controlling substrate exchange.

The development process completes the transformation of the resist coating into the three-dimensional representation of the CAD pattern. Although the CAD pattern is specified only in the plane of the substrate, the resist sidewall profile (normal to the substrate) can significantly impact pattern transfer and dimensional control.
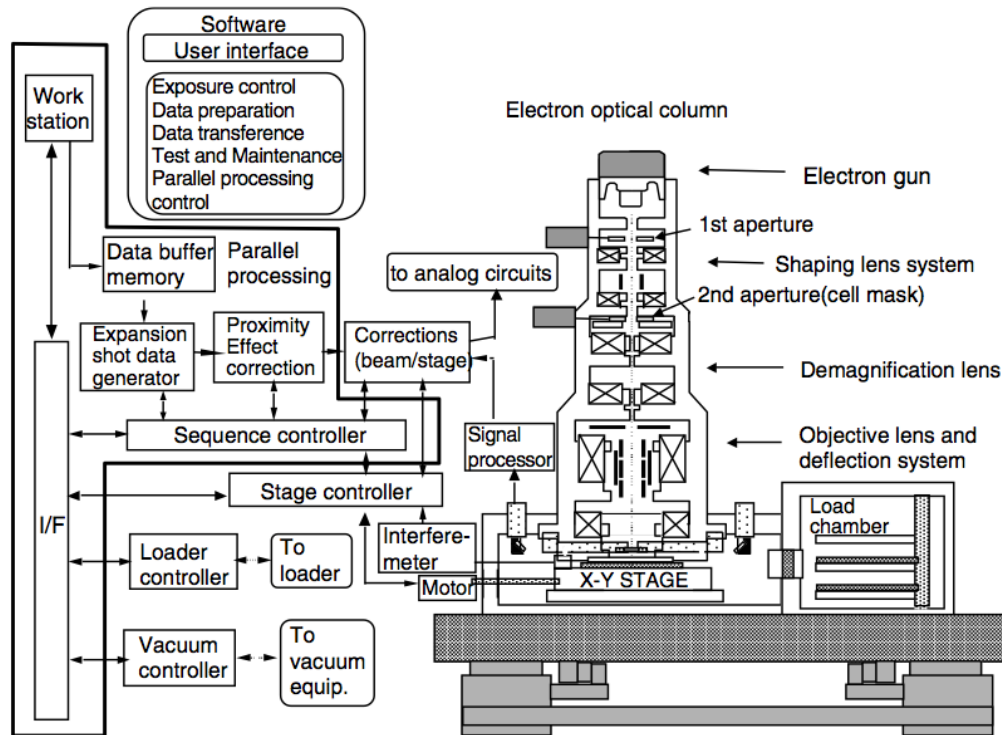
Figure 3.8: Typical electron-beam lithographic system scheme [13]

3.1.5   UV Lithography

Photolithography is one of the most common lithography techniques. As XRL, it is a parallel technique. It uses light (UV) to transfer a pattern from a photomask to a photoresist.

One of the advantages of UV lithography is the high throughput with resists of moderate to fast sensitivity. The primary limitations are resolution due to diffraction and substrate reflectivity. Diffraction affects resolution, since the image projected on the resist becomes increasingly blurred as the dimensions decrease, while substrate reflectivity affects line-width control, because of the standing waves in the resist and the effect of interference at the air-resist interface on coupling of the incident exposure dose into the resist.

The photomask is composed by flat glass or quartz substrate, transparent respectively to near and deep ultraviolet, and an absorber pattern metal layer, usually chromium, opaque to UV. The mask is placed in direct contact with the resist covered substrate and light, passing through the photomask, exposes the area of the resist not protected by the mask absorber pattern. In this way, a 1:1 image of the mask is transferred from the mask to the

photoresist.
Optical lithography is generally the most cost effective lithography technique.

3.1.6   Reactive Ion Etching

In plasma etching a solid surface is etched in the gas or vapor phase.
Plasma etching can be purely physical, when ions are used to bombard the surface, chemical, when reactive species are used, or a combination of the two.
A plasma is a partially ionized gas. A plasma reactor consists of a chamber containing two parallel plates (cathode and anode) in a vacuum system, connected to a DC or RF supply. When a gas is introduced in the chamber at a reduced pressure (10^{-1}-$10^{-3}mbar$) and a voltage is applied, a plasma may form. In DC case, when the applied voltage is high enough, the field in the reactor will exceed the breakdown field of the gas and a high voltage arc will flash between the electrodes, creating a large number of ions and free electron. When the ions strike on the cathode they release a cloud of secondary electrons, which are accelerated towards the anode. In the case the secondary electrons collide inelastically with neutral gas atoms, they creates more ions. Ion creation sustains the plasma. In the case one of the electrode is insulating, a AC signal can drive the plasma, to avoid the possibility of a charge accumulation on the surface to be etched due to insulation.
A plasma etch process requires six steps to occur:

1. a feed gas is introduced in the chamber and the plasma broke it down in chemically reactive species;

2. the species diffuse over the surface to be etched;

3. they are absorbed on the surface;

4. they react with the exposed surface;

5. the reaction product must be desorbed from the surface;

6. they are diffused away from the surface and transported by the gas stream out of the etch chamber.

In Reactive Ion Etching (RIE) reactive neutral chemical species generated in the plasma diffuse to the substrate where they form volatile products with the layer to be removed. The plasma supplies gaseous, reactive etchant species. Chlorine- and fluorine-based plasmas are commonly used in RIE. The penetration of the reactive species formed by plasma is dramatically increased

by ion bombardment due to voltage acceleration. As a result, the surfaces subject to ion bombardment etch much more rapidly than those that are not. In particular, the vertical sidewalls receive very little ion bombardment. RIE, indeed, was developed to achieve a strong anisotropic etch with a high selectivity.

3.1.7 Metal evaporation

Metal evaporation is a thin film deposition method. A metal evaporator consist of a vacuum chamber where the source material (a metal) is heated until it evaporates and the vapor particles condense on the sample.
The material to be deposited is loaded into a heated container, the crucible. It can be heated simply by an embedded resistance heater (thermal method) or by an electron beam (electron-beam method). Due to the very low pressure in chamber (10^{-5}-$10^{-7} mbar$), the atoms of the vapor travel across the chamber in a straight line until they impact on a surface where they accumulate as a film. Some evaporation systems may contain many crucibles in order to perform multiple material deposition without breaking vacuum. They may contain a large number of wafers suspended above the crucibles.
Deposition rate is commonly measured using a quartz crystal rate monitor. A feedback may be used to control the crucible heating in order to maintain a constant deposition rate.
The main disadvantage of metal evaporation, the discontinuity to cover surface topology, in particular the vertical walls, may be exploited for lift-off processes or tilted deposition.

3.1.8 Electrochemical growth

Electrochemical growth, also known as electroplating, is a method for metal deposition on conductive substrates [14]. It is typically used for finishing X-ray masks or other samples, especially when a thick layer of metal is needed.
The electrochemical growth exploits the well known process of discharge of metal ions in a solution when a voltage is applied.
The most basic scheme for DC electrolysis can be seen in Figure 3.9. Two electrondes are immersed in a solution, connected to the output of a DC current source. The metal is deposited onto the cathode and the anode complete the electrical circuit. The anode may be sacrificial, made on the same metal to be deposited and then dissolving releasing metal ions in the solution, or permanent, usually made of platinum coated titanium. In the latter case, metal ion depletion from solution is made good by adding metal to solution
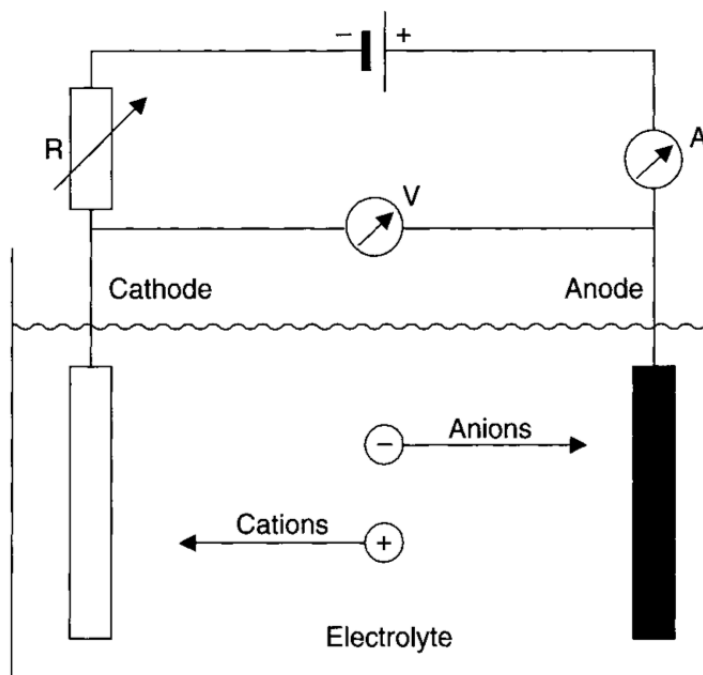
Figure 3.9: Main components of DC electrolysis system [14]

in the form of a metal salt. In IOM-CNR electrodeposition facility the anode
is the permanent type, thus the metal ions derive from metal salts added to
solution.

If a voltage is applied across the two electrodes in an electrolysis cell, a cur-
rent consisting of electron flow is set up. Electrons move from the anode
through the external circuit and back to the cathode. The cations in the
solution move to the cathode and the anions will move in the opposite direc-
tion. Current, thus, flows through the solution by virtue of the movement of
these charged ions and this is known as ionic current, or electrolytic conduc-
tance.

The process of electrodeposition of metallic layers from aqueous solution is
a quite complex process, involving a number of intermediate stages (Figure
3.10):

1. transport of the hydrated metal ion from bulk solution to the cathode;

2. stripping the hydration sheath from the metal ion at the metal-solution
   interface;

3. charge transfer with formation of adsorbed atom at the cathode surface;
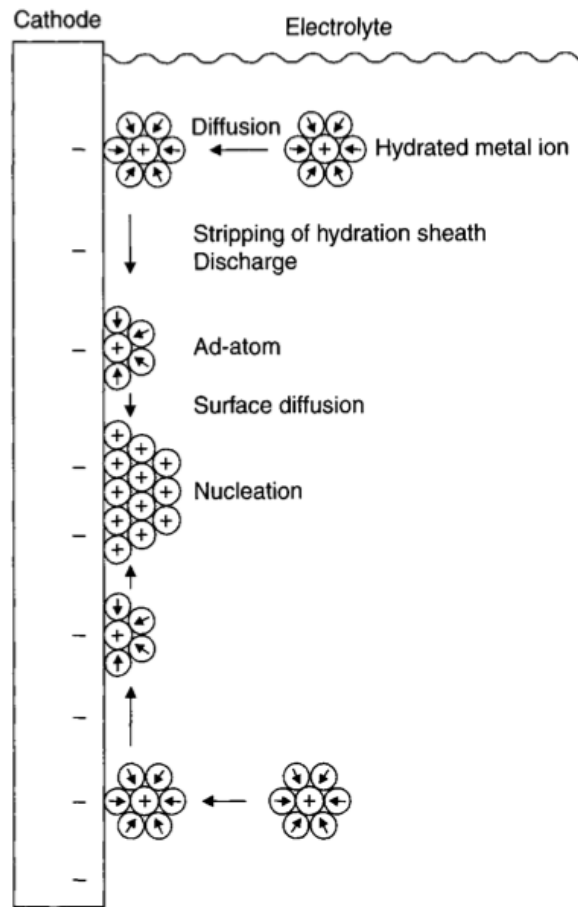
Figure 3.10: Main stages of the electrochemical deposition mechanism: migration of the hydrated metal ions to a cathode surface, surrender of the hydration sheath, formation of adsorbed atoms and formation of crystal nuclei at cathode surface [14]

4. formation of crystal nuclei by diffusion of the adsorbed atoms at the cathode surface;

5. fusion of thermodynamically stable crystal nuclei to form a metallic layer.

Convection and diffusion are the main mechanisms involved in the transport of metal ions from the bulk solution to the cathode surface. The discharge of adsorbed atoms takes place within the electrolyte double layer, which forms spontaneously at the metal-solution interface. In this phase the metal ions lose most of their charge. Nevertheless, a residual charge and a part of their hydration sheath remain. After passing through the electrolytic double-layer,

the ions are adsorbed on the cathode surface, forming the so-called *ad-atoms*. The last two stages of the electrochemical process are nucleation, resulting from the controlled migration of the ad-atoms on the surface (diffusion), and crystal growth, beginning once the nuclei have reached a critical size.

3.2   Characterization techniques

3.2.1   Scanning Electron Microscopy

The Scanning Electron Microscope (SEM) is the most widely used of all electron beam instruments. The main advantages of this microscopy technique are the versatility of its various modes of imaging, the excellent spatial resolution of its images, the ease with which the micrographs that are generated can be interpreted, the modest demands that are made on specimen preparation, and its "user-friendliness". Its resolution can approach 0.5 nm and it can handle specimens as large as production size silicon wafers.
In Figure 3.11 it is shown a schematic drawing of the SEM electron column. Inside the columns are [15]:

- the electron gun, the source of the electron beam which is accelerated down the column;

- a series of lenses, condenser and objective, which act to control the diameter of the beam as well as to focus the beam on the specimen;

- a series of apertures, which are micron-scale holes in metal film, through which the beam passes and which affect properties of that beam;

- controls for specimen position (x, y, z-height) and orientation (tilt, rotation);

- an area of beam/specimen interaction that generates several types of signals that can be detected and processed to produce an image or spectra.

The electron column is maintained at high vacuum levels, higher in the upper column than in the specimen chamber.
After being produced, accelerated and shaped, the objective lenses focus the electron beam on the specimen surface. To obtain the image of the specimen, the beam is rasted from left to right and top to bottom by the deflector coils. A signal is generated from the specimen, acquired by the detector, and processed to produce an image or a spectrum on the monitor display.
The electron gun provides a stable beam of electrons of adjustable energy. There are three main types of electron guns: Tungsten hairpin, Lanthanum hexaboride (LaB$_6$) and Field emission. The SEM we used in this thesis, a Zeiss Gemini at IOM-CNR in Trieste, is a Field Emission Gun (FEG). The FEG cathode consists of a sharp metal tip with a radius smaller than $100nm$. Below the tip two anodes extract and accelerate the electron beam. When a
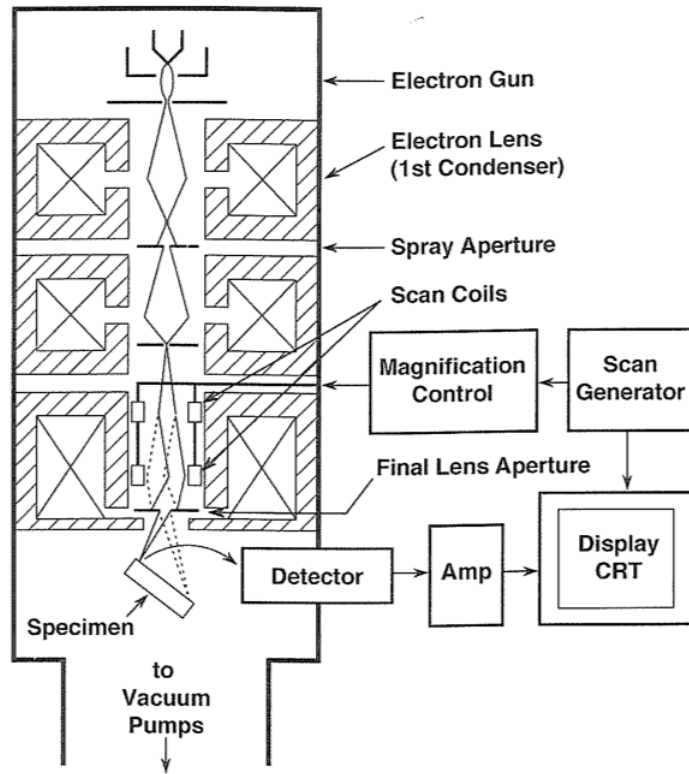
Figure 3.11: Schematic drawing of the electron column showing the electron gun, lenses, the deflection system and the electron detector [15]

potential difference, called extraction voltage V_1, is established between the first anode and the tip, an electric field, concentrated at the tip, is formed, facilitating electron emission (emission current). The potential difference between the tip and the second grounded anode determines the accelerating voltage of the gun, V_0. The higher the accelerating voltage the faster the electrons travel down the column and the more penetrating power they have. The field emission requires the tip to remain free of contaminants and oxides: Ultra High Vacuum conditions (10^{-10} to 10^{-11} $Torr$) are required.

Electromagnetic lenses are used to demagnify the image of the beam source exiting the electron gun and to focus the beam on the specimen. Condenser lenses are involved in demagnification. Objective lens focuses on the specimen as well as demagnifies. An electromagnetic lens consists of a coil of copper wires inside an iron pole piece. A current through the coils creates a magnetic field which is used to converge the electron beam. The electron of the beam passing through the magnet experiences a force parallel to the core of the lens, causing it spiraling, and a force parallel to the radius of the

lens, which compress (focus) the beam toward the vertical axes. The magnetic field is inhomogeneous: it is weak in the center of the gap and becomes stronger close to the bore. Electrons close to the center are less strongly deflected than those passing the lens far from the axis.

The object being imaged, then, is the source diameter, which is a Gaussian intensity distribution, of the electron beam as it exits the gun. The lenses action is to demagnify this beam source diameter. The SEM has stationary electromagnetic lenses which we can vary the strength of by altering the amount of current running through them. Being more than one electromagnetic lens, the image plane of the first lens becomes the object plane of the second. The total demagnification is the product of the demagnification of lens one with lens two.

Electromagnetic lenses are affected by:

- **Spherical aberration:** the inhomogeneous field in the lens results in a series of focal points of the beam, and the point source is imaged as a disk of finite size (disk of minimum confusion). Apertures reduces the effects of spherical aberration.

- **Chromatic aberration:** the electrons are generated by the gun at different energies, which, at the same location in the column, will experience different forces, being deflected by the lenses in a different way; a disk of minimum confusion is formed. Chromatic aberration is problematic especially at low accelerating voltages.

- **Astigmatism:** the field produced by the lenses is not perfectly symmetrical, resulting in an oblong beam.

The electron of the beam can interact with the coulomb field of both the specimen nucleus and electrons. These interactions are responsible for a multitude of signal types: backscattered electrons, secondary electrons, X-rays, Auger electrons, cathodoluminescence. Backscattered and secondary electrons are used to produce the image of the specimen.

When the electron interacts with the electric field of a specimen atom electron ad inelastic event occurs and the result is a transfer of energy to the specimen, eventually causing the expulsion of an electron from that atom: a *secondary electron* (SE). SE energy is less than $50\ eV$. The inelastic interaction is also responsible of the production of Auger electrons and X-rays.

When the interaction occurs between the electron and the electric field of the nucleus of a specimen atom, resulting in a change in direction of the beam electron without a significant change in the energy of the electron, we have an elastic event. In the case the elastically scattered electron is deflected back
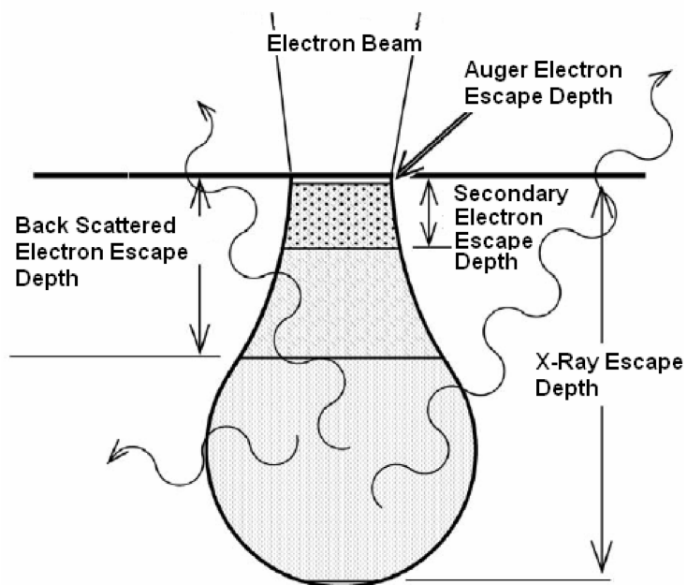
Figure 3.12: Interaction volume of the beam electrons.

out of the specimen, the electron is termed *backscattered electron* (BSE). Its energy ranges from 50 eV to nearly the incident beam energy.

The combined effect of the elastic and inelastic interactions is to distribute the beam electrons over a three-dimensional *interaction volume* (Figure 3.12). Secondary and backscattered electrons have different maximum escape depths given their energy differences. The escape depth of SE is approximately 5-50 nm; BSE can escape from a depth a hundred times greater, and X-rays even grater. The actual dimension and shape of the interaction volume depend upon accelerating voltage, atomic number and tilt of the specimen.

The loss of electron beam energy in the specimen occurs mostly in the form of heat generation at the irradiated point. Polymer materials and biological specimens, which are generally not resistant to heat, are easily damaged by the electron beam.

3.2.2   Ellipsometry

Ellipsometry is a non destructive, flexible and sensitive technique for the characterization of optical properties of the analyzed sample. From the analysis of the reflection, or the transmission, of a circularly polarized monochromatic wave incident on a multilayer flat sample, it is possible to obtain information about thickness and refractive index of each layer.

Let us consider the most general polarization of a monochromatic light: the

elliptic polarization, in which the endpoint of the electric-field vector processes along an elliptic trajectory in any plane perpendicular to the direction of propagation. The time evolution can be viewed as a superimposition of two harmonic vibration along the perpendicular axes, with a phase shift Δ. The amplitude of the electric field in the xy-plane, assuming the wave propagating along the z-axis, can be described as:

$$\mathbf{E}(t) = \left(\begin{array}{c} E_x(t) \\ E_y(t) \end{array} \right) = Re \left\{ \left(\begin{array}{c} Xe^{i\Delta} \\ Y \end{array} \right) e^{i\omega(t-t_0)} \right\}$$

The state of elliptic polarization is determined by the amplitude X and Y, besides the phase shift Δ. In ellipsometric measurement, only relative amplitude X/Y is relevant, because multiplying both X and Y by a common constant simply changes light intensity. When we define the angle ψ as $\psi = X/Y$, varying from 0 to $\pi/2$, we can represent elliptic polarization using the *Jones vector*:

$$\left(\begin{array}{c} \sin\psi e^{i\Delta} \\ \cos\psi \end{array} \right)$$

Simple cases of general elliptic polarization are:

- linear polarization, for $\Delta = 0$ or π

- circular polarization, for $\psi = \pi/4$ and $\Delta = \pi/2$ (right) of $\Delta = -\pi/2$ (left)

Ellipsometric technique is based on manipulation of the polarization state by auxiliary polarizing elements and measured sample. The basic configuration (PCSA, Figure 3.13) of an ellipsometer consists of [16]:

- a light source

- a linear polarizer (P)

- a retarder, called compensator (C)

- the sample (S)

- a linear polarizer, called analyzer (A)

- a detector

The wave incident on the sample is a superimposition of the parallel and perpendicular component of the wave to the plane of incidence (p and s polarization). The first polarizer (P) is used to produce pure linearly polarized light with a known direction of polarization. The compensator (C) is capable
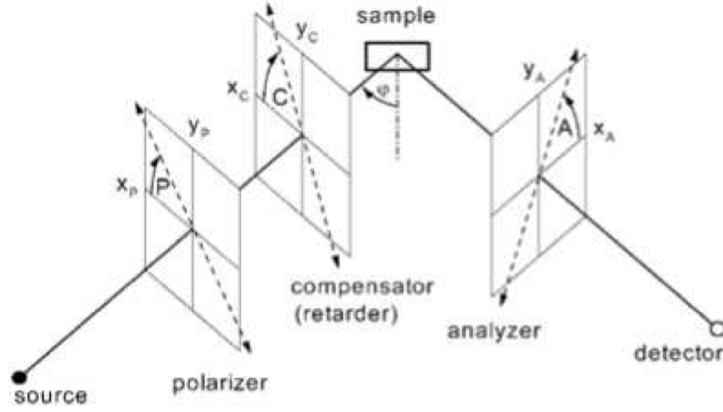
Figure 3.13: PCSA configuration, [16]

of introducing controlled amounts of phase delay between different components of polarization. The analyzer (A) determines the polarization direction of the reflected wave.

The ellipsometer measures the ratio of the reflectivity for the s- versus the p-polarized wave, $\tan\psi$, and the difference in the phase angle of the two reflected polarization, Δ. Those two quantities fully characterize the reflection of the two polarization.

It is assumed to have a planar sample with the angle of incidence denoted by ϕ. The beams incident on and reflected from the sample lie in the plane of incidence, which contains also the normal to the sample surface. Angles P and A defines respectively the direction of linearly polarized light transmitted by the polarizer and analyzer. The azimuth of the fast axis of the compensator is C.

Let us consider E_p as the complex amplitude of the linearly polarized wave transmitted by the polarizer. The wave incident on the compensator is a superposition of the component aligned along the fast[1] axis, having the complex amplitude $E_p\cos(P-C)$. The orthogonal component along the slow axes is $E_p\sin(P-C)$. The transmitted wave is modified by multiplying the two components by the complex transmittance t_f and t_s respectively, so the field amplitudes transmitted by the compensator along its fast and slow axes are:

$$E_f = t_f E_p \cos(P-C) \qquad E_s = t_s E_p \sin(P-C) \tag{3.5}$$

---

[1]fast and slow axes refer to directions parallel and perpendicular to anisotropy axis in a birefringence medium

The reflected wave, as the transmitted wave, is modified by multiplying the two components by the complex reflectivities r_p and r_s. The amplitudes of p- and s-polarized components reflected by the samples are:

$$E_{rp} = r_p(E_f \cos C - E_s \sin C)$$
$$E_{rs} = r_s(E_f \cos C + E_s \sin C) \tag{3.6}$$

and the wave transmitted by the analyzer results from the addiction of the incident p- and s-polarized components projected onto the direction of the azimuth A:

$$E_A = E_{rp} \cos A + E_{rs} \sin A \tag{3.7}$$

We can simplify our analysis considering a simpler elipsometric scheme, where the compensator has been removed. This configuration is called polarizer-sample-analyzer (PSA).
The field amplitude on the detector results:

$$
\begin{aligned}
E_A &= E_p(r_p \cos P \cos A + r_s \sin P \sin A) \\
&= E_p r_s(\rho \cos P \cos A + \sin P \sin A)
\end{aligned}
\tag{3.8}
$$

where ρ is the complex reflectance ratio defined as:

$$\rho = \frac{r_p}{r_s} = \tan \psi e^{i\Delta} \tag{3.9}$$

Photometric ellipsometry is based on measurements of intensity for a number of suitably chosen settings of the optical components influencing the polarization state of light. Light intensities, in PSA configuration, are measured for several properly chosen azimuths of the polarizer and analyzer. The analyzed state of polarization is independent of absolute intensities. Thus, one of them can be used as a reference for the measurement of relative values. To determine the two real ellipsometric parameters, at least three independent intensities are required.
When the azimuth P is fixed, the intensity transmitted by the analyzer is:

$$
\begin{aligned}
I(A) = I(P)|r_s|^2 \cos^2 P(\quad &\tan^2 \psi \cos^2 A + \tan^2 P \sin^2 A + \\
&+2 \tan \psi \cos \Delta \tan P \cos A \sin A)
\end{aligned}
\tag{3.10}
$$

It is possible to obtain the ellipsometric angle ψ from the relative intensity measured for $A = 0$, when the intensity for $A = \pi/2$ is taken as a reference:

$$\tan \psi = |\tan P| \sqrt{\frac{I(0)}{I(\pi/2)}} \tag{3.11}$$

The third intensity can be measured for $A = \pi/4$ and provides the value of the ellipsometric angle Δ:

$$\cos \Delta = sgn(P)\frac{2I(\pi/4) - I(0) - I(\pi/2)}{2\sqrt{I(=)I(\pi/2)}} \tag{3.12}$$

The PSA scheme with fixed polarizer is usually operated with a large number of intensity measurements at different analyzer azimuths. In this rotating analyzer configuration, the signal at the analyzer as a function of time (uniform rotation) is:

$$V(t) = DC + \alpha \cos(2\omega t) + \beta \sin(2\omega t) \tag{3.13}$$

(one AC component on a DC background). We can obtain the normalized intensity from (3.10):

$$\frac{I(A)}{2(tan^2\psi + \tan^2 P)} = I(P)|r_s|^2 \cos^2 P(1 + \alpha \cos 2A + \beta \sin 2A) \tag{3.14}$$

where

$$\alpha = \frac{tan^2\psi - \tan^2 P}{\tan^2 \psi + \tan^2 P} \tag{3.15}$$

$$\beta = \frac{2 \tan P \tan \psi \cos \Delta}{\tan^2 \psi + \tan^2 P} \tag{3.16}$$

α and β results from the discrete Fourier transform of the measured signal. Once computed, they are used to calculate the ellipsometric angles:

$$\tan \psi = |\tan P|\sqrt{\frac{1 + \alpha}{1 - \alpha}} \tag{3.17}$$

$$\cos \Delta = sgn(P)\frac{\beta}{\sqrt{1 - \alpha^2}} \tag{3.18}$$

Chapter 4

Nanofabrication

The core of this thesis is the fabrication of nanometric Split Ring Resonator using, as principal technique X-ray lithography (XRL), taking advantage of LILIT beamline at Elettra Synchrotron in Trieste (see Appendix A). The structures to produce, the Split Ring Resonator, have been presented in the previous chapters and the geometry design reported in Chapter 2. The fabrication of structures with features below $100nm$ is challenging for X-Ray Lithography: in order to achieve the desired resolution for the SRRs, a series of lithographic test have been performed.

In this Chapter we are describing the optimization of the fabrication of high density SRR array on transparent substrate. One of the final aim of this thesis is the fabrication of multiple chip sample on transparent substrate for multiple measurement on the same sample. The sample geometry, studied to achieve also microfluidic measurement, is shown in Figure 4.1.
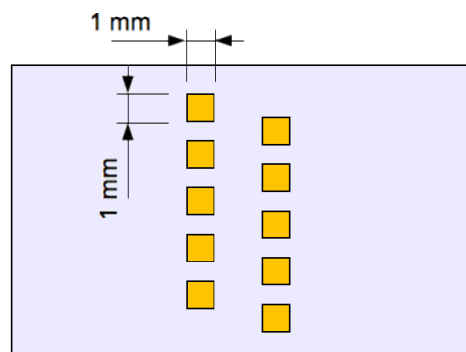

Figure 4.1: Sample design to perform multiple measurement and microfluidic experiment.

Membrane design, mask fabrication, X-ray lithography, sample preparation
and metal deposition are some of step composing the fabrication process we
have optimized.

We started using positive tone mask with a low density SRR array as a test
mask. In this phase we optimized resist development and electrochemical
growth. In order to study the mask replica and the sample fabrication, a
positive and a negative resist have been employed on three different sub-
strates.

The results obtained with the low density positive tone mask have been used
as a starting point for the optimization of the process using a high density,
positive tone mask. In this phase a negative and a positive resist have been
employed. The high density pattern induced a poor adhesion of the positive
resist: an adhesion promoter between the resist and the substrate has been
introduced, adding further step to the fabrication process. The combined
use of positive resist and adhesion promoter gave very positive result, while
the negative resist option has been abandoned because of the high sensitivity
and the inadequate results.

Due to the complexity of the process, the multiple chip design and the need
to use a positive resist, we studied the opportunity to design and fabricate
negative tone mask. The positive result obtained by the study drove us to
fabricate the negative tone mask for the multiple chip sample fabrication.

In the last part of the fabrication optimization a new mask concept has been
design and produced and the multiple chip sample has been fabricated on a
transparent substrate.

XRL has been performed at LILIT beamline on Elettra Synchrotron in high
resolution mode (i.e. soft X-ray regime) during $2GeV$ electron beam energy
user shift.

4.1 X-Ray lithography: positive tone masks

We started the fabricative process by considering positive tone mask. This means that to obtain the same positive tone on the sample two strategies can be followed:

- replica of the mask via XRL, using a positive resist, obtaining a negative tone mask to be used to produce the final sample, using a positive resist once more; or

- direct fabrication of the sample, using a negative resist.

The first option requires an additional lithographic step, but a positive resist generally offers better lithographic performances compared to the negative resist.

The first part of the lithographic optimization was focused on the following geometries:

Mask name	l (nm)	w (nm)	d (nm)	a (nm)
srr500	500	100	200	1000
srr360	360	90	90	460

where l is the lateral size of the SRR, w the width, d the gap dimension and a is the period (see Figure 1.12).

A mask was produced for each geometry. The mask *srr500* has been studied and fabricated in order to be used for XRL optimization: the large period of its structures makes it suitable for a first optimization of the XRL process, in particular regarding the choice of resist and the development. The goal of the mask *srr360* was testing the XRL process using a positive tone mask for the final geometry. The widening of the SRR features due to the steps in the fabrication process will produce the SRR geometry presented in Chapter2.

After pattern design, the X-ray mask has been fabricated writing the pattern by EBL on silicon nitride membrane, followed by electrochemical growth.

The pattern has been replicated by XRL on three different substrates: silicon, base-plated silicon and ITO on glass. Positive and negative resist has been employed.

4.1.1 Positive tone X-ray masks

Single silicon nitride membrane

The fabricated silicon membrane consist of a $4 \times 4mm$ square silicon nitride window held by a $1 \times 1cm$ silicon frame. It has been fabricated following

the sequence given in Section 3.1.3: it is a subtractive process during which a silicon nitride membrane is obtained from a silicon wafer covered by silicon nitride on both sides. To fabricate the membrane, the silicon nitride on the opposite side of the wafer and the silicon are removed, respectively, by dry and wet etching. The silicon nitride on the opposite side of the membrane is used as a mask for silicon wet etching, and this silicon nitride mask is fabricated by dry etching, using a resist mask.

The silicon nitride double covered silicon wafers were purchased from Minnesota University. In order to have a resistant and stable membrane, a wafer covered by $2\mu m$ thick silicon nitride layer was chosen.

In order to obtain an adequate contrast in soft X-Ray regime with $2\mu m$ silicon nitride membrane, the absorber on the mask has to be at least $380 - 400nm$ thick: the electrochemical growth is, then, the best choice for depositing the absorber pattern in gold. To perform electrochemical growth the substrate has to be conductive. A base plating consisting of $10nm$ of chromium (Cr) and $20nm$ of gold (Au) has been evaporated on one of the side silicon nitride wafer. Few atomic layer of Cr are used to promote the poor Au adhesion on silicon nitride. Cr is chosen instead of titanium (Ti), since the latter would be etched by the following KOH silicon etching. The total thickness of the bilayer ($30nm$) does not affect membrane transparence to X-rays.

The evaporation has been performed at IOM-CNR thermal metal evaporation facility. Wafer holder rotates during evaporation for best plating uniformity. The base plating operation precedes membrane fabrication process to limit defects on silicon nitride film. The opposite side of the wafer will be etched. After metallic bi-layer evaporation, both sides of the wafer has been covered by MEGAPOSIT SPR 220 3.0 positive resist, spun at $3500rpm$ for $45s$. Soft bake at $115°C$ for $90s$ followed resist deposition. Resist deposition on metalized side is requested to protect the metal layer.

UV lithography is used to obtain the resist mask needed for silicon nitride etching. The pattern on the employed UV mask is designed to obtain a final $4 \times 4mm$ membrane given the etching angle due to KOH silicon etching ($54.7°$. The mask/wafer assembly was exposed to UV at $3mW/cm^2$ for $18s$, baked at $115°C$ for $90s$, then developed in MICROPOSIT MF-24A developer for $30s$ and rinsed in water.

The silicon nitride has been etched at IOM-CNR RIE facility in O_2-CF_4. Parameter process are the following:

O_2 (sccm)	CF_4 (sccm)	P (W)	Bias (V)	p (mbar)	t (min)
1.5	28.5	150	250	3.5 e^{-1}	25

The silicon nitride is removed in the areas not covered by the resist, creating the hard silicon nitride mask.
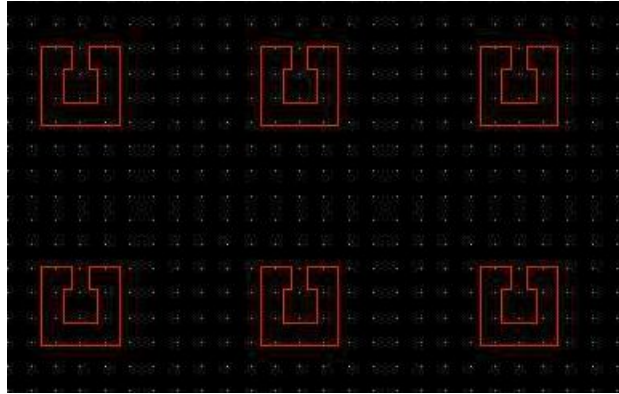
Figure 4.2: Example of SRR designed using LayoutEditor

The final step of membrane fabrication is silicon wet etching. After removing the remaining resist in hot ($50°C$) acetone, the wafer is immersed in $5M$ KOH solution at $65°C$ for 12 hours. Rinse in hot water and careful nitrogen flux drying complete the process.

Electron Beam Lithography and electrochemical growth

The absorber pattern of the X-ray mask has been lithographed using EBL and the resulting resist template has been filled by electrochemical growth of gold.

The fabricated base-plated membrane has been covered with Allresist AR-P 671.05, positive polymethylmethacrylate (PMMA), spun at $3000rpm$ for $60s$. The resist has been baked at $180°C$ for $30min$. PMMA layer thickness is approximately $580nm$.

The pattern has been designed using the software LayoutEditor (in Figure 4.2 we show an example of SRR design). EBL has been performed at Laboratory for Nanofabrication of Nanodevices (LaNN) in Padova. The EBL worked in high resolution (HR) mode using a $100keV$ acceleration voltage and a beam current of $100pA$. After exposition, the resist has been developed in high contrast developer solution of 3:7 H_2O/isopropyl alcohol (IPA) [57] for $20s$, then rinse in water.

The metal deposition has been performed at IOM-CNR electrodeposition facility.

The facility works in direct current with the following parameters:

I (mA)	T ($°C$)	t (s)
100	35	30

In Figure 4.3 and 4.4 we show the *srr500* mask after gold growing and resist removing in hot acetone, respectively in top and tilted view. The tilted view shows the height of the structure, more than $380nm$, which is sufficient for high resolution X-ray lithography (soft X-ray regime). The mask *srr500* has
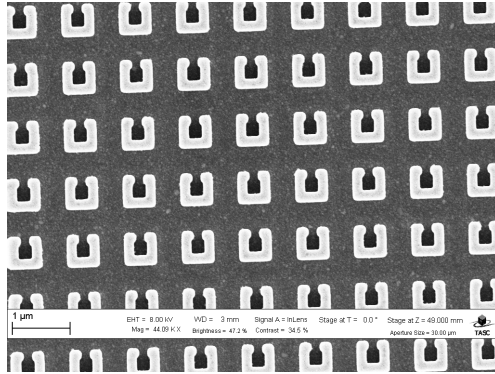

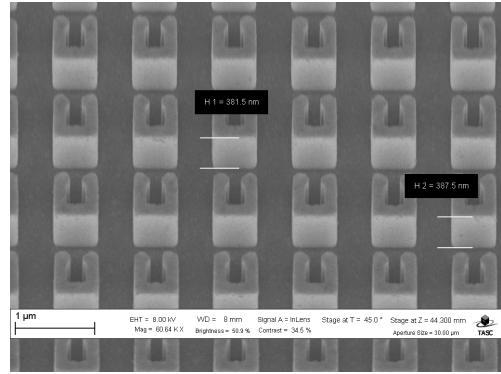Figure 4.3: XRL mask, *srr500*, top view

Figure 4.4: XRL mask, *srr500*, tilted view

been studied and fabricated in order to be used for XRL optimization: the total area of the SRR array is $500 \times 500\mu m$.

The mask *srr360* has been designed in order to test the final geometry fabrication. Its fabrication process is the same of the previous mask. We report in Figure 4.5 and 4.6 the top and the tilted image of *srr360*.
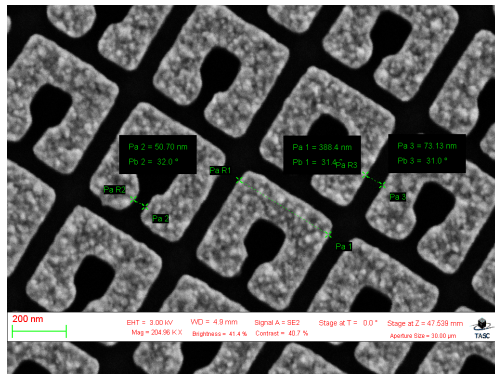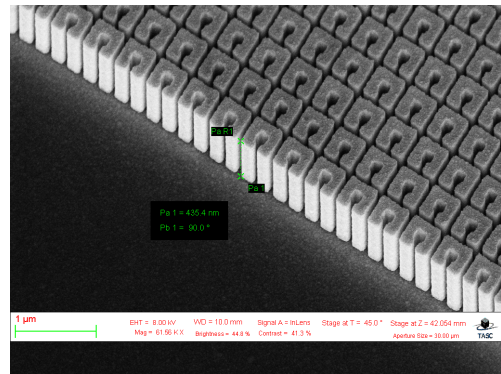

Figure 4.5: XRL mask, *srr360*, top view

Figure 4.6: XRL mask, *srr360*, tilted view

We would like to underline the filling factor of the mask *srr360* is larger than *srr500*, as can be observed from the comparison of Figure 4.3 and 4.5.

This difference has become important in the optimization of the process, in particular regarding the choice for the resist.
All the images have been taken using the Zeiss Gemini SEM at IOM-CNR.

4.1.2 X-ray lithography: mask *srr500*

The mask *srr500* was used to analyze the XRL process for both mask replica and sample fabrication. The positive resist PMMA and the negative resist SAL 601 have been employed for the tests. Three different substrate have been investigated:

- **silicon**: using PMMA for testing the development solutions;

- **base plated silicon**: using PMMA to study the mask replica process; using SAL to study the lithographic process;

- **ITO on glass**: using SAL to study the lithographic process on transparent substrate.

PMMA on silicon

In this process phase we compared two development solution:

- **MIBK:IPA in 1:3 solution**, the standard development for XRL processes involving PMMA, and

- **water:IPA in 3:7 solution**, a development solution for electron beam impressed PMMA proposed by Yasin in 2002 [57] H2O=IPA.

We performed the test on silicon as a cheap substrate requiring no preparation. The silicon has been covered by Allresist AR-P 671.05 PMMA, spun at $3000rpm$ for $60s$ and baked at $180°C$ for $30min$.
We prepared a dose matrix for each of the two set on PMMA covered samples. We report in Figure 4.7 and 4.8 two samples exposed at the same dose ($2J/cm^2$) but developed using, respectively, the MIBK:IPA solution for $60s$ (rinse: IPA) and the H_2O:IPA solution for $20s$ (rinse: H_2O). The images are taken in low magnification to highlight the effect of the development solution on the resist exposed through the silicon nitride membrane. The dark frame in the left and bottom part of Figure 4.7 is the unexposed PMMA under the mask frame; the SRR chip is in the centre of the image. In the remaining area of the image, which is the part of the sample exposed through the mask membrane, the stripes are residuals of PMMA. The stripes are due to inhomogeneity of the berillium window closing the beamline (see Appendix A for
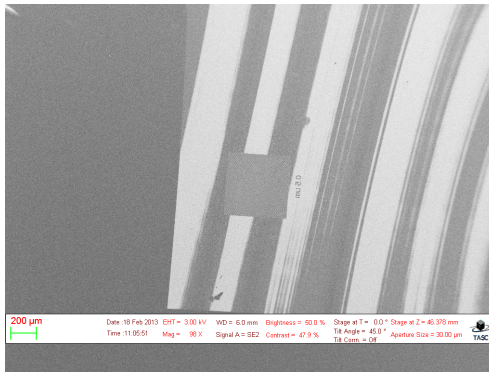
Figure 4.7: PMMA covered silicon, exposed to X-ray and developed using a MIBK:IPA=1:3 solution
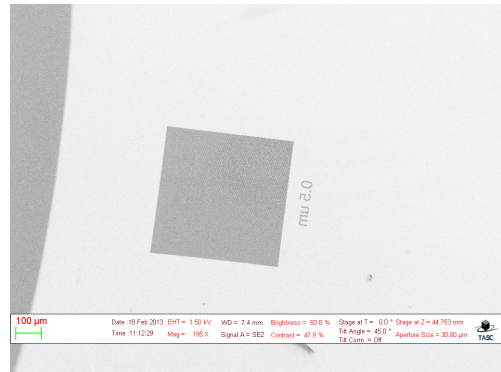

Figure 4.8: PMMA covered silicon, exposed to X-ray and developed using a H_2O:IPA=3:7 solution

beamline scheme). In Figure 4.8 the residual PMMA stripes are not present. The development process lasted $65s$ in MIBK:IPA case and $10s$ in H_2O:IPA case.
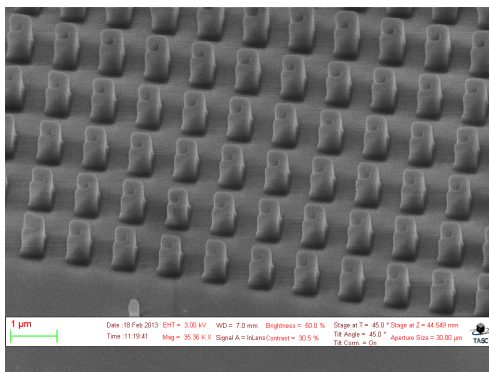
Figure 4.9: SRR in PMMA on silicon. MIBK:IPA=1:3 development
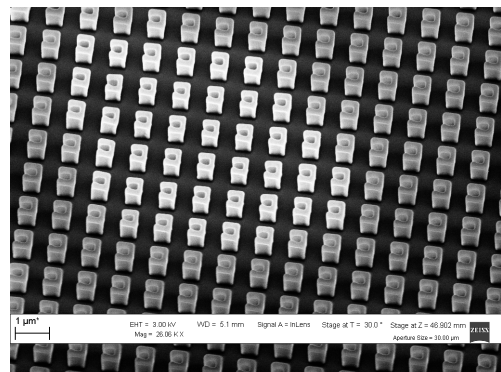
Figure 4.10: SRR in PMMA on silicon H_2O:IPA=3:7 development

Figure 4.9 show the PMMA SRR structures resulting from XRL and MIBK:IPA development. The edges of the structure are not sharp and a residual layer of PMMA still covers the substrate. The development in H_2O:IPA=3:7, whose result is shown in 4.10, produces sharper structures. The silicon substrate is clean from residual of PMMA.

We can conclude the H_2O:IPA development exhibit an higher selectivity, a higher constrast and an higher speed compared to the standard MIBK:IPA

development; this last feature can be exploited in order to use lower doses, reducing exposure time.

PMMA on base plated silicon

The XRL process on PMMA covered base plated silicon was the preliminary study for the mask replica via XRL.

The substrate for every test is silicon covered by a base plating of $10nm$ of chromium, as gold promotion layer, and $20nm$ of gold as seed layer for the subsequent electrochemical gold deposition. The evaporation of the base plating was performed at IOM-CNR thermal evaporation facility in rotating mode.

The substrate has been covered by Allresist AR-P 671.05 PMMA, spun at $3000rpm$ for $60s$ and baked at $180°C$ for $30min$.

The results of the previous test on silicon have been exploited as starting point for base plated silicon exposures. The dose in $2J/cm^2$ and the development solution used is H_2O:IPA=3:7.
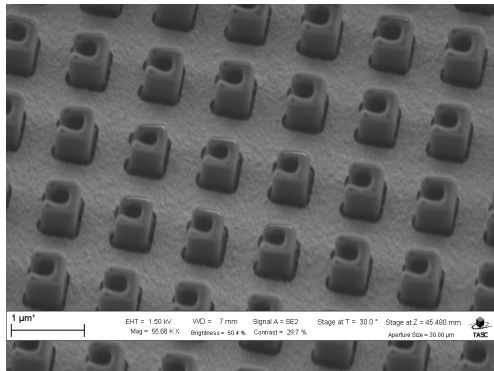
Figure 4.11: SRR in PMMA on base plated silicon. Few nanometers of gold has been grown
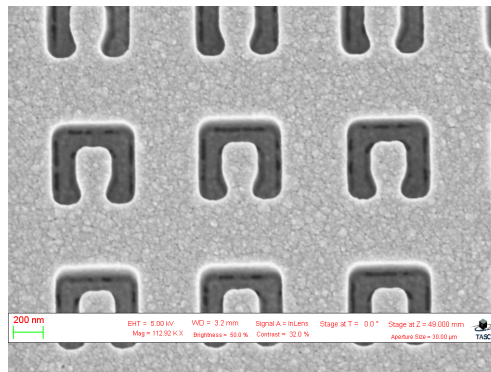
Figure 4.12: Sample after gold growth and PMMA removal in hot acetone

The SRR in PMMA resulting from the exposition and subsequent development are shown in Figure 4.11. A few nanometer layer has been grown in order to test the cleaning of the substrate from residual PMMA. Figure 4.12 show the SRR holes structure after electrochemical growth. The good quality of grown gold proves the good substrate cleaning.

Gold growings has been performed in IOM-CNR electrochemical deposition facility in direct current. Parameters of the process are: I= $100mA$,

T= $35°C$, t= $30s$. From the test of PMMA on base plated silicon we can conclude the mask replica process is possible for this geometry.

SAL on base plated silicon

In this phase we test the negative resist SAL601. As previously said, the use of a negative resist eliminate the mask replica step in the lithographic flowchart.

The substrate is base plated silicon ($10nm$ of chromium/$20nm$ of gold) covered by $530nm$ of MICROPOSIT SAL601, spun at $6000rpm$ for $60s$ and baked at $105°C$ for $60s$. The negative resist require an additional post exposure baking, before development, to promote resist cross-linking. The exposed samples have been baked at $105°C$ for $60s$. The used development solution is MICROPOSIT MF319 (rinse in water).

The dose matrix for the SAL experiment proved this negative resist being approximatively twenty times more sensible than the PMMA. As a consequence, small differences in the dose may cause considerable change in the lithographic results.

In Figure 4.13 it is shown the sample after exposure, post exposure baking and development. The exposure dose is $29mJ/cm^2$ and development time $15s$.
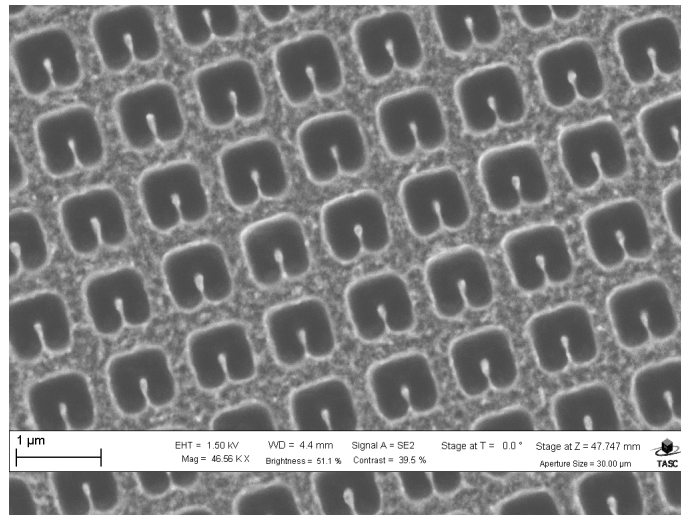

Figure 4.13: XRL on SAL. The sample has not been grown

It is evident from the SEM image the substrate on the open areas is still covered by SAL. That it is not an effect due to the over-exposure, but the

result of the very good adhesion of SAL on the substrate. To remove the residual few nanometers of SAL, an oxygen plasma etching is necessary. The parameters of the dry etching are the following:

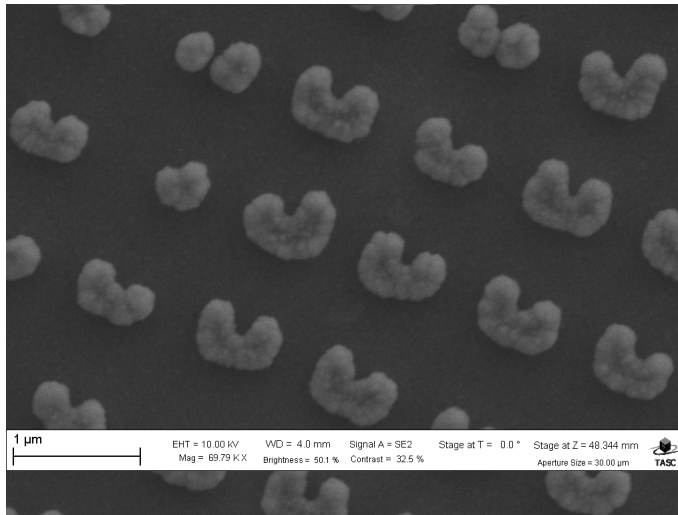| O_2 (*sccm*)	P (*W*)	Bias (*V*)	p (*mbar*)	t (*s*)
30	40	90	3.8 e^{-1}	30

Figure 4.14: Sample after gold growth with defects. The substrate of the open areas in the resist template has not being cleaned properly

The parameter presented for the oxygen plasma are the final result of the SAL removing optimization. When the SAL is not completely removed from the substrate in the open areas, the electrochemical growth is defective, as can be seen in Figure 4.14.

After the open areas bottom cleaning, the sample is ready for the growth, from which it is possible to achieve information about the quality of the lithography. The dose received from the sample shown in Figure 4.15 is $29mJ/cm^2$, while the dose received from the one shown in Figure 4.16 is $31mJ/cm^2$. The other parameters are the same for both the samples: post exposure bake at $105°C$ for $60s$, oxygen plasma, gold growth at $35°C$ for $20s$ with I= $100mA$. The difference in the SRR structure in the two exposures is due to the high sensitivity of the SAL601.

In Figure 4.17 and 4.18 we show the final result of the lithographic test and the consequent optimization of the process (baking, development, oxygen plasma, electrochemical growth). The SRR shape is sharper than the previous samples (see Figure 4.15), but the dimension of the pattern is much
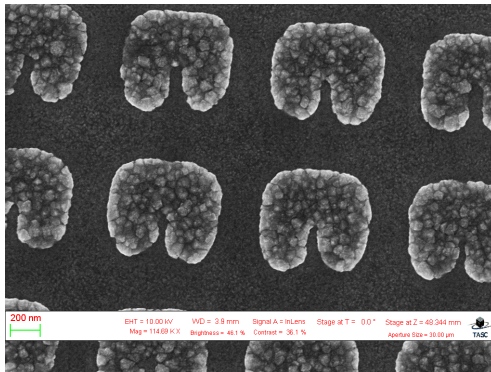
Figure 4.15: Sample after gold growth and SAL removal; dose= $29mJ/cm^2$
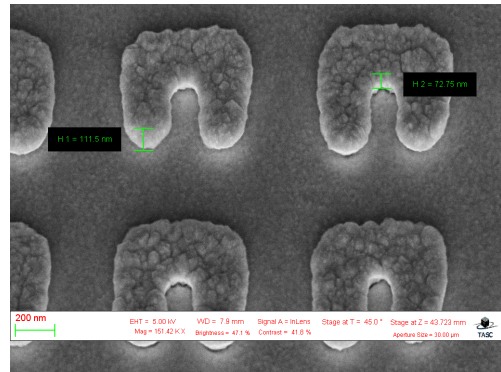
Figure 4.16: Sample after gold growth and SAL removal; dose= $31mJ/cm^2$
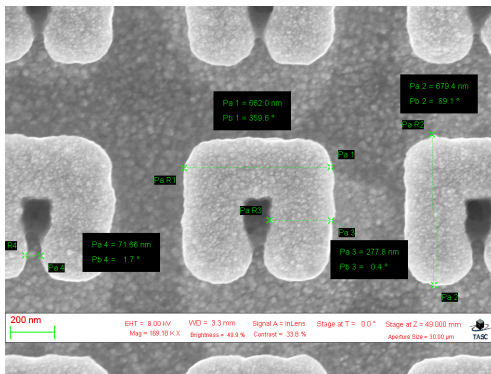
Figure 4.17: Final test for XRL on SAL covered base plated silicon. Top view
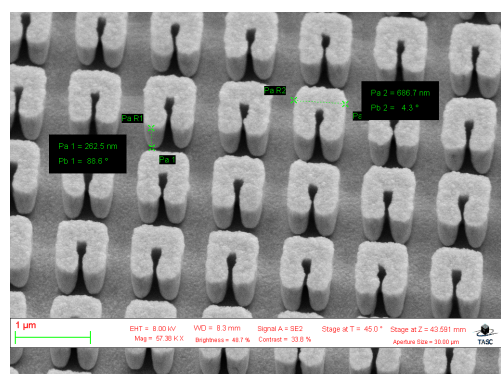
Figure 4.18: Final test for XRL on SAL covered base plated silicon. Tilted view

larger than the dimension of the pattern on the mask. The sample has been fabricated by XRL, receiving a dose of $44mJ/cm^2$, on SAL covered base plated silicon. The lithography has been baked at $105°C$ for $60s$, developed in MF319 for $20s$ and the residual SAL has been removed via oxygen plasma (parameters reported above). The growth has been performed at I= $100mA$, T= $35°C$ for $60s$.

SAL on ITO

The final phase of SAL test lithography has been performed of ITO, to explore the possibility to use the process to produce samples on transparent substrate.

We report here only the final result of the process, it being analyzed and described in the previous section.

In Figure 4.19 we report the result of the following process, derived from the previous test:

1. ITO cleaning: three step cleaning process: substrate immersion in water and soap, water, and IPA in ultrasonic bath;

2. SAL deposition: resist spin deposition at $6000rpm$ for $60s$ and baking at $105°C$ for $60s$;

3. XRL: exposition in soft X-ray regime, dose d= $40mJ/cm^2$;

4. post exposure bake: bake at $105°C$ for $60s$;

5. development: immersion in MF319, $20s$, rinse in water;

6. residual SAL removal: oxygen plasma, $30s$ (see the process details on the previous section);

7. electrochemical growth: direct current mode, I= $100mA$ at $35°C$ for $50s$

8. resist removal: hot acetone.

Comparing the result of the process on ITO to the SRR on base plated silicon presented in Figure 4.17 it is possible to notice the different quality of the gold grown. The difference is due to the morphology of the conductive seed layer: ITO presents a higher roughness compared to gold, which is replicated by the growth.

The dimension of the SRR are larger than the structure on the mask, resulting in a less sharp structure. The high sensitivity of the resist and the small features of the structure makes the replica of the mask challenging.

Conclusion

The mask *srr500* was used to test the XRL process on LILIT beamline. In particular, the possibility to achieve line width around $100nm$ was analyzed. The study of the lithographic process was fundamental to set the
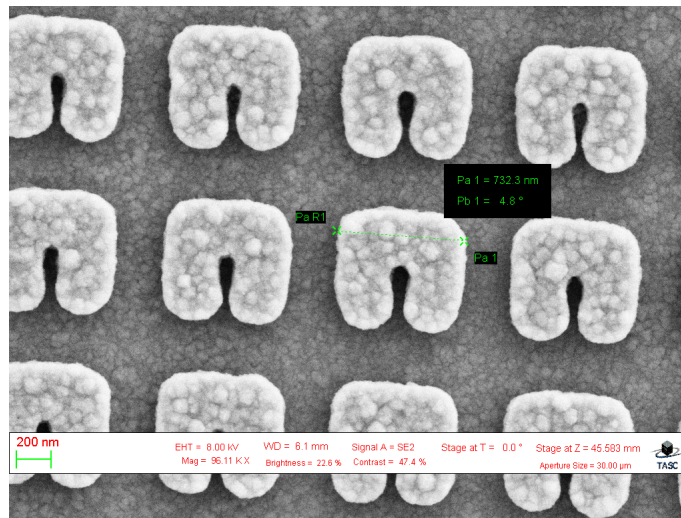
Figure 4.19: Sample on ITO. XRL on SAL and electrochemical gold of growth. The resist template has been removed.

development process, in particular the choice of the development solution.
The fabrication of the SRR structure using a negative resist is possible, though the result are less precise than the positive resist result.
Resist removal by plasma etching and electrochemical growth on different substrates have been examined in this phase.

4.1.3   X-ray lithography: mask *srr360*

In this part of the project we use the mask *srr360* to test the XRL of the final geometry. As the mask *srr500*, the mask *srr360* has been used with negative and positive resist, and on different substrates. The positive resist PMMA and the negative resist SAL 601 have been employed for the tests and, due to the poor adhesion of PMMA on gold in addition to the problems deriving from the high filling factor of the structure, the combination of SAL (as adhesion layer) and PMMA has been analyzed.
Three different substrate have been investigated:

- **silicon**: using PMMA as a first test of the lithography on positive resist;

- **base plated silicon**: using PMMA as a preliminary study of the mask replica process; using SAL to study the lithographic process;

- **base plated silicon nitride membrane**: using PMMA on a adhesion layer of SAL to analyze the mask replica process.

SAL on base plated silicon

The first test performed with the mask *srr360* was the lithography on SAL601 covered base plated silicon. The substrate was chosen in order to check the cleaning of the bottom of lithography taking advantage of the electrochemical growth.

The phases of the process, already fine tuned using the lower resolution mask *srr500*, are summarized in the following list:

1. SAL deposition: resist spin deposition at $6000rpm$ for $60s$ and baking at $105°C$ for $60s$;

2. XRL: exposition in soft X-ray regime, exposition time from d=$25mJ/cm^2$ to d= $44mJ/cm^2$;

3. post exposure bake: bake at $105°C$ for $60s$;

4. development: immersion in MF319, $20s$, rinse in water;

5. residual SAL removal: oxygen plasma, $60s$ at $40W$;

6. electrochemical growth: direct current mode, I= $100mA$ at $35°C$ for $20s$
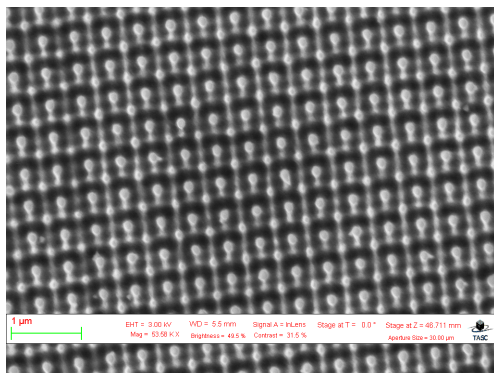
7. resist removal: hot acetone.

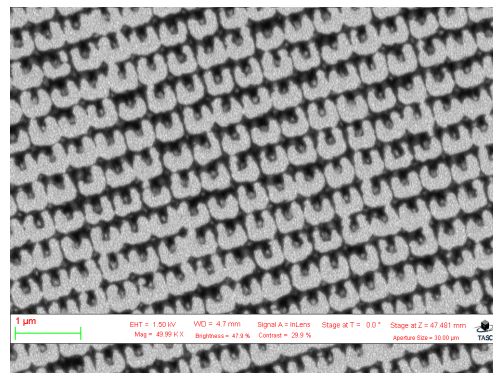Figure 4.20: XRL on SAL, mask *srr360*. Dose d= $44mJ/cm^2$

Figure 4.21: XRL on SAL, mask *srr360*. Dose d= $25mJ/cm^2$

The duration of the plasma SAL removing was fixed at the maximum value of $60s$, after which the etching affect heavily the walls of the resist template, considerably modifying the pattern. The only parameter we modify was the exposure time.

The result of the higher and lower dose are respectively presented in Figure 4.20 and 4.21. Both the samples have been processed till the growth step. The SAL has not being removed in hot acetone, to analyze the process result including the lithographic step. The higher dose sample, d= $44mJ/cm^2$, present no growing: this is due to the excessive lithographic dose, which caused an excessive cross-linking of the resist, in particular at the bottom of the open areas of the resist template, as can be seen in the picture. The SAL layer thickness in that region was too high to be removed by the plasma etching process. The SAL residual layer was, on the other hand, removed in the lower dose sample, d= $25mJ/cm^2$, allowing the gold to grow. The SRR obtained with the lower dose process have an irregular shape, due to the fact the SAL removal is not homogeneous over the SRR array.

The high sensitivity of the SAL, the small features of the mask, its high filling factor and low contrast, the difficulties arising in the control of the low doses on LILIT beamline, makes this resist unsuitable for the fabrication of nanometric split ring resonators via X-Ray Lithography.

PMMA on silicon

In this phase of the process optimization, we used PMMA covered silicon. The standard process of substrate preparation, already presented in the previous section, is PMMA deposition on silicon by spinning. The resist is Allresist AR-P 671.05 PMMA. It has been spun at $3000rpm$ for $60s$ and baked at $180°C$ for $30min$. After the exposition (dose d= $1,274J/cm^2$), the sample has been developed in H$_2$O:IPA=3:7 solution for $20s$ and rinsed in water.

The lithographic result is presented in Figure 4.22. The quality of the lithography is good, the mask contrast in sufficient to impress the PMMA and the shape of the SRR is comparable to the mask (see Figure 4.5).

PMMA on base plated silicon

The XRL on PMMA and silicon has been the starting point of the lithographic test on PMMA over base plated silicon.

The base plated substrate, prepared at IOM-CNR depositing the bi-layer Cr/Au $10nm/20nm$, has been covered by Allresist AR-P 671.05, spun at $3000rpm$ for $60s$ and baked at $180°C$ for $30min$. After exposition (dose
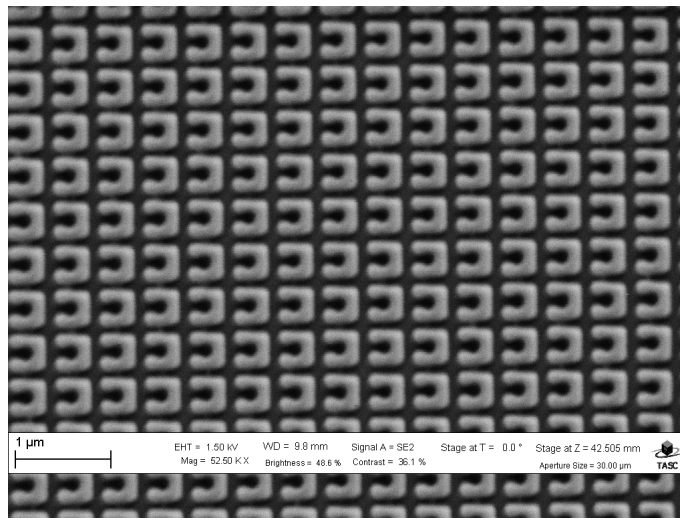
Figure 4.22: XRL on PMMA and silicon

d= $1,820 J/cm^2$), the sample has been developed for $20s$ in H_2O:IPA=3:7 solution.

The SEM image of the sample after development show the structures detached from the substrate (Figure 4.23). A resist detachment can be ascribed

Figure 4.23: XRL on PMMA and base plated silicon. The dose is too low, but the structures are detached from the substrate

to excessive dose or poor resist adhesion to the substrate. From the image it

is possible to notice the dose given to the sample was not sufficient to impress the PMMA and produce the SRR. The resist detachment is to be ascribed, then, to the poor adhesion of the PMMA to the gold. Another evidence of this hypothesis is the absence of the effect on silicon, as can be seen comparing 4.23 with Figure 4.22. The hig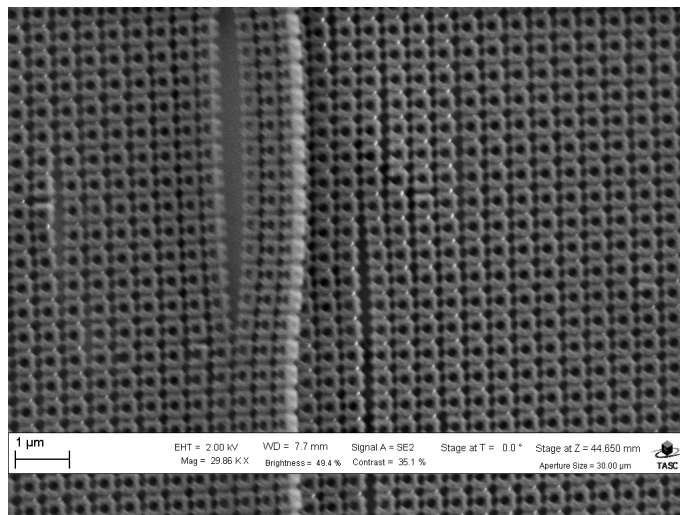h filling factor, the low contrast and the resolution of the mask pattern also contribute to the detachment, which was not present in the lithographic test performed with the mask *srr500*.
The PMMA adhesion on gold has to be promoted using an adhesion layer.

PMMA and SAL on base plating

In this final phase of the optimization of XRL on PMMA for mask replica we developed the lithographic process on positive resist using an adhesion layer for PMMA. Diluted SAL has been chosen as the adhesion promoter for PMMA layer on base plated silicon. After PMMA deposition, the sample is treated as a PMMA covered sample for the exposure and development process; the adhesion layer of diluted SAL is not removed by PMMA development. A dry etching process is necessary to remove the SAL: optimization of the residual SAL plasma etching process has been performed in this phase. After the removal, the sample is ready for growth.
We diluted MICROPOSIT SAL607 in Sigma Aldrich Ethyl L-lactate in 1:8 proportion. A thin layer ($< 20nm$) of SAL/Ethyl L-lactate 1:8 has been deposited on the base plated silicon by spinning at $6000rpm$ for $60s$. In order to remove the solvent which may interfere with the following PMMA deposition, the SAL covered sample has been baked at $105°C$ for $60s$. Allresist AR-P 671.05 spin deposition at $3000rpm$ for $60s$ followed. The bi-layer covered base plated silicon has been baked at $180°C$ for $30min$.
The correct dose for the lithography, d= $1.730J/cm^2$, has been obtained with a dose matrix. A set of samples has been prepared to optimize the adhesion layer removal. The two recipes we compared for reactive ion etching are the following

O_2 ($sccm$)	CF_4 ($sccm$)	P (W)	Bias (V)	p ($mbar$)	t (s)
30	0	40	100	3.5 e^{-1}	40
28.5	1.5	40	100	3.5 e^{-1}	40

The comparison between the two recipes is reported in Figure 4.24, 4.25, 4.26 and 4.27.
Figure 4.24 show the sample after lithography, plasma etching in O_2/CF_4 gas mixture and $30s$ gold growth at I= $100mA$ at $35°C$. In Figure 4.25 an equivalent sample (same dose, same development process, same growth) having received a plasma etching in pure O_2 is shown. The resist profile is
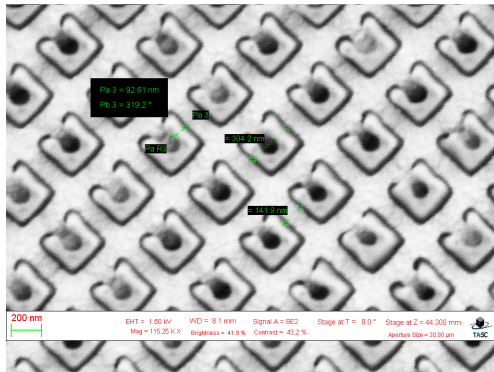
Figure 4.24: Sample in base plated silicon, after XRL, O_2/CF_4 plasma etching and electrochemical growth. The resist has not being removed.
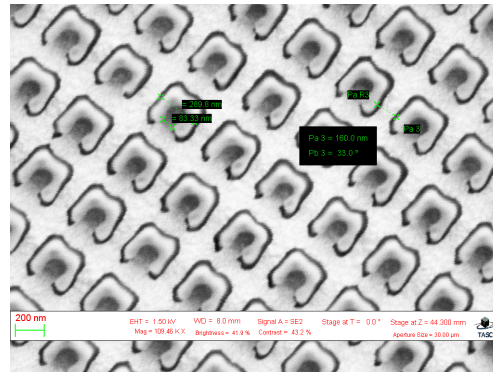

Figure 4.25: Sample in base plated silicon, after XRL, O_2 plasma etching and electrochemical growth. The resist has not being removed.

Figure 4.26: Sample in base plated silicon, after XRL, O_2/CF_4 plasma etching and electrochemical growth. Resist removed.
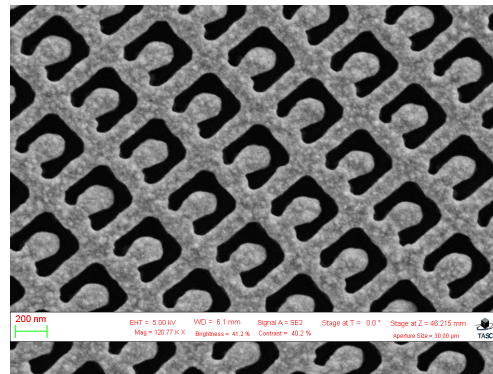
Figure 4.27: Sample in base plated silicon, after XRL, O_2/CF_4 plasma etching and electrochemical growth. Resist removed.

sharper and more corresponding to the mask (Figure 4.5) in the first sample than in the second.

The same samples are shown after resist removal. The holes profile on the sample etched using the O_2/CF_4 gas mixture (Figure 4.26) is actually more defined, but the sample present not cleaned areas which have prevented the gold from growing. The second sample (Figure 4.27) present an homogeneous growth of gold but a distorted profile of the holes walls. The O_2 plasma is more aggressive and therefore more effective in resist removal in the open

areas. However, its removal action is more isotropic than O_2/CF_4 gas mixture plasma, causing defects in the vertical walls of the structures in resist. The O_2/CF_4 gas mixture plasma is anisotropic, resulting in sharp vertical walls of the structures. It is less aggressive than the pure O_2 mixture, and for this reason the time of the process have to be extended. A possible disadvantage in excessive extent of etching time is the etching of the top of the resist template, resulting in a reduction of its height. Moreover, the process is not perfectly anisotropic and the etching of the vertical walls of the resist structure, even homogeneous, reduce the holes which, after electrochemical growth, result in smaller structures.

Concluding, we set the following recipe for adhesion layer removal:

O_2 ($sccm$)	CF_4 ($sccm$)	P (W)	Bias (V)	p ($mbar$)	t (s)
28.5	1.5	40	100	3.5 e^{-1}	45

The whole process has been repeated on silicon nitride membrane and silicon nitride covered silicon, to analyze the mask replica process.

In order to improve the contrast of the mask we used a $500nm$ thick silicon nitride membrane. The result of the process on membrane is shown in Figure 4.28. We ascribe the distorted pattern to the sum of the mechanical distortions occurring in both the membranes when in contact.
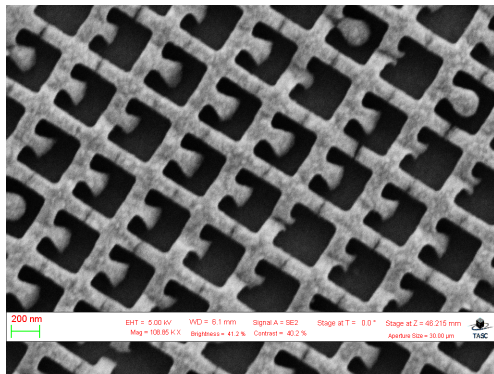

Figure 4.28: Sample in base plated silicon nitride membrane, after XRL, O_2/CF_4 plasma etching and electrochemical growth.
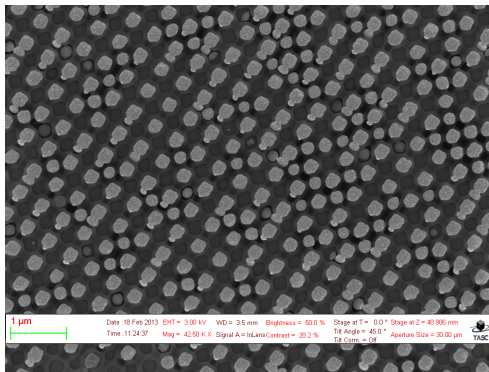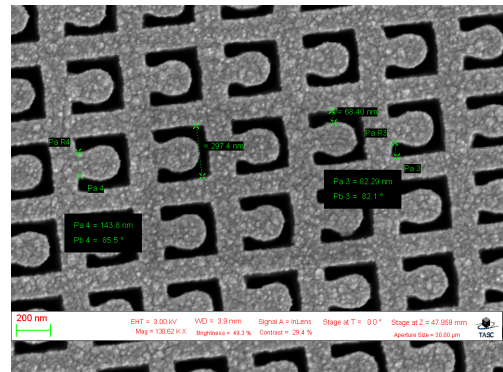

Figure 4.29: Sample in base plated silicon nitride covered silicon, after XRL, O_2/CF_4 plasma etching and electrochemical growth.

Figure 4.29 show the result of the process on base plated silicon nitride covered silicon. The dose is $1.460 J/cm^2$. The extent in the plasma process duration caused a reduction of the PMMA structure and, thus, of the holes

in the gold, without affecting SRR sharpness. To obtain the mask, the sample has to be processed as described in Section 4.1.1, removing silicon nitride and silicon from the opposite side to the patterned one to create the silicon nitride membrane sustaining the absorber pattern.

Conclusion

We used a prototype of the final pattern mask to study the XRL on negative resist (MICROPOSIT SAL601) and positive resist (Allresist AR-P 671.05 PMMA).

The high sensitivity of the SAL, united to the small features of the mask, its high filling factor and low contrast, and the difficulties in the control of low doses on LILIT beamline, makes this resist unsuitable for the fabrication of nanometric split ring resonators via X-Ray Lithography. Thus, we abandoned the negative resist lithography.

XRL on PMMA was analyzed to study the mask replica process. The poor adhesion of PMMA on gold forced us to use an adhesion layer between the PMMA layer and the substrate. The introduction of this layer complicates the fabrication process, summarized in the following list

1. adhesion layer deposition: MICROPOSIT SAL607 diluted in Sigma Aldrich Ethyl L-lactate (1:8) is spun on the substrate at $6000 rpm$ for $60 s$, then baked for $60 s$ at $105°C$;

2. PMMA layer deposition: Allresist AR-P 671.05 spun at $3000 rpm$ for $60 s$, then baked for $30 min$ at $180°C$;

3. X-ray lithography: optimized dose d= $1.730 J/cm^2$ for base plated silicon and d= $1.460 J/cm^2$ for base plated silicon nitride covered silicon;

4. PMMA development: immersion in H_2O:IPA=3:7 developing solution for $20 s$;

5. adhesion layer removal: plasma etching in O_2/CF_4 gas mixture for $45 s$;

6. gold growth: electrochemical process at I= $100 mA$ at $35°C$;

7. resist template removal: hot acetone.

The plasma etching affects the resist template formed in the lithographic and developing process, resulting in smaller structures compared to the parent positive tone mask ones. The mask replica process has to be performed not on membrane, but on nitride covered silicon to avoid mechanical distortion of mask and substrate. After patterning of the negative tone structure, the

membrane has to be produced removing silicon nitride and silicon from the non-patterned side of the sample.

4.2 X-Ray lithography: negative tone mask

In the previous phase of the fabrication optimization we established the positive resist process. Due to the PMMA poor adhesion on gold and ITO, as we will demonstrate in Section 4.2.2, a thin adhesion layer has to be deposited between PMMA and the conductive substrate. The adhesion layer removal introduce a supplementary step in the list of processes. The distortion problems arising from the membranes contact in the mask replica lithography, force us to produce the membrane after the patterning, adding another critical step to the process. The membrane fabrication after mask absorber patterning for multiple membranes mask is, at least, challenging.

The small feature of the mask replica and the poor adhesion of PMMA on the substrate will induce to use the same process for the sample fabrication. The defects of the negative tone mask replica will be, thus, reproduced and amplified in the sample fabrication.

All those reason induced us to consider the fabrication of a negative tone mask using EBL in order to reduce the fabrication step and the defects in the final samples.

4.2.1 X-ray mask

In order to study negative tone mask fabrication we took advantage of the Electron Beam lithographic facility at IOM-CNR. The acceleration of the beam, low compared to the $100KeV$ LaNN EBL, is $30KeV$. Despite the lower acceleration, the IOM-CNR electron beam lithographic facility is the ideal setup for the study of the feasibility of the negative mask fabrication process.

The fabricated mask has been used for the optimization of the XRL process. The membrane fabrication follows the process already reported in Section 4.1.1, summarized as:

1. base plating: evaporation of Cr/Au bi-layer ($10nm/20nm$) on one side of the silicon nitride double side covered silicon wafer;

2. UV-resist deposition: MEGAPOSIT SPR220 3.0 spun at $3500rpm$ for $45s$, baked at $115°C$ for $90s$, on both sides;

3. UV lithography: exposition at $3mW/cm^2$ for $18s$, post exposure bake at $115°C$ for $90s$ and development in MICROPOSIT MF24A for $30s$;

4. RIE: O_2 plasma etching of the silicon nitride;

5. wet etching: wet etching of silicon in 5M KOH solution at $65°C$ for $12h$.

Silicon nitride thickness of $500nm$ has been chosen with the intent to increase the mask contrast. The plasma etching time is, then, reduced. The parameters of the $500nm$ thick silicon nitride etching process are reported in the following table:

O_2 $(sccm)$	CF_4 $(sccm)$	P (W)	Bias (V)	p $(mbar)$	t (min)
1.5	28.5	150	250	3.5 e^{-1}	10

Electron Beam Lithography at 30 KeV

EBL of the negative tone mask has been performed at $30KeV$ acceleration voltage and beam current of $130pA$. In order to obtain a negative tone pattern, the CAD file driving the e-beam writing has been designed to expose of the area outside the SRR.

The dose optimization was performed on $500nm$ thick silicon nitride single membranes, covered by approximatively $550nm$ thick Allresist AR-P 671.05, spun at $3000rpm$ for $60s$ and baked at $180°C$ for $30min$. The developing time was fixed at $20s$ in the H$_2$O:IPA=3:7 development solution.

The dose matrix chips size is $50 \times 50\mu m$. In Figure 4.30 and 4.31 we show examples of the effect of low and high dose to the sample, respectively, after development and electrochemical growth at I= $100mA$, $35°C$ for $30s$.
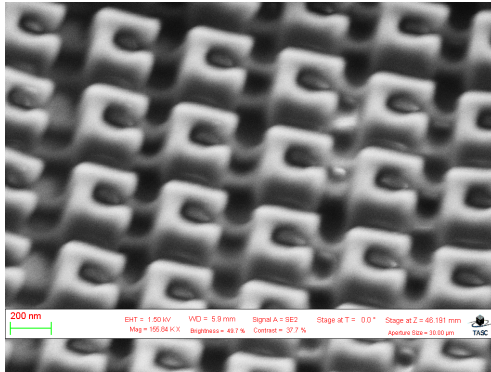

Figure 4.30: EBL dose matrix. Low dose chip on silicon nitride membrane, after gold growing
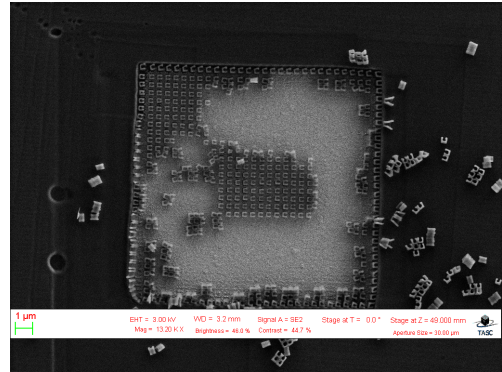

Figure 4.31: EBL dose matrix. High dose chip on silicon nitride membrane, after gold growing

The final negative SRR array was fabricated on an area of $300 \times 300\mu m$, enough to optimize XRL. The pattern area and the structures density caused

shifting on the electron beam during the exposition over the whole $300 \times 300\mu m$ area(Figure 4.32). To reduce the shifting effect we produced the array pattern in CAD file by dividing the total array in modules, to drive the electron beam in writing smaller areas at a time: first in rows $900nm \times 300\mu m$ (Figure 4.33), then in squares $30 \times 30\mu m$ (4.34). It is clear from the images the better result we achieve was the square modules option. The result is still not free by shifting effects, therefore the mask can not be used to produce the final samples. It is possible, however, to use it for XRL optimization.
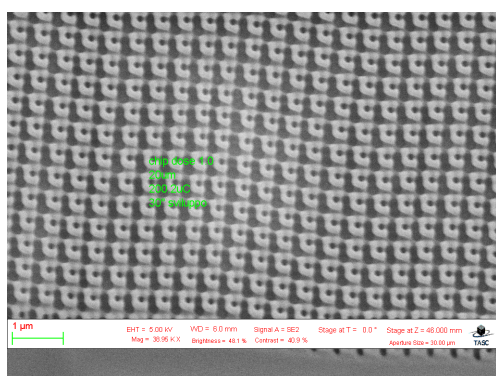

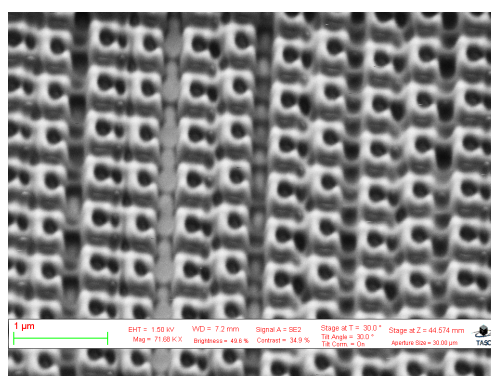Figure 4.32: Shifting of the electron beam in the exposition of the total area of the array.

Figure 4.33: SEM image of the sample produced by dividing the total array area in rows

4.2.2 X-ray lithography

In this phase we optimize the XRL process, with the negative tone mask on transparent substrate, ITO on glass.
The substrate is Sigma Aldrich glass slides covered by $100nm$ of ITO. The substrate preparation includes glass slide cutting and cleaning. The ITO covered glass cleaning is a three step procedure, during which the substrate in immersed in an ultrasonic bath of water and soap, then water and finally IPA for $10min$ each.
We first test the adhesion of PMMA on ITO. The result showed the PMMA has a poor adhesion on ITO. We introduced, thus, the diluted SAL adhesion layer between the PMMA and the substrate, as already described in Section 4.1.3.
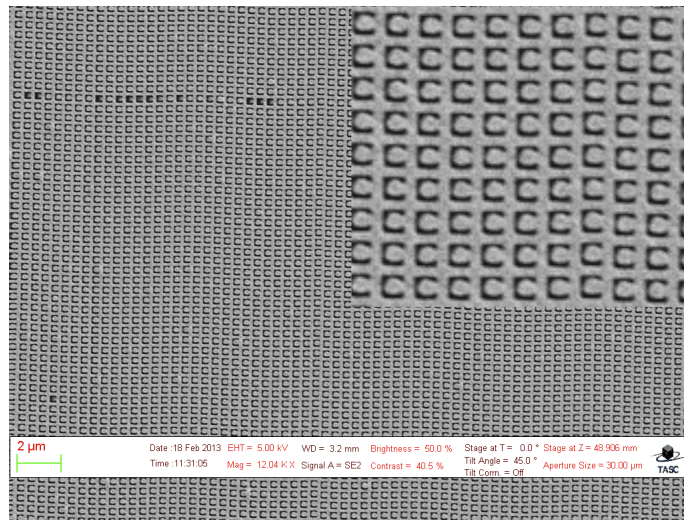
Figure 4.34: SEM image of the sample produced by dividing the total array area in squares. Enlarged detail at the right/top of the picture.
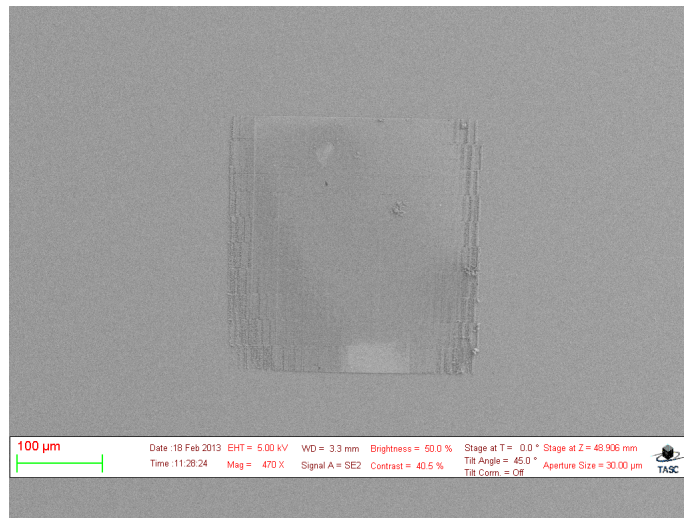

Figure 4.35: SEM of the chip of SRR on the negative tone mask fabricated by $30KeV$ EBL.

PMMA on ITO

A test of the adhesion of PMMA on ITO was performed. The substrate has been cleaned following the procedure given in 4.2.2 and covered by All-resist AR-P 671.05, spun at $3000rpm$ for $60s$ and baked at $180°C$ for $30min$.

The developing time was fixed at $20s$ in the H$_2$O:IPA=3:7 development solution.

The correct dose was fixed at d= $2.432 J/cm^2$ by dose metic analysis. After exposure and development, the gold has been deposited by electrochemical growth in direct current mode at I= $100mA$, $35°C$ for $30s$. The result is shown in Figure 4.36 and 4.37.
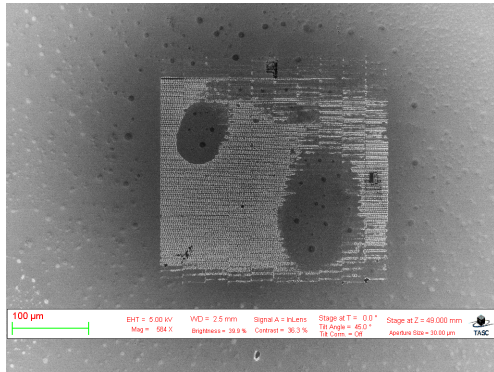

Figure 4.36: Chip of SRR after XRL exposure, development, gold growth and resist removal in hot acetone.
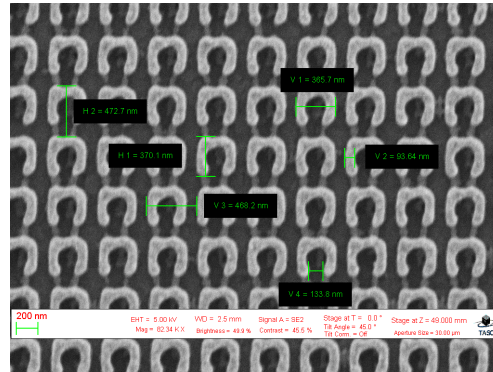

Figure 4.37: Chip of SRR after XRL exposure, development, gold growth and resist removal in hot acetone (detail).

Though the SRR in Figure 4.37 are well shaped and correspond the the negative pattern on the mask (Figure 4.34), the image of the whole chip (Figure 4.36) show large non-patterned areas. The image is taken after electrochemical gold growth and resist template removal in acetone. The non-patterned areas are filled with gold, indicating the grown lifted the resist template, probably already detached from the substrate. The effect indicates a poor adhesion of PMMA on ITO.

PMMA and SAL on ITO

To improve the adhesion of PMMA on ITO a thin layer of diluted SAL was deposited between the PMMA and the substrate. The adhesion layer deposition and removal processes have been optimized in a previous phase of this work.

The ITO covered glass has been cleaned by a three step ultrasonic bath, then covered by a thin layer ($< 20nm$) of MICROPOSIT SAL607 diluted in Sigma Aldrich Ethyl L-lactate (1:8), spun on the substrate at $6000rpm$ for $60s$, then baked for $60s$ at $105°C$. After the deposition of $550nm$ of Allresist

AR-P 671.05, spun at $3000rpm$ for $60s$ and baked at $180°C$ for $30min$, the sample is ready for the exposition.

A dose matrix fixed the dose at d= $2.720J/cm^2$. After the exposition the adhesion layer is removed by a plasma etching in O_2/CF_4 gas mixture:

O_2 $(sccm)$	CF_4 $(sccm)$	P (W)	Bias (V)	p $(mbar)$	t (s)
28.5	1.5	40	100	3.5 e^{-1}	45

Electrochemical gold deposition follows.

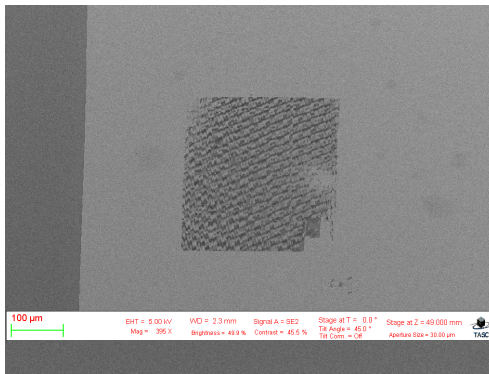The result of the process is presented in Figure 4.38 and 4.38. The improve-

Figure 4.38: Chip of SRR after XRL exposure, development, gold growth and resist removal in hot acetone. Diluted SAL used as adhesion promoter for PMMA.
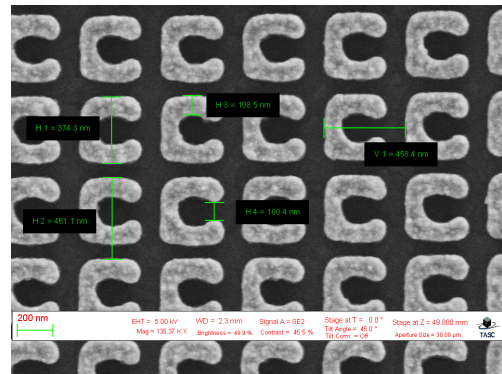

Figure 4.39: Chip of SRR after XRL exposure, development, gold growth and resist removal in hot acetone (detail). Diluted SAL used as adhesion promoter for PMMA.

ment given by the adhesion layer deposition are clear from the comparison of the result of the process without (Figure 4.36) and with (Figure 4.38) diluted SAL. The defects present on the edges of the chip are the replica of the defects present on the mask (Figure 4.35).

Conclusion

The results of EBL test on the fabrication of negative tone mask has been positive.

The subsequent optimization of XRL on ITO covered glass highlighted the poor adhesion of PMMA on ITO. The process involving diluted SAL as adhesion promoter, already fine tuned, has been applied with success to the transparent substrate.

4.3 X-Ray lithography: negative tone multi-membrane mask

The previous study on the feasibility of SRR fabrication using XRL have given positive result. The final phase of the fabrication activity is the production of multiple membrane mask, to be used for the fabrication of SRR array on transparent substrate.

In order to have the possibility to perform multiple measurement on the same sample, and eventually to perform microfluidic measurement, the sample geometry is reported again in Figure 4.40 has been designed.
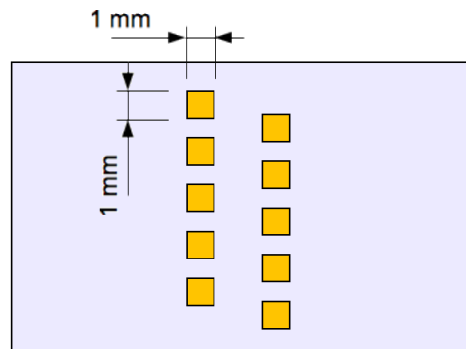

Figure 4.40: Sample design to perform multiple measurement and microfluidic experiment.

The sample design presents two staggered column of five chips each, $3mm$ distant. The shift between the columns is $1mm$. Each chip has an area of $1 \times 1mm$ and $2mm$ period.

In order to produce this geometry on the sample using XRL, two mask design are possible: a large ($> 1cm^2$) single membrane mask or a multiple membrane mask. The second design is more stable and easy to handle compared to the first one. To improve mask contrast we are using $500nm$ thick silicon nitride, which is extremely fragile and easy to break: the breakage of a single membrane of a multiple membrane does not imply the waste of the whole mask. The redundant number of chip makes the membrane breakage event less critical.

The multiple membrane fabrication has been studied and performed in this phase.

4.3.1   X-ray mask

The XRL mask, in this phase of the work, is composed by a multiple silicon nitride membrane substrate and a gold absorber fabricated using EBL and electrochemical gold deposition.

Silicon nitride multiple membrane

The silicon nitride membrane fabrication follow the scheme already presented in Sections 4.1.1 and 4.2.1. To obtain multiple membrane on the same frame a new UV mask (Figure 4.41) has been designed and fabricated. The
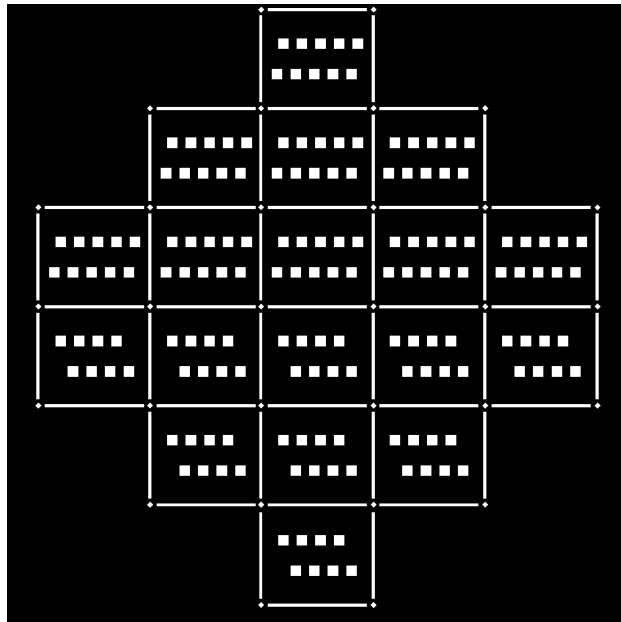
Figure 4.41: UV mask for producing multiple silicon nitride membrane on the same frame

UV mask has been designed to obtain 8-10 multiple membrane having an area of $1.2 \times 1.2mm$ on a total frame area of $18 \times 15mm$.
In Figure 4.42 we show a picture of the obtained multiple membrane.

Electron Beam Lithography and electrochemical growth

The multiple membranes frame has been covered with Allresist AR-P 671.05 spun at $3000rpm$ for $60s$. The resist has been baked at $180°C$ for $30min$.
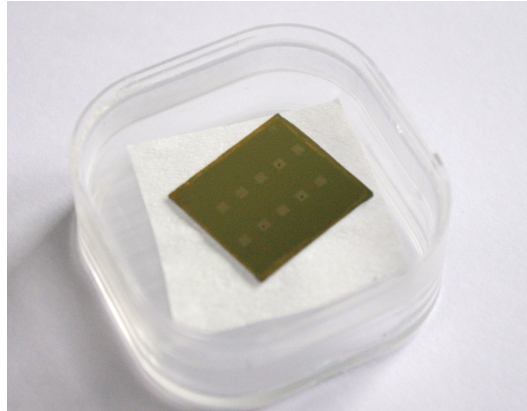
Figure 4.42: Picture of the multiple membrane

EBL has been performed at LaNN. The EBL worked in high resolution (HR) mode using a $100keV$ acceleration voltage and a beam current of $100pA$. The exposed sample has been developed in H_2O:IPA=3:7 developer solution. The metal deposition has been performed at IOM-CNR electrodeposition facility. In Figure 4.43 we show the SRR holes in one of the chip on the multiple membrane mask after gold growing and resist removing in hot acetone.

Figure 4.43: Top view of negative tone SRR mask.

The dimension of the SRR holes are: $l = 350nm$, $w = 80nm$, $d = 105nm$ and $a = 470nm$.

4.3.2   X-ray lithography
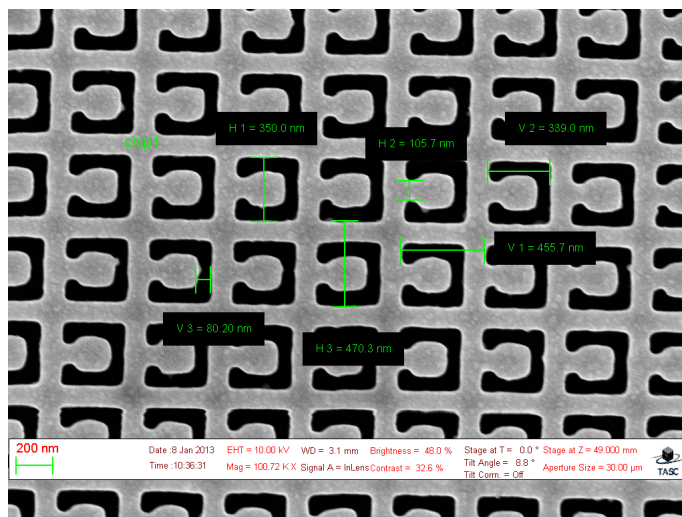
In the previous phases of the work we optimized the XRL process and sample fabrication. The final process of XRL on ITO covered glass and sample fabrication can be summarized as follows:

- ITO/glass preparation: three step ultrasonic bath in water and soap, water, and IPA;

- adhesion layer deposition: MICROPOSIT SAL607 diluted in Sigma Aldrich Ethyl L-lactate (1:8) is spun on the substrate at $6000rpm$ for $60s$, then baked for $60s$ at $105°C$;

- PMMA layer deposition: Allresist AR-P 671.05 spun at $3000rpm$ for $60s$, then baked for $30min$ at $180°C$;

- X-ray lithography: optimized dose d$= 1.730J/cm^2$ for base plated silicon and d$= 2.720J/cm^2$ for base plated silicon nitride covered silicon;

- PMMA development: immersion in H_2O:IPA=3:7 developing solution for $20s$;

- adhesion layer removal: plasma etching in O_2/CF_4 gas mixture for $45s$;

- gold growth: electrochemical process at I$= 100mA$ at $35°C$;

- resist template removal: hot acetone.

PMMA and SAL on ITO

We report here the result of the XRL process and sample finalization. A large number of multiple chip samples have been fabricated, obtaining SRR array at various height, from $200nm$ to $400nm$. In Figure 4.44, 4.45, 4.46 and 4.47 we show examples of the SRR structure on the final sample. Especially due to the plasma etching step, the dimensions of the SRR vary from sample to sample, as can be seen from the presented images. The average values are: $l = 398nm$, $w = 59nm$, $d130 = nm$ and $a = 460nm$.
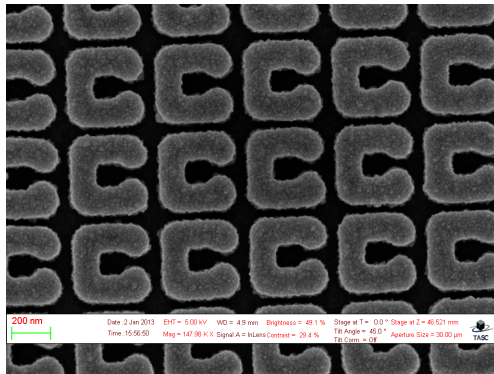
Figure 4.44: SEM image of sample produced using XRL and negative tone mask, on ITO covered glass, top view.
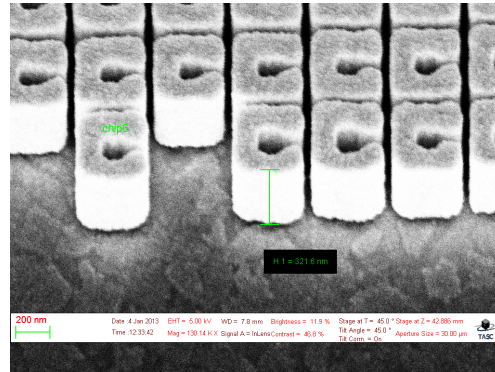
Figure 4.45: SEM image of sample produced using XRL and negative tone mask, on ITO covered glass, tilted view.
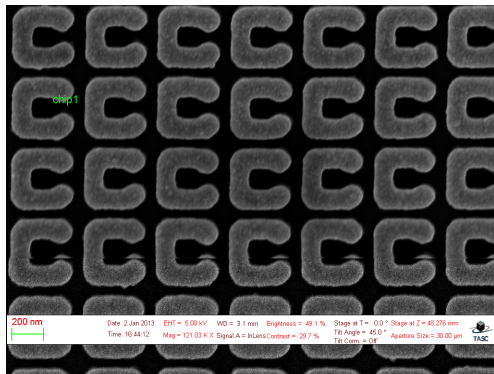
Figure 4.46: SEM image of sample produced using XRL and negative tone mask, on ITO covered glass, top view.
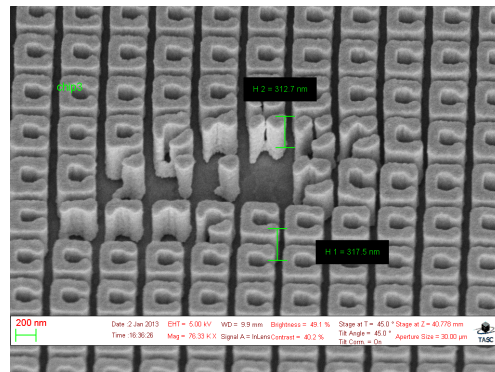
Figure 4.47: SEM image of sample produced using XRL and negative tone mask, on ITO covered glass, tilted view.

4.4 Conclusion

The X-ray lithographic and the related process have been studied, analyzed and optimized in this part of the thesis.

During the fabrication phase, the following task have been achieved:

- introduction of the H_2O:IPA=3:7 development solution;

- enhancement of PMMA adhesion on gold and ITO covered substrate

by introduction of SAL607 diluted in Ethyl L-lactate (1:8) as adhesion promoter;

- development of adhesion layer removal process;

- development of the XRL on PMMA and diluted SAL;

- fabrication of negative tone mask via EBL;

- design and fabrication of multiple membrane mask;

- fine tuning of the fabrication process involving UVL, XRL, EBL, RIE;

- sample fabrication on transparent substrate.

The request of multiple chip sample on transparent substrate, potentially suitable for microfluidic analysis, has been achieved.

Chapter 5

Charaterization

In this chapter we present the results of the characterization of the fabricated SRR samples and a preliminary test of the detection of a functionalization thiol monolayer.

Transmission analysis has been performed at LaNN in Padova, using the monochromatized 75W Xe lamp of a VASE (J.A. Woollam) Spectroscopic Ellipsometer with a wavelength resolution of 0.3nm. Transmission spectra of the fabricated samples have been acquired in the range $400 - 1100nm$, at normal incidence. The measurement have been performed for two polarization: p-polarization, electric field parallel to the gap of the SRR, and s-polarization, electric field perpendicular to the gap of the SRR. From now on we will refer to parallel polarization as p-polarization and perpendicular as s-polarization.

The measurement have been repeated after the samples have been functionalized with a monolayer of dodecanethiol, as a preliminary detection test.

We will first present the result for the fresh samples, in order to compare the simulated spectra to the measured ones. The spectra collected after functionalization are then compared to the spectra collected for the fresh samples.

5.1   Ellipsometry: Fresh sample

In this section we present the measured transmittance of the fabricated SRR chip. Transmission spectra were acquired in the range $400 - 1100nm$, step $3nm$, at normal incidence and p- and s-polarization values.
The first result we present is the trasmittance spectrum for the following SRR geometry:

l (nm)	w (nm)	d (nm)	h (nm)	a (nm)
400	130	50	220	460

The parameters has been measured on the SEM images, taken by the SEM Gemini Zeiss at IOM CNR in Trieste. In Figure 5.5 and 5.6 the SEM images of the sample are shown. The tilted images, from which the height of the structure is measured, are showing minor defects in the sample.
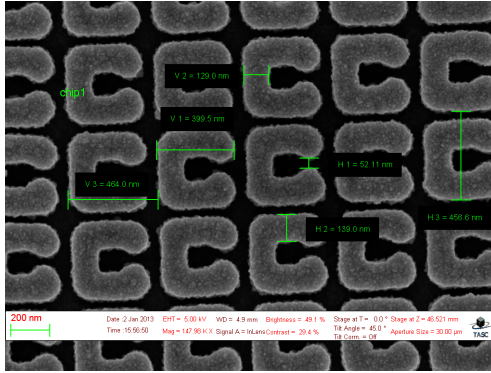

Figure 5.1: SEM image of the measured SRR array, $h = 220nm$. Top view.
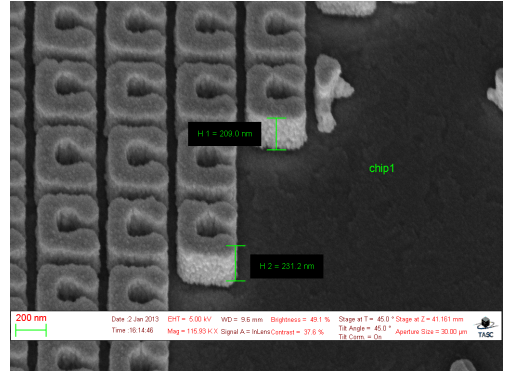
Figure 5.2:   SEM image of the measured SRR array, $h = 220nm$. Tilted view.

The results of the ellipsometric measurement for both polarization are compared to the simulated spectra in Figure 5.3 and 5.4. The measurement are shifted by approximatively $70nm$ from the simulated result. Despite the shift, the shape of the measured spectra follow the same trend of the simulated result. Possible causes of the shift may be the differences and the approximation done in the simulation.
The spectra for both polarization for the SRR array having the following geometric parameters are shown is Figure 5.7 and 5.8:

l (nm)	w (nm)	d (nm)	h (nm)	a (nm)
400	130	70	300	460

Figure 5.3: Transmittance over $400 - 1100nm$ wavelength. SRR height $h = 220nm$ Electric field polarized perpendicular to the gap. Blue: measured spectrum. Red: simulated spectrum.

Figure 5.4: Transmittance over $400 - 1100nm$ wavelength. SRR height $h = 220nm$ Electric field polarized parallel to the gap. Blue: measured spectrum. Red: simulated spectrum.
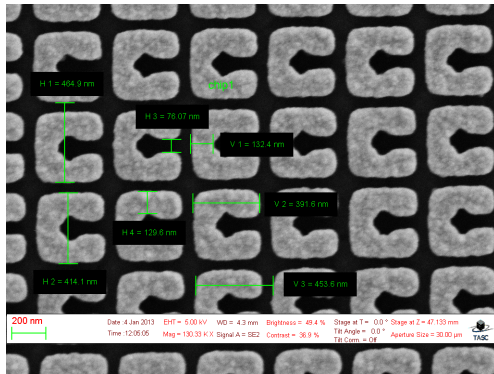
Figure 5.5: SEM image of the measured SRR array, $h = 300nm$. Top view.
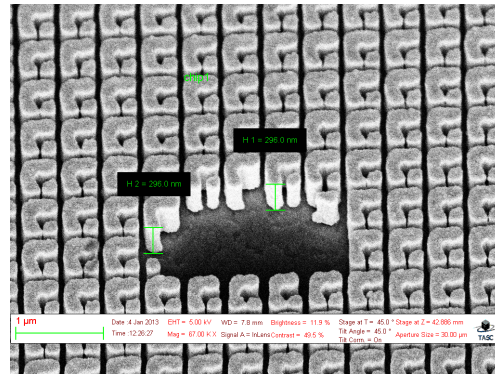
Figure 5.6: SEM image of the measured SRR array, $h = 300nm$. Tilted view.

As in the case $h = 200nm$, the measured spectra are blue shifted compared to the simulated spectra, while the trend is the same. The shift in the transmittance spectrum for the electric field parallel show a third peak which was not present in the simulated spectrum.

In Figures 5.9 and 5.10 we report the SEM images of a third sample, having $h = 400nm$, from which we obtained the following parameters:
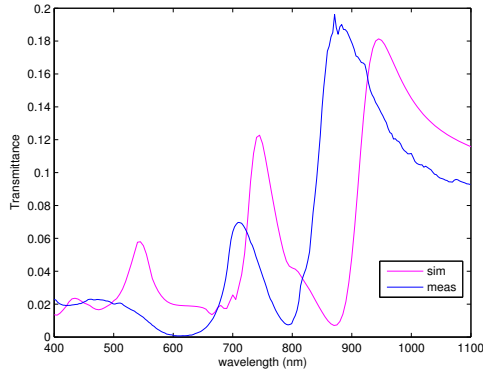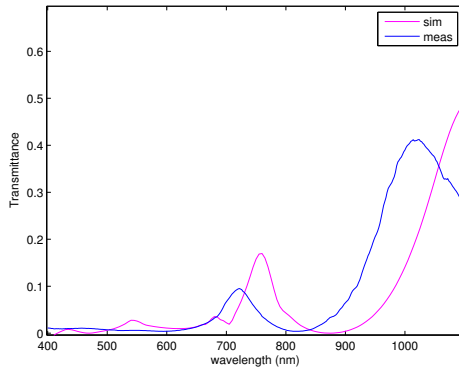
Figure 5.7: Transmittance over $400 - 1100nm$ wavelength. SRR height $h = 300nm$ Electric field polarized perpendicular to the gap. Blue: measured spectrum. Red: simulated spectrum.
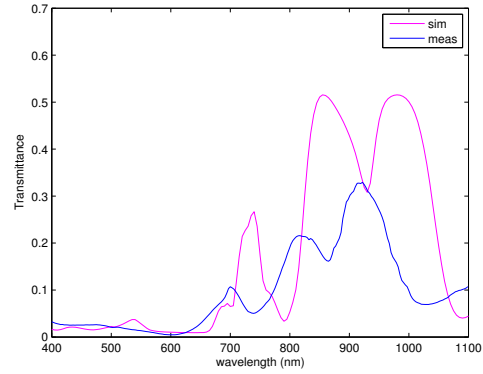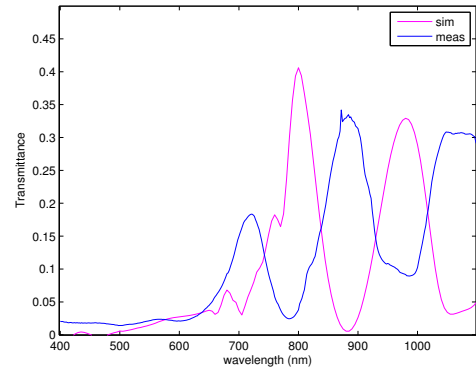

Figure 5.8: Transmittance over $400 - 1100nm$ wavelength. SRR height $h = 300nm$ Electric field polarized parallel to the gap. Blue: measured spectrum. Red: simulated spectrum.

l (nm)	w (nm)	d (nm)	h (nm)	a (nm)
390	120	60	400	460
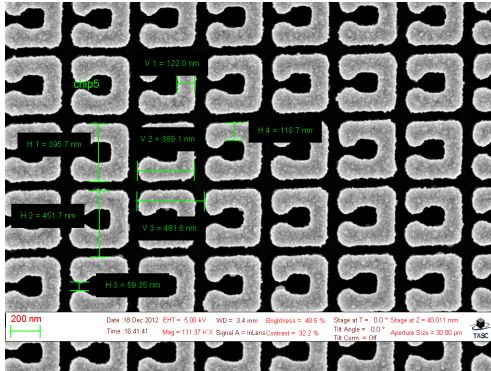
Figure 5.9: SEM image of the measured SRR array, $h = 400nm$. Top view.
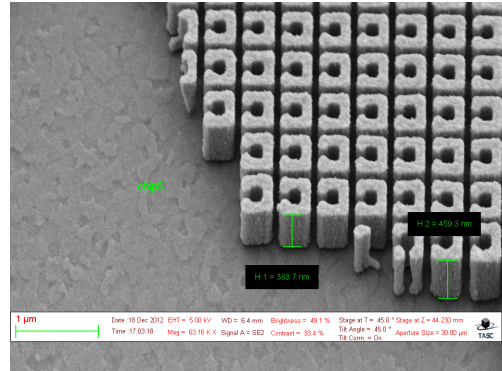
Figure 5.10: SEM image of the measured SRR array, $h = 400nm$. Tilted view.

Also in this case, the comparison with the simulated spectra, especially for s-polarization, show the blue shift of the measured spectra. Moreover, the rich peak response seen in the simulated result around $\lambda = 800nm$ is reduced
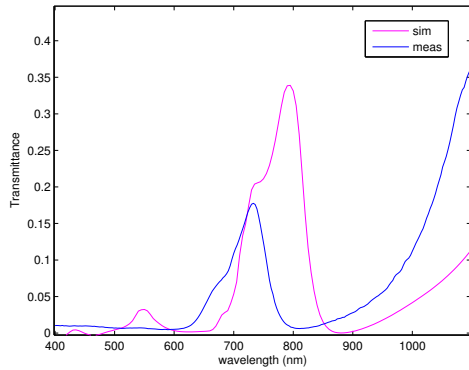
Figure 5.11: Transmittance over $400 - 1100nm$ wavelength. SRR height $h = 400nm$ Electric field polarized perpendicular to the gap. Blue: measured spectrum. Red: simulated spectrum.

Figure 5.12: Transmittance over $400 - 1100nm$ wavelength. SRR height $h = 400nm$ Electric field polarized parallel to the gap. Blue: measured spectrum. Red: simulated spectrum.

to a single broad peak for the measured spectra.

The observed differences in shift and shape between the measured and simulated spectra may be caused by the many discrepancies between the simulated conditions from the real ones:

- **dielectric constant:** in the simulations we used the dielectric constant found in literature, which may be different from the dielectric constant of the real material we used for fabrication;

- **ITO layer tickness:** to design the model we assumed the thickness on ITO is $100nm$; the commercial ITO thickness on every sample, however, may vary from this value;

- **gold roughness:** the roughness of the electrochemical grown gold, which can be up to few nm and worsens on ITO, has not been taken in account in the simulation;

- **inhomogeneities:** inhomogeneities in the height of the SRR in the chip may be present;

- **defects in the samples:** real samples present fabrication defects;

- **SRR sharpness:** the fabricated SRR structure is less sharp than the modelled one;

- **SEM accuracy:** the measurement of the SRR geometric parameters has been performed using the SEM control software: more accurate measurement may evidence differences in the measurement of the height of the structure up to $50nm$;

- **experimental condition:** the ideal simulated measurement condition may differ from the real experimental condition (alignment, angle of incidence on the sample...)

It is possible to improve the model introducing accurate measurement of the physical quantity and considering roughness.

5.2 Ellipsometry: Functionalized sample

In this section we present the result of the detection test.
We functionalized the samples using a self-assembled monolayer of dode-canethiol ($C_{12}H_{25}SH$, hereafter C_{12}), deposited on the gold surface at room temperature and performed the measurement in the same conditions. As described in the previous section, the spectra are collected in transmittance at normal incidence and p- and s-polarization values, in the $400 - 1100nm$ range.
The spectra before and after functionalization for the SRR array having $h = 200nm$, $h = 300nm$ and $h = 400nm$ are presented.
Figures 5.13 ($h = 200nm$), 5.14 ($h = 300nm$) and 5.15 ($h = 400nm$) show the result of the measurement before (blue) and after (red) functionalization for s-polarization. No field enhancement is present in the gap. Only few nanometers shift is shown for the spectrum after functionalization for $h = 300nm$. The presence on the monolayer of C_{12} is not detected by the resonances excited for s-polarization.
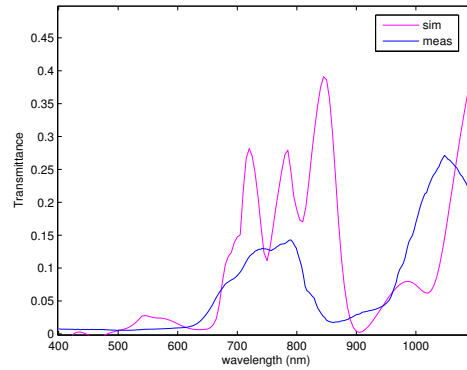

Figure 5.13: Transmittance over $400 - 1100nm$ wavelength. SRR height $h = 200nm$ Electric field polarized perpendicular to the gap. Blue: spectrum of the fresh sample. Red: spectrum of the functionalized sample.

In Figure 5.16 ($h = 200nm$), 5.17 ($h = 300nm$) and 5.18 ($h = 400nm$) the transmittance spectra in p-polarization for fresh (blue) and functionalized (red) sample are presented.
The presence of the monolayer of C_{12} is evidenced by a red shift, up to $30nm$, of the transmittance spectra of the functionalized samples. The shift is stronger on the peaks corresponding to resonances only due to the enhancement of the electric field in the gap area. The red shift of the spectrum

Figure 5.14: Transmittance over $400 - 1100nm$ wavelength. SRR height $h = 300nm$ Electric field polarized perpendicular to the gap. Blue: spectrum of the fresh sample. Red: spectrum of the functionalized sample.
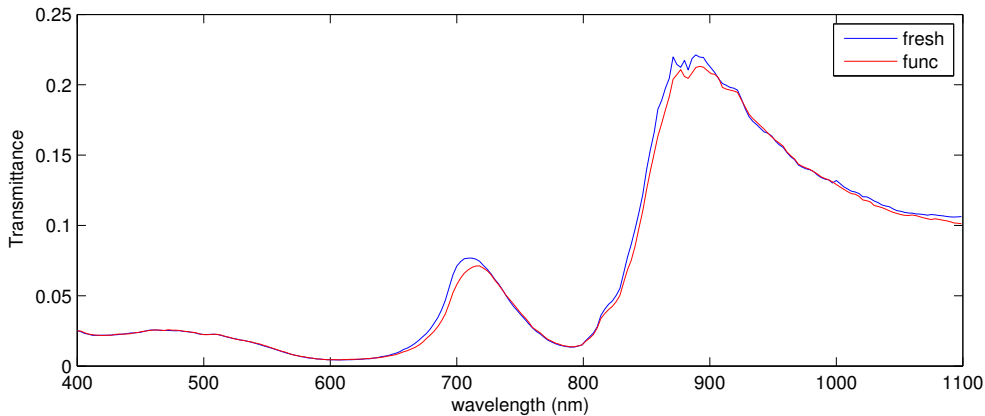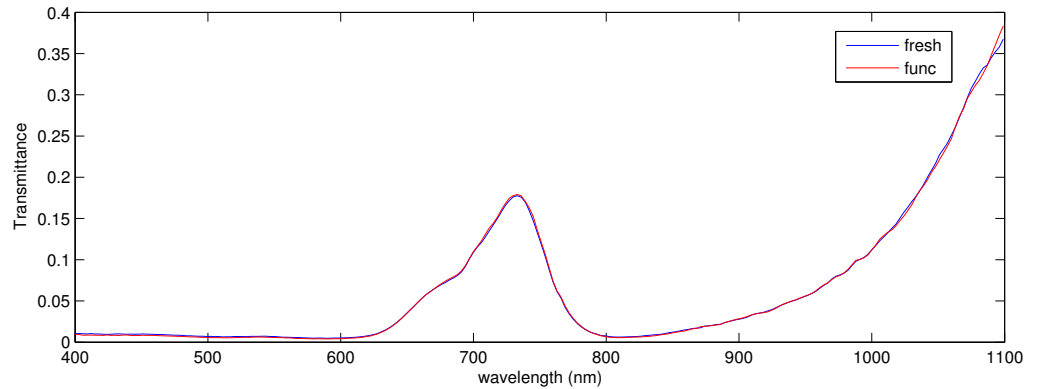

Figure 5.15: Transmittance over $400 - 1100nm$ wavelength. SRR height $h = 400nm$ Electric field polarized perpendicular to the gap. Blue: spectrum of the fresh sample. Red: spectrum of the functionalized sample.

of the functionalized sample compared to the one of the fresh sample is up to $20nm$ in $h = 200$ and $h = 300$ cases. The spectrum collected after functionalization, in those cases, repeats exactly the trend of the spectrum of the fresh sample, whereas the spectrum after functionalization, in the case $h = 400$, is distorted with the respect of the spectrum collected on the fresh sample, even if the shift due to the presence of the dodecanthiol monolayer is $30nm$ from peak to peak (at the resonance around $\lambda = 1050nm$). Further measurement will evidence if the effect is due to the height of the structures or to measurement errors.
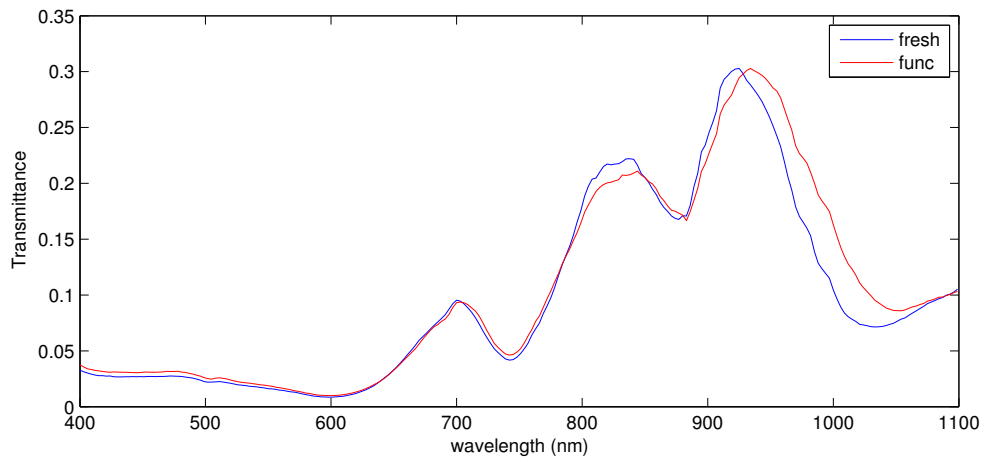
Figure 5.16: Transmittance over $400 - 1100nm$ wavelength. SRR height $h = 200nm$ Electric field polarized parallel to the gap. Blue: spectrum of the fresh sample. Red: spectrum of the functionalized sample.
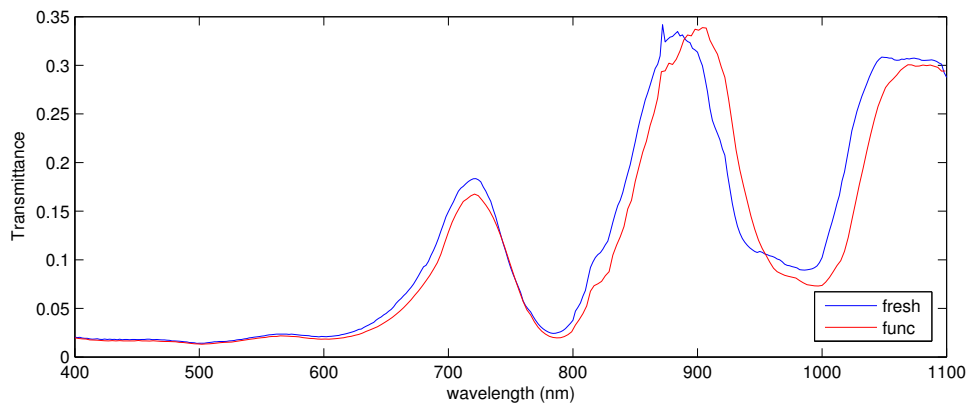
Figure 5.17: Transmittance over $400 - 1100nm$ wavelength. SRR height $h = 300nm$ Electric field polarized parallel to the gap. Blue: spectrum of the fresh sample. Red: spectrum of the functionalized sample.

However, the $20nm$ shift of the spectra, due to the presence of a monolayer of C_{12}, in p-polarization in the $h = 200$ and $h = 300$ cases is a positive result, supporting the idea to exploit the SRR geometry for sensing purposes.
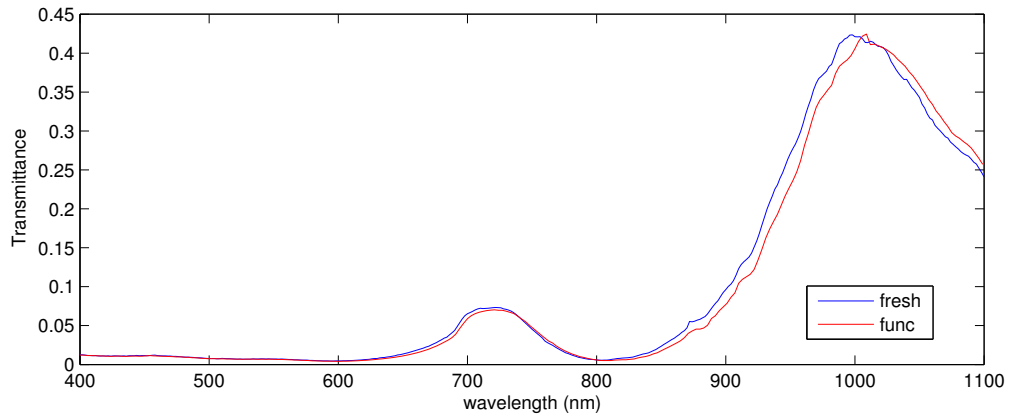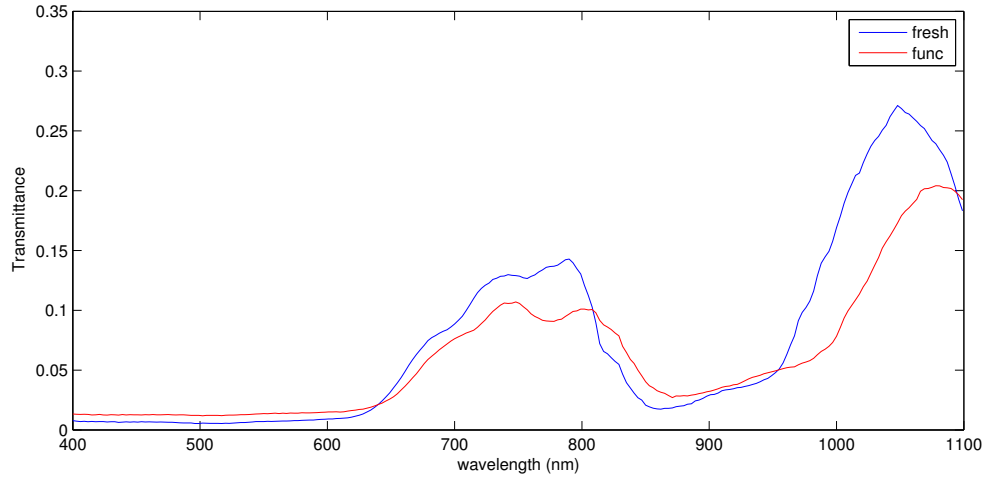
Figure 5.18: Transmittance over $400 - 1100nm$ wavelength. SRR height $h = 400nm$ Electric field polarized parallel to the gap. Blue: spectrum of the fresh sample. Red: spectrum of the functionalized sample.

5.3   Conclusion

The transmission spectra of the fabricated samples have been acquired using a spectroscopic ellipsometer, in the range $400 - 1100$nm at normal incidence and p- and s-polarization values.

The measures have been performed on the fresh and functionalizes samples, in order to compare measured and simulated spectra and to perform a detection test on the SRR structure.

The comparison of the simulated and collected spectra shows an agreement in the trend of the curve, but the measured spectra blue shifted almost $100nm$ with the respect of the simulated ones. This difference may be due to the discrepancies between the simulated model and the real sample. To improve the model, in the next future more realistic parameters will be implemented in the simulation.

The detection test of a monolayer of dodecanthiol has shown a red-shift of $15 - 20nm$ with the respect of the fresh sample spectra in p-polarization configuration. This encouraging result will be the starting point of a more accurate analysis of the SRR use as sensing geometry.

Chapter 6

Future work and conclusion

This thesis work has been devoted to the design, the fabrication and the characterization of nano split ring resonator (SRR) array on transparent substrate in order to allow optical transmission analysis for sensing application in the visible - near-infrared range.

The final sample has been designed in order to permit multiple analysis and to suit future microfluidic measurement. This request implied the need to fabricate multiple large area ($1 \times 1mm^2$) array of nanostructures.

The optical response of the SRR to visible-near infrared light illumination has been simulated by the finite element analysis software COMSOL Multiphysics. The structure model has been built according to the expected fabricated structure.

We analyzed the case of normally impinging plane wave with electric field polarized parallel and perpendicular to the gap, focusing our attention on the peaks in transmittance spectra, covering the visible-infra red wavelength range ($400 - 1100nm$). Near field analysis of the distribution of the electric and magnetic field enhancement corresponding to transmittance peak has been used in order to understand the origin of the resonances.

The near field analysis evidenced the origin of the resonances as plasmonic modes in the gap of the structure and Fabry-Pérot modes between two contiguous SRRs. In particular, the analysis of the near field images of the simulation in which the electric field is perpendicular to the gap, evidenced a resonance between SRRs found at the same wavelength in the other polarization simulation results, making the first set of peaks in the transmittance spectra as the superimposition of plasmonic modes in the gap and Fabry-Pérot resonances. The electric field polarized parallel to the gap, on the other hand, causes a strong field enhancement and confinement in the SRR gap region.

The analysis on the changes of the transmittance spectra due to the change

of the height of the SRR has been performed, evidencing the strong influence this parameter has on the shape and the position of the peaks in transmittance.

A qualitative test on the sensitivity of the structures to changes in the bulk refractive index of the dielectric media surrounding the SRR was performed, showing a red shift in the transmittance spectra.

The design of the structure done by the simulating tools was exploited in the fabrication phase.

In order to fabricate multiple arrays on nano SRR on transparent substrate, a series of test has been performed.

At first, we optimized resist development and electrochemical growth, using a positive tone mask whose pattern has a lower density of structures compared to the final geometry. In order to study the mask replica and the sample fabrication, a positive and a negative resist have been employed on three different substrates.

The results obtained with the low density positive tone mask have been used as a starting point for the optimization of the process using a high density, positive tone mask. Due to the problems arising from the high density of structures and the low contrast of the mask, the combined use of positive resist and adhesion promoter has been introduced, while the direct fabrication of the sample using the negative resist has been abandoned.

The opportunity to design and fabricate negative tone mask was explored. The positive result obtained by this study drove us to fabricate the negative tone mask for the multiple chip sample fabrication. In the last part of the fabrication optimization a new mask concept has been design and produced and the multiple chip sample has been fabricated on a transparent substrate.

Summarizing, the achieved fabrication technical tasks are the following:

- introduction of the H_2O:IPA=3:7 high contrast development solution;

- enhancement of the positive resist polymethylmethacrylate (PMMA) adhesion on gold and ITO (Indium-Tin Oxide) covered substrate by introduction of negative resist MICROPOSIT SAL607 diluted in Ethyl L-lactate (1:8) as adhesion promoter;

- development of adhesion layer removal process;

- development of the X-Ray Lithography on the adhesion promoter/resist bilayer;

- fabrication of negative tone mask via Electron Beam Lithography;

- design and fabrication of multiple membrane mask;

- fine tuning of the fabrication process involving UV Lithography, X-Ray Lithography, Electron Beam Lithography, Reactive Ion Etching;

- multiple chip sample fabrication on transparent substrate.

The transmission spectra of the fabricated samples have been acquired in the range $400 - 1100nm$, at normal incidence, using a spectroscopic ellipsometer with a wavelength resolution of 0.3nm. The measurement have been performed for two polarization: p-polarization, electric field parallel to the gap of the SRR, and s-polarization, electric field perpendicular to the gap of the SRR, of fresh and functionalized samples. The samples have been functionalized using a self-assembled monolayer of dodecanethiol ($C_{12}H_{25}SH$) deposited on the gold surface at room temperature.

The comparison of the simulated and collected spectra shows an agreement in the trend of the curve, but the measured spectra blue shifted almost $100nm$ with the respect of the simulated ones.

The detection test of a monolayer of dodecanthiol has shown a red-shift of $15 - 20nm$ with the respect of the fresh sample spectra in p-polarization configuration.

The results collected in this thesis will be the starting point of a more accurate analysis of the SRR use as sensing geometry.

Further improvement of the research are planned.

The difference of the simulated spectra from the measured ones may be due to the discrepancies between the simulated model and the real sample. To improve the model, in the next future more realistic parameters will be implemented in the simulation, as an example introducing accurate measurement of the physical quantity and considering gold roughness.

The result of the characterization and the detection test, though still preliminary, are encouraging. In the next future we aim to perform accurate test on the sensitivity of the geometry and to test the design of the sample for microfluidic measurements.

Appendix A

LILIT beam line

LILIT (Laboratory for Interdisciplinary LIThography) is a lithographic beamline based on a bending magnet, working from soft ($1.5 KeV$) to hard ($10 KeV$) X-rays, installed on the third generation synchrotron ELETTRA (Trieste, Italy) [58][59].

Even though wigglers and undulators are the insertion devices a third generation synchrotron is optimized to use, some of the characteristics of such a synchrotron are advantageous also for lithographic beamline based on bending magnets. In particular, the high brightness of the electron beam makes it possible to collect intense photon flux with only few milliradians of horizontal acceptance. As a consequence, the source is symmetric in the horizontal plane: in this way it is possible to use a toroidal mirror in order to optimize the lithographic image, avoiding the use of a more complex aspherical optics. The high brightness, moreover, is responsible of the small divergence that produces a negligible run-out of the lithographic image: the field distortion on the mask/sample plane is then in the range of few nanometers. The intensity distribution at mask/sample plane is uniform within 3%.

The peculiarity of LILIT beamline is the wide lithographic window, achieved by combining high-pass filters (Berillium window) with low-pass filters (mirrors at increasing angle of incidence). The soft X-ray range (photon energy between 1 and $2 KeV$) is used to achieve high lithographic resolution (see Figure A.1), while the hard X-ray region (photon energy higher than $5 KeV$) to expose sensitive materials of thickness of tens on microns (see Figure A.2). The optical layout of the beamline consists of a plane mirror (M1), placed at $14 m$ from the source and a second toroidal mirror (M2) placed at $2 m$ from M1. The total length of the beamline, measured from the front end port of the bending magnet, is $13.3 m$.

An adjustable slit, a Beryllium window and an additional filter are located before M1. The adjustable slit select the solid angle under which the syn-
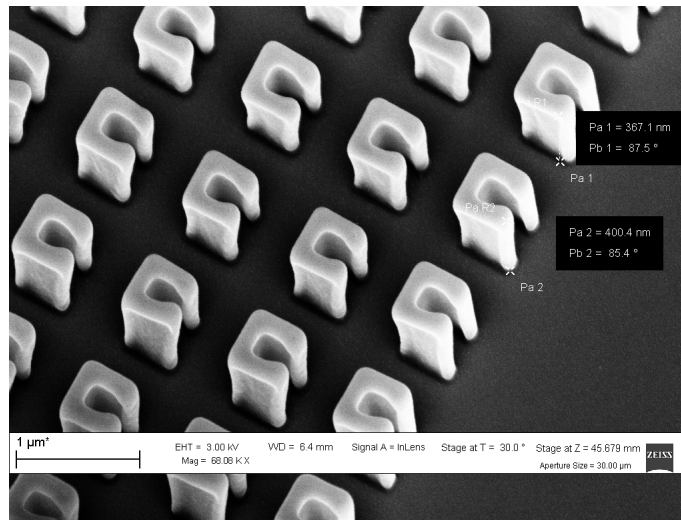
Figure A.1: In this figure it is shown the result of XRL on a thin layer of PMMA in the soft X-ray regime, in particular the small resolution achieved.

chrotron radiation is collected.

The collection angles have been fixed at $6mrad$ in the horizontal plane and $0.83mrad$ in the vertical plane. The latter value corresponds to the natural divergence of the synchrotron radiation in the soft X-ray regime under the standard operating condition of the beamline.

Further adjustable slits for the beam shaping and a photon shutter are placed after M2, close to the end of the beamline (see Figure A.3). A second Beryllium window closes the ultra vacuum part of the beamline, and the X-ray beam is then delivered in Helium flux (at atmospheric pressure), within a snout, to the exposure stage, located in a class 10 clean room. The mirrors act like a low pass energy filters. They are typically made of silicon coated with a low roughness gold film, typically of the order of 0.5nm. Their reflectivity strongly depends on the wavelength on the beam angle of incidence. The mirrors angles θ_1 and θ_2 respectively for the first and the second mirror operate at very grazing to the surface in order to allow a substantial fraction of the incoming radiation of the X- ray beam to be reflected. In fact, an increase of the angle θ_1 decreases the mirror reflectivity of the lower wavelengths providing a rejection of the hard part of the spectrum energy (low-pass filter).

The combined action of both mirrors produces image of the source at the mask/sample location whose size is $3 \times 50mm^2$.

The spectral composition and flux of the X-ray beam depends on the precise direction at which photons are collected within the emission cone of
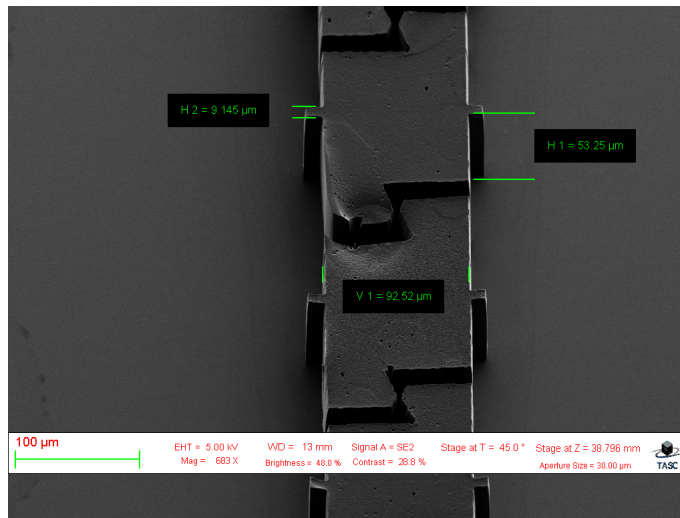
Figure A.2: In this figure it is shown the result of XRL on over $50\mu m$ layer of PMMA in the hard X-ray regime.

$\gamma^{-1} = mc^2/E$ radiant of divergence. The exposure of a sample in static conditions would produce, then, a non-uniform dose as a function of the relative position of the irradiated area of the resist with respect to the center of the beam. The sweeping of the electrons in the plane of their orbit averages the intensity and the spectral distribution in the horizontal direction, while the non-uniformity in the vertical direction can be averaged by vertically scanning the mask/sample assembly across the beam. Uniform exposure doses can be obtained on rectangular areas with both edges of few centimeters.

On LILIT beamline, an exposure stage consists of a granite scanner on which it is possible to mount the sample holder, held in position by vacuum circuit. During the exposure, the mask/sample assembly oscillates in front of the snout, to expose the correct sample area and to uniform the exposure. Scan ranges from few millimiters up to four centimeters, with a precision of few microns; it is also possible to indicate scanning speed. A LabVIEW based control software is installed on a personal computer in the adjacent class 100 clean room, separated from the class 10 exposure cleanroom by a leaded door for radiation protection reasons. Besides controlling the exposure, the software recognizes not only the exposure status itself, but also the status of the beamline and the accelerator. The electron beam current stored inside Elettra synchrotron is recorded to calculate the deposited dose value.

In the last years a goniometric stage has been designed and mounted on the granite scanner in order to achieve tilted and rotated exposure.
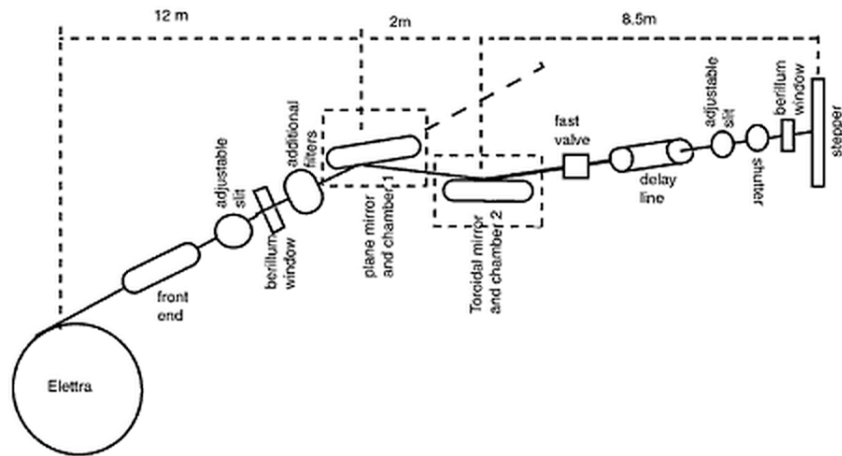
Figure A.3: LILIT beamline scheme

Acknowledgements

Bibliography

[1] Imogen M Pryce, Yousif a Kelaita, Koray Aydin, and Harry a Atwater. Compliant metamaterials for resonantly enhanced infrared absorption spectroscopy and refractive index sensing. *ACS nano*, 5(10):8167–74, October 2011.

[2] Ertugrul Cubukcu, Shuang Zhang, Yong-shik Park, Guy Bartal, and Xiang Zhang. Split ring resonator sensors for infrared detection of single molecular monolayers. *Applied Physics Letters*, 95(043113):2–4, 2009.

[3] Birgit Paivanranta, Hannes Merbold, Reto Giannini, Luca Buchi, Sergey Gorelick, Christian David, Jorg F. Lofflet, Thomas Feurer, and Yasin Ekinci. High Aspect Ratio Plasmonic Nanostructures for Sensing. *ACS nano*, 5(8):6374–6382, 2011.

[4] Alasdair W Clark, Andrew Glidle, David R S Cumming, and Jonathan M Cooper. Plasmonic Split-Ring Resonators as Dichroic Nanophotonic DNA Biosensors. *American Chemical Society*, 15(7):17615–17619, 2009.

[5] Sergey Gorelick, Vitaliy A Guzenko, Joan Vila-comamala, and Christian David. Direct e-beam writing of dense and high aspect ratio nanostructures in thick layers of PMMA for electroplating. *Nanotechnology*, 21, 2010.

[6] Zoran Jakšić, Olga Jakšić, Zoran Djurić, and Christoph Kment. A consideration of the use of metamaterials for sensing applications: field fluctuations and ultimate performance. *Journal of Optics A: Pure and Applied Optics*, 9(9):S377–S384, September 2007.

[7] William L Barnes, Alain Dereux, and Thomas W Ebbesen. Surface plasmon subwavelength optics. *Nature*, 424(August):824–830, 2003.

[8] Maier. *Plasmonics Fundamentals and Applications*. Springer, 2007.

[9] A. W. Clark. *Nanophotonic split-ring resonators as dichroics for molecular spectroscopy.* PhD thesis, University of Glasgow, 2009.

[10] John N. Helbert, editor. *Handbook of VLSI Microlithography.* Noyes, 2001.

[11] Massimo Tormen, Gianluca Grenci, Benedetta Marmiroli, and Filippo Romanato. X-ray lithography : fundamentals and applications . ISTE Wiley, 2010.

[12] H.D Bauer, editor. *LIGA Technique, Training in Microsystems UETP MEMS course.* 1994.

[13] Syed Rizvi, editor. *Handbook of Photomask Manufacturing Technology.* Taylor & Francis, 2005.

[14] Nasser Kanani. *Electroplating.* Elsevier Ltd, 2004.

[15] Joseph Goldstein, Dale Newbury, David Joy, Charles Lyman, Patrick Echlin, Eric Lifshin, Joseph Michae, and I Charles. *Scanning Electron Micros id X-Ray Microanalysis.* Kluwe Academic/Plenum Publisher, 2003.

[16] H.G. Tompkins and E.A. Irene, editors. *Handbook of Ellipsometry.* Springer, 2005.

[17] Jirí Homola. Present and future of surface plasmon resonance biosensors. *Analytical and bioanalytical chemistry*, 377(3):528–39, October 2003.

[18] N. P. Johnson, a. Z. Khokhar, H. M. Chong, R. M. Rue, T. J. Antosiewicz, and S. McMeekin. A review of size and geometrical factors influencing resonant frequencies in metamaterials. *Opto-Electronics Review*, 14(3):187–191, September 2006.

[19] Vladimir M. Shalaev. Optical negative-index metamaterials. *Nature Photonics*, 1(1):41–48, January 2007.

[20] Stefan Linden, Christian Enkrich, Martin Wegener, Jiangfeng Zhou, Thomas Koschny, and Costas M Soukoulis. Magnetic response of metamaterials at 100 terahertz. *Science (New York, N.Y.)*, 306(5700):1351–3, November 2004.

[21] Na Liu and Harald Giessen. Coupling effects in optical metamaterials. *Angewandte Chemie (International ed. in English)*, 49(51):9838–52, December 2010.

[22] Jordi Naqui, Miguel Durán-Sindreu, and Ferran Martín. Novel Sensors Based on the Symmetry Properties of Split Ring Resonators (SRRs). *Sensors*, 11(8):7545–7553, July 2011.

[23] John F O Hara, Ranjan Singh, Igal Brener, Evgenya Smirnova, Jiaguang Han, Antoinette J Taylor, and Weili Zhang. Thin-film sensing with planar terahertz metamaterials : sensitivity and limitations Abstract :. *Optical Society of America*, 16(3):1786–1795, 2008.

[24] J.A. Gordon, C.L. Holloway, J. Booth, S. Kim, Y. Wang, J. Baker-Jarvis, and D.R. Novotny. Fluid interactions with metafilms/metasurfaces for tuning, sensing, and microwave-assisted chemical processes. *Physical Review B*, 80(20):205103, 2011.

[25] M. Labidi, J.B. Tahar, and F. Choubani. Meta-materials application in thin-film sensing and sensing liquids properties. *Optix Express*, 19(19):A733–739, 2011.

[26] W. Withayachumnankula, K. Jaruwongrungseeb, A. Tuantranontc, C. Fumeauxa, and D. Abbotta. Metamaterial-based microfluidic sensor for dielectric characterization. *Sensors and Actuators A: Physical*, 189(15):233–237, 2012.

[27] F Romanato, L Businaro, L Vaccari, S Cabrini, and P Candeloro. Fabrication of 3D metallic photonic crystals by X-ray lithography. *Microelectronic Engineering*, 68:479–486, 2003.

[28] Jaeyoun Kim. Joining plasmonics with microfluidics: from convenience to inevitability. *Lab on a chip*, 12(19):3611–23, October 2012.

[29] H O Moser, B D F Casse, O Wilhelmi, and B T Saw. Terahertz Response of a Microfabricated Rod-Split-Ring-Resonator Electromagnetic Metamaterial. *Physical Review Letters*, 94(6), 2005.

[30] B D F Casse, H O Moser, J W Lee, M Bahou, S Inglis, and L K Jian. Towards three-dimensional and multilayer rod-split-ring metamaterial structures by means of deep x-ray lithography. *Applied Physics Letters*, 90:89–91, 2007.

[31] Raether. Surface Plasmon on smooth and rough surface and on grating, 1988.

[32] M.L. Brongersma and P.G. Kik, editors. *Surface Plasmon Nanophotonics*. Springer, 2007.

[33] Jiri Homola, editor. *Surface Plasmon Resonance Based Sensors.* Springer, 2006.

[34] J.N. Anker, W.P. Hall, O. Lyandres, N.C. Shan, J. Zhao, and R.P.V. Duyne. Biosensing with plasmonic nanosensors. *Nat. Mater.*, 7:422–453, 2008.

[35] Basudev Lahiri, Ali Z Khokhar, Richard M De La Rue, Scott G Mcmeekin, and Nigel P Johnson. Asymmetric split ring resonators for optical sensing of organic materials. *Optics Express*, 17(2):1107–1115, 2009.

[36] Humeyra Caglayan, Semih Cakmakyapan, Sarah A Addae, Melissa A Pinard, Deniz Caliskan, Kadir Aslan, and Ekmel Ozbay. Ultrafast and sensitive bioassay using split ring resonator structures and microwave heating. *Applied Physics Letters*, 97:2010–2012, 2010.

[37] M.J. Madou. *Fundamentals of Microfabrication.* CRC Press, 2002.

[38] E. Hutter and J.H. Fendler. Exploitation of Localized Surface Plasmon Resonance. *Advanced Materials*, 16(19):1685–1706, 2004.

[39] S.A. Ramakrishna and T.M. Grzegorczyk. *Physics and Applications of Negative Refractive Index Materials Physics and Applications of Negative Refractive Index Materials.* SPIE, CRC, 2009.

[40] Tie Jun Cui, David R. Smith, and Ruopeng Liu, editors. *Metamaterials Theory, Design and Applications.* Springer, 2010.

[41] V.G. Veselago. The electrodynamics of substances with simultaneously negative values of ϵ AND μ. *Physics-Uspekhi*, 10(4):509–514, 1968.

[42] JB Pendry, A J Holden, W J Stewart, and I Youngs. Extremely Low Frequency Plasmons. *Physical Review Letters*, 76:4773–6, 1996.

[43] J B Pendry, a J Holden, D J Robbins, and W J Stewart. Low frequency plasmons in thin-wire structures. *Journal of Physics: Condensed Matter*, 10(22):4785–4809, June 1998.

[44] J.B. Pendry, a.J. Holden, D.J. Robbins, and W.J. Stewart. Magnetism from conductors and enhanced nonlinear phenomena. *IEEE Transactions on Microwave Theory and Techniques*, 47(11):2075–2084, 1999.

[45] Dr Smith, Wj Padilla, Dc Vier, Sc Nemat-Nasser, and S Schultz. Composite medium with simultaneously negative permeability and permittivity. *Physical review letters*, 84(18):4184–7, May 2000.

[46] Claus Jeppesen, Sanshui Xiao, Niels Asger Mortensen, and Anders Kristensen. Extended verification of scaling behavior in split-ring resonators. *Optics Communications*, 284(3):799–801, 2011.

[47] T. Koschny, M. Kafesaki, and C. M. Soukoulis. Effective Medium Theory of Left-Handed Materials. *Physical Review Letters*, 93(10):1–4, September 2004.

[48] N Katsarakis, T Koschny, M Kafesaki, E N Economou, and C M Soukoulis. Electric coupling to the magnetic resonance of split ring resonators. *Applied Physics Letters*, 84(15):2943–2945, 2004.

[49] Carsten Rockstuhl, Falk Lederer, Christoph Etrich, Thomas Zentgraf, Jürgen Kuhl, and Harald Giessen. On the reinterpretation of resonances in split-ring-resonators at normal incidence. *Optics express*, 14(19):8827–36, September 2006.

[50] W. Chen and C. Lin. A standing-wave interpretation of plasmon resonance excitation in split-ring resonators. *Optics Express*, 18(13):14280–14292, 2010.

[51] T Zentgraf, J Dorfmüller, C Rockstuhl, C Etrich, R Vogelgesang, K Kern, T Pertsch, F Lederer, and H Giessen. Amplitude- and phase-resolved optical near fields of split-ring-resonator-based metamaterials. *Optics letters*, 33(8):848–50, April 2008.

[52] David Crouse and Pavan Keshavareddy. Role of optical and surface plasmon modes in enhanced transmission and applications. *Optics express*, 13(20):7760–71, October 2005.

[53] Hongcang Guo, Na Liu, Liwei Fu, Heinz Schweizer, Stefan Kaiser, and Harald Giessen. Thickness dependence of the optical properties of split-ring resonator metamaterials. *Physica Status Solidi (B)*, 1261(4):1256 – 1261, 2007.

[54] U. Kreibig and M. Vollmer. *Optical properties of metal clusters*. Springer, 1995.

[55] Giorgio Margaritondo. *Introduction to synchrotron radiation*, volume 148. Oxford University Press, 1988.

[56] Kwang-je Kim. *X-Ray Data Booklet.* Lawrence Berkley National Laboratory, 2009.

[57] Shazia Yasin, D G Hasko, and H Ahmed. Comparison of MIBK / IPA and water / IPA as PMMA developers for electron beam nanolithography. *Microelectronic Engineering*, 62:745–753, 2002.

[58] E. Di Fabrizio, A. Nucara, and R. Gentili, M. Cingolani. Design of a beamline for soft and deep lithography on third generation synchrotron radiation source. *Review of scientific Instruments*, 70(3):1605–1613, 1999.

[59] F. Romanato, E. Di Fabrizio, L. Vaccari, M. Altissimo, D. Cojoc, L. Businaro, and S. Cabrini. LILIT beamline for soft and deep X-ray lithography at Elettra. *Microelectronic Engineering*, 58:101–107, 2001.